BUBBLE TEMPLATE SYNTHESIS OF HOLLOW GOLD NANOPARTICLES

by

CHIVARAT MUANGPHAT

Presented to the Faculty of the Graduate School of

The University of Texas at Arlington in Partial Fulfillment

of the Requirements

for the Degree of

DOCTOR OF PHILOSOPHY

THE UNIVERSITY OF TEXAS AT ARLINGTON

December 2013

ACKNOWLEDGEMENTS

This research project would not have been possible without the support of many people. My deep gratitude goes to my Professor, Dr. Yaowu Hao, who was abundantly helpful and offered invaluable assistance, support and guidance.

I am highly grateful to my committee members. Dr.Efstathios I. Meletis, Dr.Pranesh Aswath, Dr.Choong-Un Kim, Dr.Fuqiang Liu, and Dr.Digant Dave for their guidance and valuable inputs throughout my dissertation work.

I wish to express my sincere thanks to Dr.Jiechao C. Jiang and UTA Characterization Center for Materials and Biology (CCMB) and The Nanotechnology Research & Teaching Facility for providing excellent research facilities with supportive environment.

Special thanks and share the credit of my work to my friends, especially group members, Shih-Hsin Chang, Chien-Wen Huang, Punnapob Punnakitikashem, Orathai Thumthan, Yi-Juin Li, Jiaqi Wu, Megha Panugati, Sina Moeendarbari, Ruiqian Jiang, Mahdi Yarali and Chia Jen Hsu

At the end, my sincere thanks are due to my parents, who have given me the understanding, supporting and endless love, through the duration of my life.

Dec 12, 2013

ABSTRACT

BUBBLE TEMPLATE SYNTHESIS OF HOLLOW GOLD NANOPARTICLES

Chivarat Muangphat, PhD

The University of Texas at Arlington, 2013

Supervising Professor: Yaowu Hao

Recently, a new synthesis method for creating hollow gold nanoparticles by using electrochemically hydrogen nanobubbles as a template was discovered in our research group. Hollow gold nanoparticles with well-controlled, tunable dimension and morphology can be synthesized using various synthesis conditions. Such hollow gold nanoparticles exhibit unique optical properties that can be tuned by changing the nanoparticle structures.

The objective of this study is to understand the formation mechanism of hollow gold nanoparticles synthesized using bubble template synthesis method. The synthesis process can be divided into two main processes: the formation of hydrogen nanobubble and the reduction of gold ions on the hydrogen nanobubble surface. Both processes were observed by in-situ and ex-situ study techniques. Phase Sensitive Interferometry Technique (PSI) is employed for in-situ monitoring the formation of hollow gold nanoparticles. PSI is a very sensitive in-situ technique for detecting sub-nanometer change of thickness on a transparent substrate. Our results demonstrate PSI can be used to probe an electrochemical process without any interference with

the process. Using PSI, the formation of hydrogen nanobubble and the reduction of gold ion on hydrogen nanobubble surface have been in-situ detected by monitoring the modulation shifted due to the optical path length and the amplitude change caused by refractive index change. These results confirmed our hypothesis that the hydrogen nanobubbles act as templates for the formation of hollow gold nanoparticles.

To further test the ability of PSI for in-situ probing an electrodeposition process, PSI has been used to monitoring Underpotential Deposition (UPD) of copper on gold surface. In an UPD process, a single layer of atoms can be electrochemically deposited onto another metal surface. The PSI technique is more suitable than other characterization techniques that have been studied before. Since PSI can probe an UPD process conducted in a normal electrochemical cell and does not interfere with the process. We have successfully detected the formation of one monolayer of copper on gold-coated mica substrate using PSI.

The effect of synthesis parameters on the size, shell thickness and morphology of hollow gold nanoparticles has been ex-situ studied using transmission electron microscopy (TEM) and scanning electron microscopy (SEM). It has been found that, the number of hydrogen nanobubbles increases as the concentration of hydrogen evolution enhancer, overpotential, or deposition time increases. On the other hand, the size of hydrogen nanobubbles significantly decreases with increasing of overpotential or decreasing of pore size of the membrane or hydrogen evolution enhancer concentration. Moreover, the number of gold nanoparticles increases while the size of gold nanoparticles decreases with the increase of applied potential or gold ion concentration, so the number of gold nanoparticles decreases while the size of gold nanoparticles increases as the stabilizer concentration increases. Also, the porosity of gold shell changes while varying either the concentration of gold ion or the concentration of stabilizer.

TABLE OF CONTENTS

LIST OF ILLUSTRATIONS

LIST OF TABLES

CHAPTER 1

INTRODUCTION

Recently, nanostructures with hollow interiors have been extensively studied for many applications because of their unique structures and properties. Hollow gold nanoparticles have been proposed for in-vivo biomedical applications particularly such as photothermal triggers (ScienceDaily, 2008) (Boyd, 2011) for drug release and as a contrast-enhancing agent in optical imaging. Gold nanoparticles are generally considered as biocompatible, as evidenced by the fact that colloidal gold has been safely used to treat rheumatoid arthritis for half a century. Moreover, gold nanoparticles can be functionalized with biomolecules that are specific to receptors over-expressed on diseased cells, in such way gold nanoparticles can conjugate with these cells. Additionally, hollow gold nanostructures is interesting to synthesize and study because they exhibit surface plasmonic properties and catalytic activities different from their solid counterparts.

Most application of gold nanostructures originate from their strong surface plasmon absorption in the visible region of light, which, provide excellent substrates for surface plasmon resonance (SPR) spectroscopy and surface-enhanced Raman scattering (SERS). In solid spherical of gold particles, there is a single resonance at approximately 520 nm, varying slightly depending on size and embedding media. However, for in-vivo biomedical applications, we need particles whose absorption peak lies in the near-infrared (IR) region (800 to1200 nm.). This is an ideal for in-vivo bioapplication because tissue has an absorption minimum in this range. For hollow gold nanoparticles, a shell of gold allows the electromagnetic field to extend further away from the surface and induce greater enhancement than spherical particles, therefore, their SPR peaks can be shifted to cover a spectral region from 400 to 1200 nm. These localized surface plasmons have been employed in a wide range of applications (L. R.

Hirsch R. J., 2003) (Jain PK H. X., 2008) including imaging, (El-Sayed) (Christopher Loo, 2005) chemical and biological sensing and probing, (Amanda J. Haes, 2002) (Robert Elghanian, 1997) (Sonnichsen Carsten, 2005) and targeted photo thermal therapy. (Christopher Loo, 2005) (L. R. Hirsch R. J., 2003) (Xiaohua Huang, 2006) A variety of methods have been reported to prepare hollow gold nanoparticles with different sizes and shell thicknesses. (Huang Y' B', 2007) (Sonnichsen Carsten, 2005)

Originally, gold nanoshells were produced by coating silica beads with gold shells of various thicknesses. This synthesis process is simple but it limits from the limitation of silica bead size that is used as template for creating gold nanoshells. Recently, a new synthesis method for producing hollow gold nanoparticles was discovered in research group. (Chienwen Huang J. J., 2010) (Chienwen Huang Y. H., 2010) (Huang C. , 2010) (LI, 2010) We discovered the electrochemically evolved hydrogen nanobubbles can be served as templates and reducing agents for the formation of hollow gold nanoparticles through the electroless reaction with sodium gold sulfite. Such process is termed as bubble template synthesis method. This new type of synthesis method for making hollow gold nanoparticles will be discussed in details in this research. This synthesis method is much more convenient than other fabrication processes that were invented before and core and particle size of hollow gold nanoparticles can be easily buned by changing the electrodeposition condition. From this reason, this synthesis method has the potential to be applied for creating hollow structure of other materials.

This research in an attempt to obtain a full understanding of the fundamentals of hydrogen bubble nucleation and gold shell formation using bubble template synthesis method. Hollow gold nanoparticles synthesis process involves two integrated electrochemical processes: 1) hydrogen evolution reaction to form hydrogen nanobubbles and 2) electroless deposition process to create a hollow gold nanoparticle on hydrogen nanobubble surface. The formation of hydrogen nanobubble and gold nanoshell has been in-situ studied in this research using Phase Sensitive Interferometry (PSI) to confirm our hypothesis and understand the formation

mechanism of hydrogen nanobubbles and gold nanoparticles. This characterization instrument can real-time observes the nucleation of hydrogen nanobubble and the formation of gold nanoshell by detecting the changing of refractive index and optical path length. This is the first time to in-situ study the formation of nanobubble and nanoparticles using phase sensitive interferometry. Beside in situ phase sensitive interferometry, scanning electron microscopy (SEM), and low- and high-resolution transmission electron microscopy (TEM) will be used to ex-situ investigate the nanobubble formation and nanoparticle morphologies under the different deposition conditions. The effect of electrodeposition conditions (applied potential and deposition time) and the composition of gold electrolyte (concentration of gold complex ions and other additives) were studied. By changing these conditions nanobubble size. Gold shell thickness, shell structure and morphology of hollow gold nanoparticles can be tuned.

In addition, the sensitivity of the phase sensitive interferometry technique was tested using underpotential electrodeposition (UPD) method. A monolayer of copper was deposited on gold surface on a gold-coated mica substrate using UPD. Such monolayer has been detected using PSI. Following our experiment results, It has been demonstrated that the PSI is sensitive to detect the formation of a monolayer of copper on gold film. This technique has the potential to become a new technique for in-situ studying a monolayer of metal on foreign metal in an electrodeposition process without external interference.

This dissertation starts from the discussions about synthesis methods, properties and applications of hollow gold nanoparticles in chapter2. Then, bubble template synthesis process for making hollow gold nanoparticles is described in chapter 3. Phase sensitive interferometry principle and in-situ study of the formation mechanism of hollow gold nanoparticles are given in chapter 4. Chapter 5 is presents ex-situ study results of the effect of synthesis process conditions on the formation of hydrogen nanobubbles and gold nanoshells. The underpotential deposition process and in-situ study using PSI including the experimental set up and results are

presented in chapter 6. The last chapter, chapter 7, is summary and conclusions of this research.

CHAPTER 2

BACKGROUND INFORMATION

In recent years, gold nanostructures have been an intensive research subject from researchers owing to their high electrical and thermal conductivities as well as unique optical properties, which may open new opportunities in catalysis, analysis and other areas; especially in biomedical applications. Gold nanostructures exhibit unique surface plasmon resonance (SPR) properties. SPR is an optical phenomenon arising from the interaction between the conduction electrons in a metal and the electromagnetic field. Gold nanoparticles strongly enhance the scattering and absorption of visible and near infrared light (800-1200 nm.), which leads to several applications such as surface enhanced Raman scattering (SERS) (Prashant K. Jain, 2009), bio-imaging contrast enhancement, and photothermal therapy. It is not only their fascinating optical properties, but also gold nanoparticles have other advantages for biomedical applications, such as their compact size, biocompatibility, and chemical stability. The ideal size of gold nanoparticles that are suitable for biomedical applications is between 20 and 100 nm depending on the application.

Recently, a new synthesis method, termed as bubble template synthesis, for producing hollow gold nanoparticles was discovered in our research group. In this chapter, fabrication process for making hollow gold nanoparticles, the advantage and also disadvantage of fabrication processes are described in this chapter. Also, their optical properties and potential of *in vivo* biomedical applications are included.

2.1 Hollow Gold Nanoparticles Fabrication Methods

Hollow nanoparticle is a type of spherical nanoparticle consisting of a empty core, which is covered by a thin metallic shell. For the last decade, there are several synthesis methods that have been reported for making hollow nanoparticles. In this chapter, we categorized these

methods into three main classes: (1) template-mediated approaches, (2) galvanic replacement (Sara E. Skrabalak, 2008), and (3) chemical etching (Kwangjin An S' G'-I', 2008). Each approach has its own advantages and disadvantages that will be discussed in this chapter.

2.1.1 Nanotemplate-Mediated Approach

Template-mediated synthesis approach is the most popular fabrication method. (Frank Caruso R' A', 1998) Hollow gold nanoparticles were generally prepared by coating the surfaces of colloidal particles (Astruc, 2004), (Kwangjin An T. H., 2009) (e.g., silver colloids, silica beads, and polymers latexes) with thin layers of gold, followed by selective removal of the colloidal templates by a post-treatment through calcination or wet chemical etching.

There are two types of template materials that are used for making hollow nanoparticles; hard and soft templates. For hard template, silica particles and polymer beads (Tenhu, 2007) are most widely used for the synthesis of hollow nanoparticles. There are various methods to coat materials on these hard templates including layer-by-layer assembly (Rachel A. Caruso, 2001), (Frank Caruso M' S', 2001), chemical deposition (Imhof, 2001), (Christina Graf, 2003), adsorption (Sang-Wook Kim, 2002) (Xiaoming Sun, 2004) (Mu Yang, 2005), casting (S.B. Yoon, 2002), and atomic layer deposition (J.Hwang, 2004). Various soft templates have been also employed for the synthesis of hollow nanostructures, including microemulsions formed in a two-phase solution (Feldmann, 2007) (Yongsheng, 2003), gas bubbles in liquid (Qing Peng, 2003) (C.Z. Wu, 2006; Haolan Xu, 2007), and micelles (or vesicles) assembled by surfactants and supramolecules (Seong Su Kim, 1998).

Lee et al. Nanocrescent structures have been produced by depositing silver over latex beads on a surface, then dissolving away the bead. These hollow spheres are open-ended with a sharp edge, which greatly enhances the EM field. This engineered hot-spot approach yields improved SERS enhancements over core/shell systems. However, both nanocrescents and core/shell systems are relatively too large for applications that are required an smaller particle size.

Halas and co-workers first produced the hollow gold nanoparticles with directly depositing gold onto silica colloidal sphere surface. They deposited small gold nanoparticles (with a diameter of 1-2 nm) on the surface of silica sphere that were first synthesized using the Stober method, the basic reduction of tetraethylorthosilicate (TESO) ($SiC_8H_{20}O_4$) in ammonium hydroxide (NH_4OH).

$$SiC_8H_{20}O_4+NH_4OH \rightarrow \text{silica} \quad (2.1)$$

The gold shell is grown on the silica cores via the seed-mediated electroless plating. Small gold nanospheres (2-4 nm in diameter) can first be attached to the silica core that is modified by using an amine-terminated silane (either aminopropyltriethoxysiland (APTES) ($C_9H_{23}NOSi$) or aminopropyltrimethoxysilane (APTMS) ($C_6H_{17}NO_3Si$)). The gold shell was electrolessly plated onto the colloidal gold nucleation sites from diluted solution of gold chloroauric ($HAuCl_4$) and potassium carbonate (K_2CO_3) using formaldehyde (CH_2O) as a reduction agent, allowing additional gold to be reduced until the seed particles coalesced into a complete shell (Oldenburg et al 1999a). To obtain hollow gold nanoparticles, after gold coating on the surface of the template particles, the template needs to be removed by a post-treatment. The diameter of the gold nanoshell is largely determined by the diameter of the silica core, and the shell thickness can be controlled through the amount of silica core and the gold salt solution. Usually, the hollow structures obtained via a template-mediated approach using silica and polymer beads as the templates are often larger than 200 nm because it is hard to make smaller sized template particles. (Kwangjin An T. H., 2009) A continuous gold shell generally has a thickness between 5 and 30 nm as shown in Figure 2.1

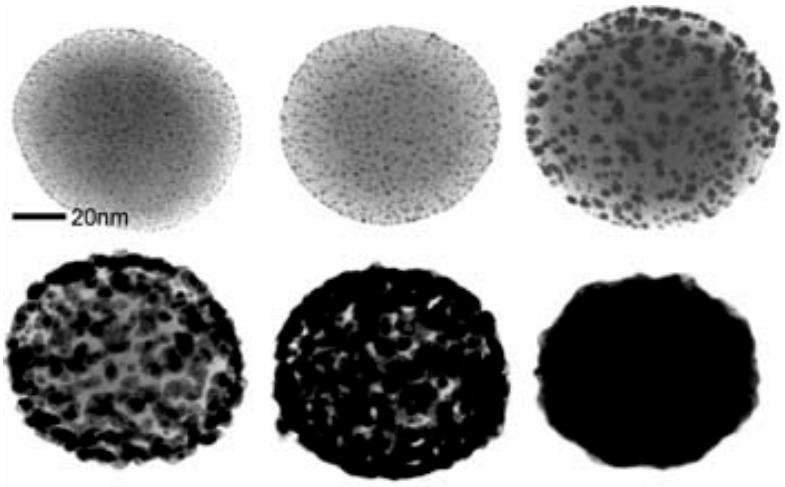

Figure 2.1 Series of TEM images showing gold colloid growth into a complete shell on silica core particle surface. Beginning form the upper Left, the gold colloid (dark dots) serve as nucleation sites for additional electroless plating of gold. As additional gold is deposited onto the gold islands, the gold grows until coalescing with neighboring colloid, finally forming a complete metal shell (bottom right).

Polystyrene spheres have been also used for the formation of hollow gold nanoparticles. The advantage for using the polystyrene spheres as the core is that they are readily available commercially in a wide range of sizes, and with dyes or other molecules doped into them. Similarly, the small gold colloids are also grown on the polystyrene cores via the seed-mediated electroless plating from gold chloroauric acid ($HAuCl_4$) with reduction agent. For soft template, microemulsions in a two-phase solution, gas bubbles in liquid, and micelles assembles by surfactants are mostly employed. (Han-Pu Liang, 2004)

Although these methods have enabled to prepare gold nanoshells supported on dielectric cores, their yields were relatively low. The gold nanoshells prepared using these methods were also characterized by problems such as rough surfaces, polycrystallinity, non-uniformity in shell thickness poorly defined composition and difficulty in removing the colloidal templates without breaking the shells. The limitation of template size and the complication of fabrication process is the main disadvantage of the template-mediated method, and also the post-treatment necessary to remove the templates adds complexity to the whole synthetic process and increases the chance of the structural deformation as well as the introduction of

impurities. As a result, it needs to develop a capable method of generating hollow nanostructures of metals with well-defined void sizes and homogeneous smooth, highly crystalline walls.

2.1.2 Galvanic Replacement Method

For the synthesis of hollow metal nanostructures, the galvanic replacement reaction provides a remarkably simple and versatile route for making metal nanostructures with controllable hollow interiors and porous walls. The shell thickness, porosity and composition of the hollow structure can be tailored by controlling the size and morphology of the template and the degree of replacement of gold atoms in the template. (Xiamao Lu, 2007).

The Xia group is the first group that has developed gold hollow structures were synthesized via galvanic replacement in which silver nanoparticles served as sacrificial template (W.Y.). This synthetic technique utilizes the redox potential between metallic silver and gold salt in solution. This reaction takes place when the metal nanoparticles are in contact with other metal ions of higher reduction potential (Jonathan A. Edgar). For creating hollow gold nanoparticles, the galvanic plating happened when the Au^{3+} ions come in contact with the silver atom. The Au^{3+} ions were reduced to gold atoms and oxidize the silver to Ag^{1+}ions. For every three silver atoms oxidized, a single gold atom is reduced. It is leading to structures with 1/3 the metal and leaving a hollow core. Sun and co-worker demonstrated this simple and generic approach to the large-scale synthesis of hollow gold nanostructures.

The key step of this approach is the galvanic replacement reaction between silver template and a salt precursor solution refluxed at an elevated temperature. The major steps involved in this process are shown in Figure 2.2 (a), with the gold/silver combination as an example. $HAuCl_4$ is added to the suspension of silver nanoparticles. When silver nanoparticles co-exist with $AuCl^{4-}$ ions in the solution, these ions take electrons from silver atoms and replace them relieving silver cations because the standard reduction potential of the $AuCl_4^-$/Au redox pair 0.99V vs the standard hydrogen electrode (SHE),

$$Ag^{+}(aq) + e^{-} \rightarrow Ag(s) = +0.8V \quad (2.2)$$

$$[AuCl_4]^{-}(aq) + 3e^{-} \rightarrow Au(s) + 4Cl^{-}(aq) = +0.99V \quad (2.3)$$

$$3Ag(s) + AuCl_4^{-}(aq) \rightarrow Au(s) + 3Ag^{+}(aq) + 4Cl^{-}(aq) = +0.19V \quad (2.4)$$

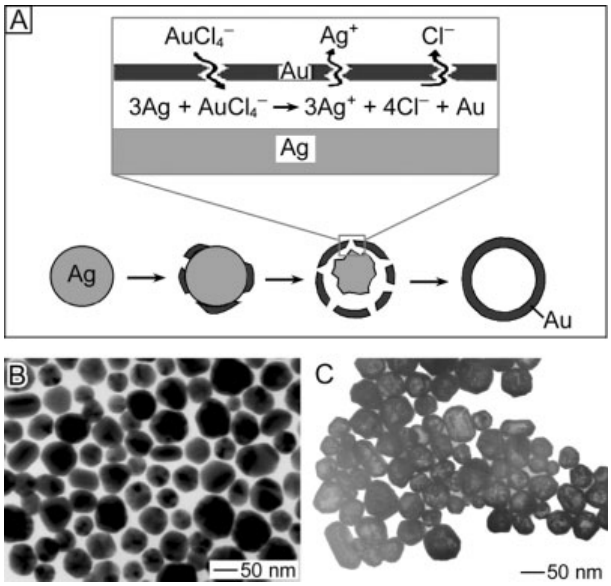

Figure 2.2 (a) Schematic illustration of the experimental procedure that generates gold nanoshells by templating against silver nanoparticles. (b) TEM Image of silver nanoparticles prepared using the polyol process. (c) TEM image of gold nanoshells obtained by reacting these silver nanoparticles with an aqueous $HAuCl_4$ solution.

When the gold atoms have reached a critical concentration, they will nucleate and grow into small cluster, and then gold cluster will form a shell-like structure around the silver template. As the reaction proceeds, small holes were formed on the surface of the nanoparticles in the early stage of the galvanic replacement reaction. This small hole serves as an anode where silver atoms are oxidized. The released electrons from silver atoms migrate to the surface of the nanoparticles and reduce $AuCl4^{-}$ ions to Au atoms, which adsorb and grow into an Au shell on the surface of nanoparticles until the silver template has been completely consumed. If the reaction occurred at an elevated temperature, the gold shell will reconstruct into a highly crystalline structure via processes such as Ostwald ripening. At the same time, the openings in the wall will also be closed to form a seamless gold shell, characterized by a smooth surface. According to the stoichiometric relationship shown in Equation 2.2, only one gold atom is

generated when every three silver atoms are oxidized. As a result, the thickness of the gold nanoshell is only one ninth of the lateral dimension of the corresponding silver template.

Figure 2.2 (b) shows the transmission electron microscopy (TEM) image of a sample of silver nanoparticles that were prepared using the so called polyol process. These nanoparticles exhibited a range of different morphologies, with an everage size of ~50nm. Note that the central portions of these nanoparticles were darker than their edges. Figure 2.2 (c) shows a TEM image of these silver nanoparticles after they have completely reacted with $HauCl_4$. In this case, the center portion of each particle was lighter than its edge, indicating the formation of a nanostructure with hollow interior. (Yugang Sun, Metal Nanostructures with Hollow Interiors, 2003)

Another similar galvanic replacement synthesis process for making hollow gold nanospheres has been developed by Liang et al., in which cobalt is used as the sacrificial template to create hollow gold nanoparticles. They found significantly increased homogeneity over solid silver nanoparticle systems for the application of single-particle pH sensing using surface functionalization with a pH sensitive probe molecule. To achieve broad size tunability of this hollow gold nanoparticle system, size control of the cobalt sacrificial template is required. Although there have been significant advances in the production of small sized (~5-10 nm) cobalt nanoparticles with incredible homogeneity, there have been little work in the production of larger particles. The main instance of this work is done by Kobayashi et al. who showed that the key to control particle size is in the concentration of nucleation sites. In general, at a given metal salt concentration, the more nuclei that are formed, the smaller the average particle size will be. These hollow gold nanoparticles were made by reduced gold ions to metal gold on cobalt nanoparticles. Simultaneously, the elemental cobalt is oxidized and leaves the complex. The amount of gold added during synthesis can change, the aspect ration of hollow gold nanoparticles. These hollow gold nanoparticles also have a unique set of attributes, including strong, narrow and tunable absorption peak. (ScienceDaily, 2008) (Boyd, 2011). Because of the

stability of the cobalt salt, the reduction cannot be done by citrate alone and a stronger reducing agent is required. Sodium borohydride is used in this case, to reduce the salt and citrate is present only as a capping agent. The inner diameter, or wall thickness, can be controlled by the amount of gold salt used leading to complete control of the optical properties of particles ranging from 20 to 70 nm. The peak of the surface plasmon band absorption can be tuned between 550 and 820 nm. For a particular diameter and wall thickness, the absorption band is relatively narrow because of the near-monodisperse distribution, as determined by single-nanosphere scattering spectrum. These hollow gold nanoparticles have been further demonstrated to be active SERS substrates with excellent consistency based on a single hollow gold nanoparticles SERS spectra.

2.1.3 Chemical etching

Etching, or partial dissolution of the interior of nanoparticles, is another approach to synthesize hollow or porous nanomaterials. Zhang and et al., reported the fabrication process of such a multilayered structure. They started to make gold nanoshells with the synthesis of super paramagnetic iron oxide (Fe_3O_4) colloidal nanocrystal clusters using a high-temperature hydrolysis reaction. Iron oxide nanoparticle is composed of small primary nanocrystals that is called the nanocrystal clusters, with uniform sizes tunable from 30 to 180 nm. Due to their relative large sizes, the iron oxide cores interact strongly with external magnetic fields and can be easily separated from solution in a low magnetic field gradient ($<30 Tm^{-1}$). In order to attach gold seeds to the surface, a thin layer of silica through a sol-gel process is coated on iron oxide particles. Iron oxide clusters are modified with a monolayer of coupling agent of 3-aminopropyl-triethoxysilane (APTS) by heating the mixture in isopropanol at 80^0C. Citrate-stabilized gold seeds (~15 nm in diameter) can therefore be loaded onto the surface of the silica through the strong chemical affinity between gold and primary amines, as shown in the TEM image at the bottom of Figure 2.3 (left side). In the presence of poly(vinyl pyrrolidone) (PVP), the composite colloids were overcoated with another layer of silica to fully encapsulate the gold seeds inside

the silica matrix (Figure 2.3, bottom right). A simple surface-protected etching process using sodium hydroxide (NaOH) solution made the outer silica layer porous, exposing the gold seed to outside chemical species and providing them the space that is needed for growing into complete shells. Finally, the gold nanoshells with tunable optical properties were formed via overgrowth of the embedded gold seeds. Although several steps are involved, the overall synthesis is straightforward and highly reproducible because the sol-gel process, surface-protected etching, and seed-mediated growth can all be carried out sequentially with simple setups under mild conditions.

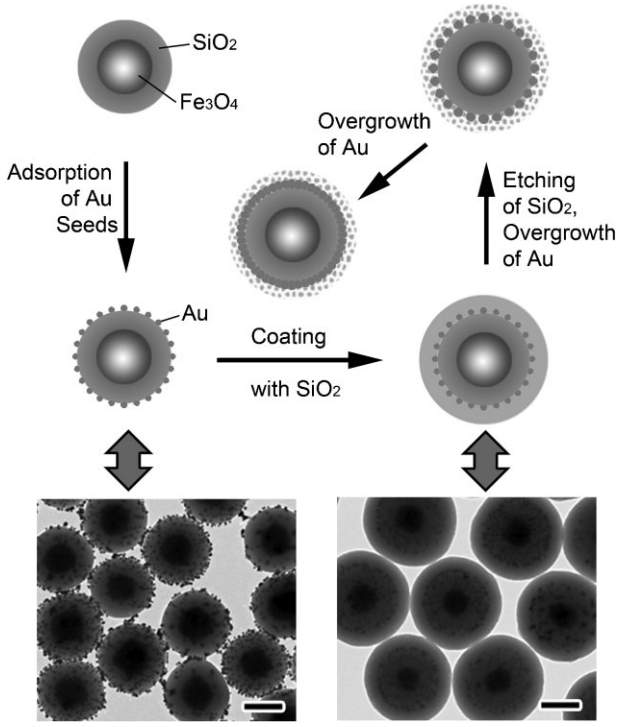

Figure 2.3 Schematic illustrations of the procedures for the fabrication of gold nanoshells containing superparamagnetic iron oxide cores. A unique porous silica layer is produced by a surface-protected etching process, and then utilized to control the seeded growth of Au nanoshells with enhanced reproducibility and structural and optical stability. The TEM images show the iron oxide/silica cores loaded with gold seeds (left) and then further overcoated with an additional layer of silica (right). Scale bars are 200 nm. (Qiao Zhang, 2010)

2.2 Optical Properties

Surface plasmon resonance (SPR) property originates from the collective oscillation of their conduction electrons in response to optical excitation. Gold nanostructures such as nanoparticles, nanowires, nanospheres and nanoshells exhibit different SPR features. With the fact that gold nanoparticles are also easily conjugated to antibodies and other biomolecules, one can envision a myriad of potential applications that are under development, including immunoassays, modulated drug delivery, photothermal cancer therapy, and imaging contrast agents.

As such the SPR frequency is strongly dependent on the size, shape, and surface functionality of the metallic nanostructures. Figure 2.4 (a) compares the UV-VIS extinction spectra of aqueous dispersions of gold solid particles (with a core diameter of ~50 nm) and nanoshells made of gold (with a core diameter of ~50 nm and wall thickness of ~4.5 nm. The solid colloids exhibited an intense, sharp peak at ~530 nm, while the SPR peak for nanoshells was broader and red-shifted to ~680 nm. Based on the Mie scattering theory, the SPR band of a metal nanoparticle is expected to red-shift with increasing refractive index of the dispersion medium. Figure 2.4 (b) plots the experimental dependence of peak shift ($\Delta\lambda_{max}$) relative to the peak recorded with water as the surrounding medium) on the refractive index unit (RIU) for the gold solid colloids and gold nanoshells, respectively.

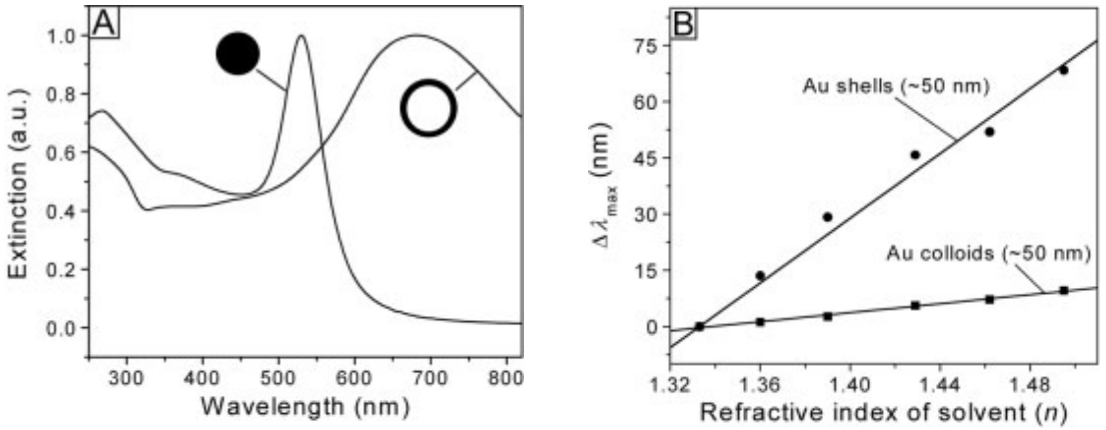

Fig. 2.4 (a) A Comparison between the UV-VIS extinction spectra of gold solid colloids (~50nm in diameter) and gold nanoshells with core diameter of ~ 50 nm and wall thickness of ~ 4.5 nm. (b) Plot of the dependence of peak shift (hk_{max}, relative to the peak position obtained with water as the dispersion solvent) on the refractive index (n) of surrounding medium. The sensitivity factors, hk_{max}/hn, were ~ 60 and ~ 410 nm/RIU for ~ 50 nm gold solid colloids and ~ 50 nm gold nanoshells, respectively.

This result implies that the nanoshells are about seven times more sensitive to environmental change when compared with solid colloids having roughly the same diameter. Because the SPR intensity decays exponentially over a length scale of ~50 nm. The modulation of SPR for surface-modified gold nanostructures is predominated by the dielectric constant of the absorbed, layer instead of the bulk solvent. Therefore, the higher sensitivity of gold nanoshells to environmental changes, as well as the high extinction coeffecient in the red regime, should make gold nanoshells an ideal platform to probe biologically binding events which occur on the gold surface. (Yugang Sun, Metal Nanostrucutres with Hollow Interiors, 2003)

For hollow gold nanospheres, the SPR frequency is a sensitive functional of the inner and outer diameter of gold nanoparticles. Therefore, the SPR property can be tuned by two geometrical parameters: shell thickness and cavity size. Most methods are based on the outward growth of the nanosphere shell. As shown in Figure 2.5, Hirsch and co-worker demonstrated the tunability of optical properties for nanoshell with the same silica core radius but the different shell thickness. They observed the plasmon resonance of the particles with

decreasing thickness of the gold shell. They found that either absorbs or scatters light is shifted to NIR light region of the electromagnetic spectrum with decreasing the shell thickness. Wheeler has also discovered that an aspect ratio of 10:1 (sphere diameter of 50 nm to shell thickness of 5 nm) yields absorbance spectra in the visible and near infrared range, a comfortable range for most biological processes since human tissue is relatively transparent to near infrared radiation. (Boyd, QB3 Fellowship Furthers Research on Hollow Gold Nanospheres for Cancer Treatment, 2011)

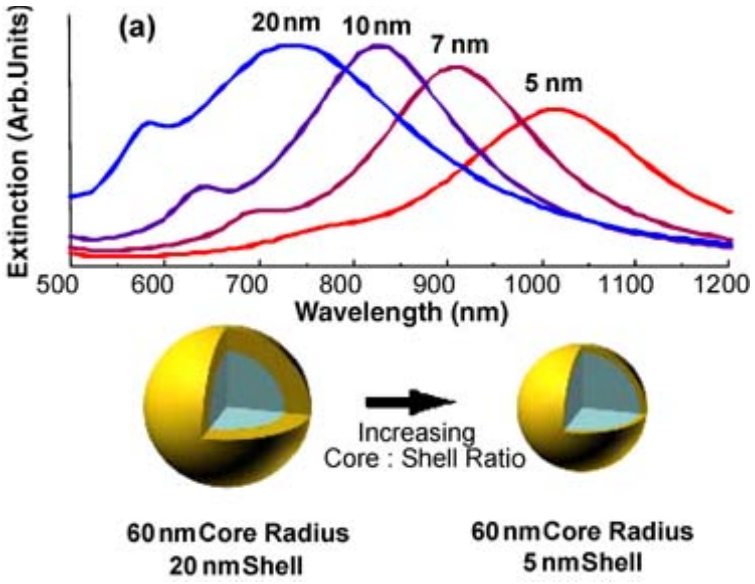

Figure 2.5 Optical tunability is demonstrated for nanoshells with a 60 nm silica core radius and gold shells 5, 7, 10, and 20 nm thick. Observes that the plasmon resonance (extinction) of the particles red shifts with decreasing thickness of the gold shell (or an increasing core-shell ratio). Nanoshells are easily fabricated with resonance in the NIR. also altering the core size, Changing the composition of the core and shell, and forming multilayered structures can achieve greater tunability.

Depending on the size and thickness of the nanoshell, particles can be designed to either absorb or scatter light over much of the visible and infrared regions of the electromagnetic spectrum, including the near infrared region where penetration of light through tissue is maximal.

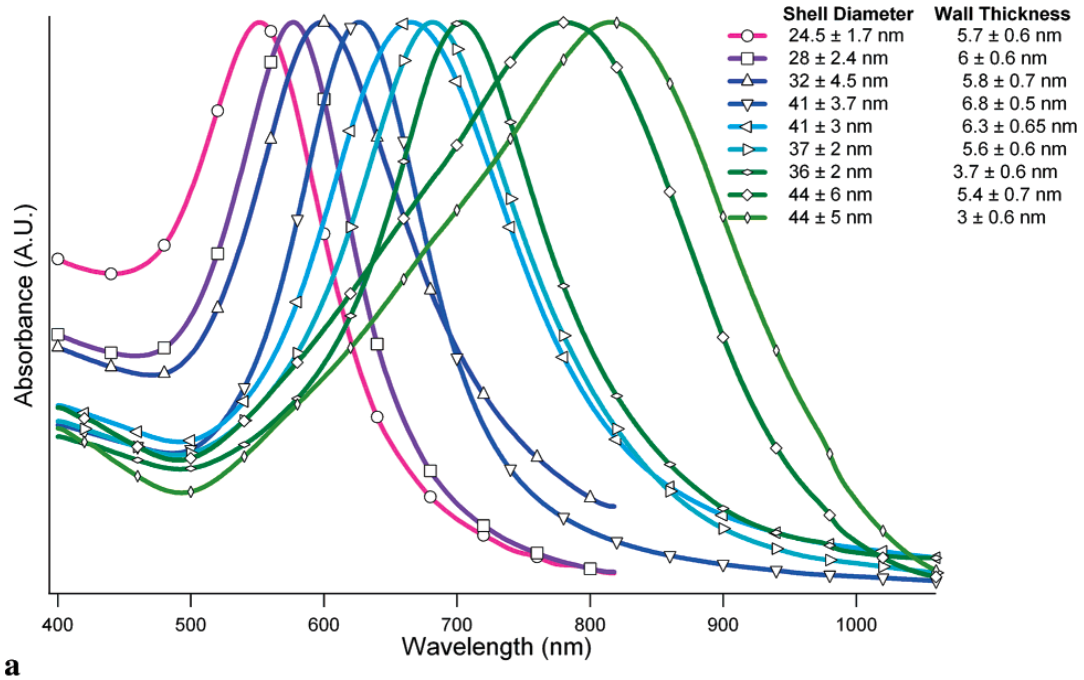

Figure 2.6 (a) UV-VIS absorption spectra of nine hollow gold nanoparticle samples with varying diameters and wall thicknesses. (b) Image showing the color range of hollow gold nanoparticle solutions. The vial on the far left contains solid gold nanoparticles, the rest are hollow gold nanoparticles with varying diameters and wall thicknesses.

Schwartzberg et al., have found that by varying wall thickness and particle size is possible to tune the plasmon absorption across much of the visible spectrum as in Figure 2.6

(a), UV-VIS data, and 2.6 (b). These spectra are representative of many experiments and show the full range of tunability of this system. By increasing particle size at a constant wall thickness, the absorption band will red-shift as the plasmon oscillation decreases in energy. However, increasing wall thickness at constant particle size will blue-shift the absorption band. The band shifts to higher energy because as the inner diameter of the hollow gold nanoparticles decreases it takes on more solid-particle-like properties. Because solid gold particles at these sizes have plasmon bands at approximately 520 nm, the absorption will always shift in this direction as wall thickness increases. Figure 2.7 (a) and (b) show the effect of the aspect ratio of particle size and wall thickness on plasmon absorption as well as the effect of particle size and wall thickness on plasmon absorption. (Adam M. Schwartzberg, 2006)

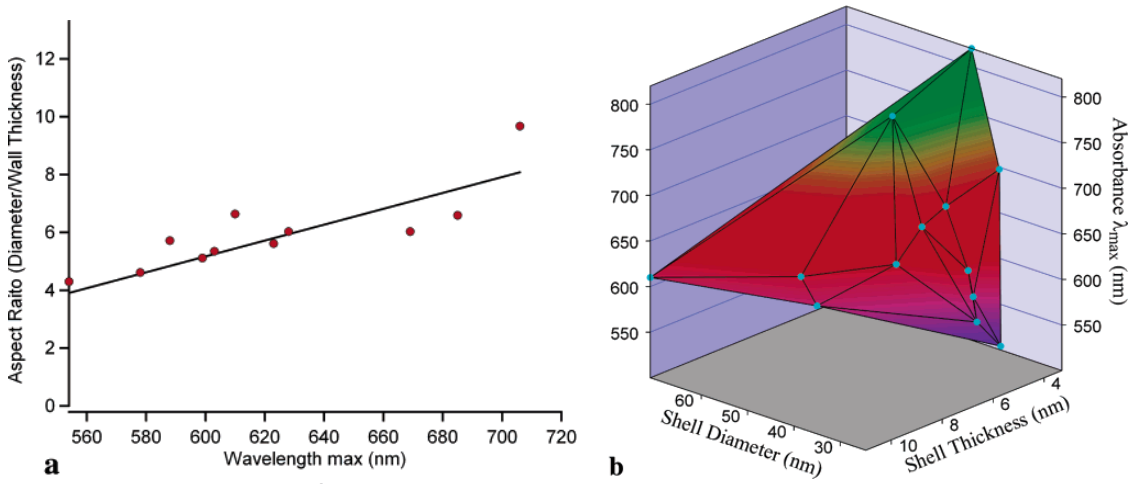

Figure 2.7 (a) Plasmon absorbance maximum wavelength (λ_{max}) as a function of the aspect ration of shell thickness and shell diameter. The line is a best fit approximation to guide the eye. (b) 3D plot of plasmon absorbance maximum wavelength (λ_{max}) as a function of the shell thickness and shell diameter. Each point on both plots represents an individual set of experiments and the average measured lengths.

All of these properties are important for the applications of cancer treatment, as mentioned before. The hollow particles can be made in sizes ranging from 20 to 70 nanometers in diameter, which is considered ideal for biological applications that require particles to be

incorporated into living cells. The heat that kills the cancer cells depends on light absorption by the metal nanoparticles, so more efficient absorption of the light the better. (Kosich, 2008)

2.3 Applications of Hollow Gold Nanoparticles

2.3.1. In Vivo Biomedical Applications of Gold Nanoparticles

Gold nanoparticles have been extensively explored for in vivo biomedical application particularly for cancer imaging and therapy. Generally, gold nanoparticles are regarded as biocompatible, and no acute cytotoxicity has been observed so far. The colloidal gold has been safely used to treat rheumatoid arthritis for half a century. Moreover, gold nanoparticles can be easily functionalized with targeting biomolecules through well-established thiol-gold conjugation chemistry.

The applications of gold nanoparticles to cancer nanotechnology originate from their SPR effects. SPR resulted in the enhancement of scattering and absorption of the local electromagnetic field at the metal surface which has made gold nanoparticle as attractive candidates for cancer imaging and photothermal therapy agents. For in vivo biomedical applications, it required deeper penetration of NIR light. The reason is because the primary absorbers in tissue are water, and blood (hemoglobin and oxyhemoglobin) and both are slightly" transparent" in the NIR range as shown in Figure 2.15. Therefore, by designing gold nanoparticles with SPR peaks in this NIR region, the NIR light is preferentially scattered and absorbed by gold nanoparticles and doesn't attenuate by the tissue.

2.3.1.1 Gold Nanoparticles as Diagnostic Agents

The development of new and early cancer diagnostic techniques is contributing to an increase in cancer survival rates. Researchers are trying to improve the resolution of the conventional imaging techniques and developing new imaging modalities. The performance of these platforms could be increased through integration with appropriate contrast enhancement agents such as gold nanoparticles. Optical coherence tomography (OCT) and surface enhance

Raman scattering (SERS) using gold nanoparticles as agents are promising diagnostic techniques for in vivo imaging.

2.3.1.1.1 Optical Coherence Tomography (OCT)

To date, most imaging studies using gold nanoparticles were carried out in cell culture. The versatile optical properties of gold nanoparticles have enables optical imaging of cells and phantoms with a wide variety of contrast mechanism. Gold nanoshell-enhanced optical coherence tomography (OCT) has the potential for molecular imaging and improved detection of diseases. The OCT is based on a Michelson interferometer, which measures the interference signal between the backscattered light of a sample and a reference. Thus image contrast increased primarily from the intrinsic scattering and absorption of light by tissue. As a result, it is hard to resolve the minor morphological changes involved in the early stage development of a disease. But this effect can be enhanced by gold nanoparticles with their large absorption and scattering cross-section.

Xia and co-workers have demonstrated that using gold nanocages as contrast agents for the OCT technique. The OCT was performed on phantom samples with gold nanocages. As a laser with a central wavelength 825 nm was scanned over the tissue phantom, the intensity of backscattered light was measures as a function of depth. Because of the intense absorption of the gold nanocages, a strong modulation of the backscattered spectrum can be observed at blue side of the OCT source spectrum.

Agrawal et al. study of OCT at 1310 nm in water and turbid tissue-simulating phantoms with added nanoshells were carried out to determine the sensitivity threshold for several nanoshell geometries (Agrawal A, 2006). For the best nanoshell tested, which has a core of 291 nm in diameter and a shell thickness of 25 nm, a concentration of 10^9 nanoshells/mL was needed to produce a signal increase. Although such concentration can be achieved theoretically under optimized conditions (assuming that 1% of each cell's surface can be covered by

nanoshells), in vivo targeted imaging would be extremely challenging since nanoshells of such size may never extravagate.

2.3.1.1.2 Surface-Enhanced Raman Scattering (SERS)

Raman spectroscopy is the measurement of the wavelength and the intensity of the inelastically scattered light and has been widely used as an analytical tool for the chemical research. The Raman effect is an inelastic scattering by the vibrational states of molecules. Typically, Raman signals are quite weak and therefore a sufficient analyze concentration is needed in order to provide enough signal. Raman scattering is dramatically enhanced if the molecules are close to the gold nanoparticle surface as illustrate in Figure 2.8. This effect is called surface-enhanced Raman scattering (SERS). Based on this enhancement on gold nanoparticles, SERS is an alternative candidate to fluorescence for biomolecular sensing. Compared to fluorescence for biomolecular sensing, gold nanoparticles are more stable and they do not suffer from photobleaching which is the major limitation for fluorescence based methods.

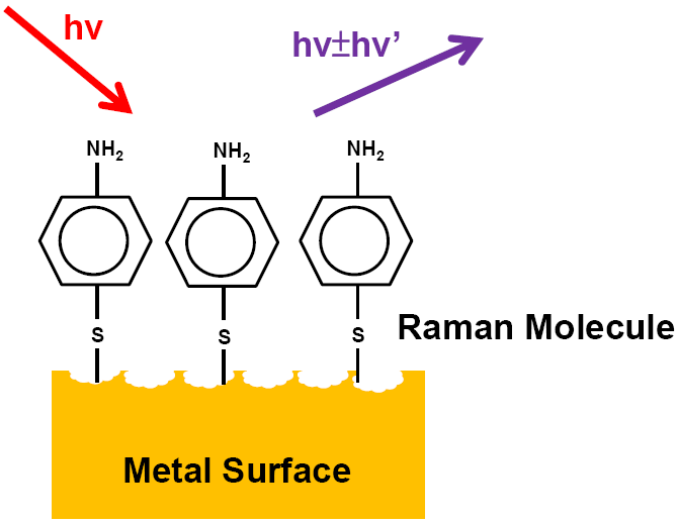

Figure 2.8 Illustration of surface enhanced Raman scattering (SERS). The red light represents the incident light and the purple line is the raman shifted emitted light.

2.3.1.2 Gold Nanoparticles as Photothermal Agents

Conventional strategies for cancer intervention include surgery, chemotherapy, and radiation therapy. Taking advantage of their unique properties, most studies of gold nanoparticle-based cancer therapy have used photothermal therapy for the destruction of cancer cells or tumor tissue, which may be potentially useful in the clinical setting. Cancer cells are more sensitive on heat damage than health tissue, heat induced cell death is used as a noninvasive cancer treatment method. Several kinds of gold nanoparticles have been demonstrated that they can be used as photothermal therapy agents such as spherical gold nanoparticles, gold nanorods and gold nanoshells. All of them have shown their capability to generate localized heat to induce cancer cell death only in the nearby area of the nanoparticles while limiting the damage to the surrounding health tissues. It was estimated that 70-80 °C can be achieved through light absorption by the gold nanoparticles. (Huang X, 2006b) In a recent report, it was suggested that 5000 gold nanoshells per prostate cancer cell was needed to achieve cell kill (stern JM, 2007). PEG-coated nanoshells with peak absorption in the NIR region were intravenously injected into tumor-bearing nude mice (Stern JM, 2008; O'Neal DP, 2004). In one study, all tumors treated with the NIR laser were ablated and the mice appeared tumor free for several months while tumors in control animals (NIR laser treatment without nanoshell injection) continued to grow. In another study, 93% of tumor necrosis and regression was observed in a high dose nanoshell (8.5 ìL/g) treated group (Stern JM, 2008). Surprisingly, a slightly lower nanoshell dose (7.0 ìL/g) only resulted in tumor growth arrest at 21 days but not tumor ablation. The reason why such a subtle difference in nanoshell dose could cause dramatically different therapeutic efficacy deserves careful investigation. It is worth noting that all these in vivo cancer therapy studies only involve passive tumor targeting but not specific molecular targeting. Passive tumor targeting is due to the non-specific accumulation of the nanoshells in the tumor, termed “the enhanced permeability and retention (EPR) effect”, since

the tumor vasculature is usually more leaky than normal blood vessels and there is no lymphatic drainage in the tumor (Maeda et al 2000).

2.3.1.3 drug delivery

Nanoshells have been tested for drug delivery. In one early study, composites of hydrogels and gold nanoshells were developed for photothermally-modulated drug delivery (Sershen SR, 2000). Irradiation at 1064 nm was absorbed by the nanoshells and converted to heat, which led to the collapse of the hydrogel thus significantly enhancing the drug release. Subsequently, modulated drug delivery of methylene blue, insulin, and lysozyme was achieved by irradiation of the drug-loaded nanoshell-hydrogel composites, with the drug release rate dependent upon the molecular weight of the therapeutic molecule (Bikram M, 2007). Hollow gold nanoshells can also encapsulate enzymes such as horseradish peroxidase (HRP). Drug delivery using gold nanoparticles, in combination with their intrinsic capability for photothermal therapy, should be explored in the future. Currently, which type of gold nanoparticle is the most suitable for drug delivery applications is still debatable. It was found that the intracellular uptake of different sized and shaped gold nanoparticles is highly dependent upon their physical dimensions (Chithrani BD, 2006). The absorption/scattering efficiency and optical resonance wavelengths have been calculated for three commonly used classes of gold nanoparticles: nanospheres, nanoshells, and nanorods (Jain PK L' K'-S', 2006a). The narrow range in the SPR peaks of nanospheres (~520–550 nm) resulted in very limited use for in vivo applications. The SPR peaks of gold nanoshells lie favorably in the NIR region. The total extinction of nanoshells has a linear dependence on the overall size, however independent of the core/shell radius ratio. The relative scattering contribution to the extinction can be rapidly increased by increasing the nanoshell size or decreasing the ratio of the core/shell radius. Gold nanorods were found to have comparable optical properties at much smaller effective size, with absorption and scattering coefficients an order of magnitude higher than those for nanoshells and nanospheres. While nanorod with a higher aspect ratio and a smaller effective radius is a better

photoabsorbing nanoparticle suitable for therapeutic applications, that with a larger effective radius is more favorable for imaging purposes.

In order to make gold nanoparticles more useful for drug delivery and other biomedical applications (imaging and therapy), they need to be effectively, specifically, and reliably directed to a specific organ or disease site without alteration. Specific targeting in vivo has not been achieved for gold nanoparticle-based drug delivery, due to the relatively large overall size of the conjugate (typically more than 50 nm in diameter), which prohibits efficient extravasation. Although utilization of passive targeting only has been shown to be efficacious in certain xenograft subcutaneous tumor models, they may not truly reflect the clinical situation. Transgenic and orthotropic tumor models are more clinically relevant and these tumors typically have much less leaky vasculature than subcutaneous ones, which will make passive targeting unsuitable for either cancer imaging or therapy. Molecular cancer markers over-expressed on the tumor vasculature may be the targets of choice. (Weibo Cai, 2008)

2.3.2 In vitro Biomedical Applications of Gold Nanoparticles

Oligonucleotide-capped gold nanoparticles have been reported for polynucleotide or protein detection using various detection/characterization methods such as atomic force microscopy (AFM) (Han et al 2000; Jin et al 2007), gel electrophoresis (Qin and Yung 2007), scanometric assay (Son and Lee 2007), chronocoulometry (Zhang et al 2007), amplified voltammetric detection (Wang et al 2008a), SPR imaging (Li et al 2006), and Raman spectroscopy (Cao et al 2002). In some reports, picomolar even femtomolar concentrations of DNA targets have been detected. Bifunctional DNA-based adsorbate molecules have been evaluated as molecular rulers, based on the SERS signals that vary independently in intensity as a function of the distance from the gold nanoshell surface (Lal et al 2006).

Gold nanoparticles have also been employed for many other applications such as immunoassay (Hirsch et al 2003a, 2005; Liu et al 2008), protein assay (Tang et al 2007), time-of-flight secondary ion mass spectrometry (Kim et al 2006), capillary electrophoresis (Tseng et

al 2005), and detection of cancer cells (Kah et al 2007; Medley et al 2008). In one report, dynamic light scattering (DLS) enabled quantitative estimation of the concentration of intravenously injected gold nanoshells in mouse blood (Xie et al 2007). This technique (Cai et al) may also be applicable towards estimating the circulation life time of other solid nanoparticles. Gold nanoshells functionalized with a pH-sensitive SERS reporter molecule, 4-mercaptopyridine, were shown to be responsive to the pH of the surrounding media within the range of 3 to 7 (Jensen et al 2007). Another study has evaluated the use of gold nanoshells as optical biosensors for real-time detection of streptavidin-biotin interactions in diluted human blood (Wang et al 2008b). However, both the sensitivity (~3 μg/mL) and the dynamic range (3–50 μg/mL) were very poor.

CHAPTER 3

BUBBLE TEMPLATE SYNTHESIS OF HOLLOW GOLD NANOPARTICLES

Recently, our research group discovered a new synthesized method for making hollow gold nanoparticles. This is the first time that nanoscale gas bubbles are proposed to be used as templates for synthesis hollow nanostructure. This new synthesis method uses electrochemically evolved hydrogen nanobubble as templates and reducing agent for the deposition of gold shell. The formation of this shell structure occurs through the electroless reaction. By this method, we can create a large amount of hollow gold nanoparticle with well-controlled size, hollow dimension, and shell structures. The particle size, core size and shell structure of hollow gold nanoparticles can be tuned by varying gold electrolyte composition and electrodeposition conditions. This synthesis method is less complicated than other synthesis methods, mentioned in chapter 2.

In this chapter, the hypothesis of the formation mechanism of hollow gold nanoparticles is given. This study has provided the basic knowledge for the template synthesis method.

3.1 hollow Gold Nanoparticles using Nanobubble Template Synthesis Method

In order to overcome the limitation of template size and the complication of other fabrication process, simple and novel strategies are highly desired. In this research, we will introduce a new way for making the hollow gold nanoparticles, hydrogen nanobubble template synthesis method.

The synthesis process was conducted in a typical three-electrode cell, as illustrated in Figure 3.1. Similar to the commonly used electrochemical template synthesis of nanorods and nanotubes, anodic aluminum oxide (AAO) membranes were used. However, instead of one membrane, two membranes were stacked on top of each other. A commercial electroplating

sodium gold sulfite ($Na_3Au(SO_3)_2$) solution (pH~7.5) was used as the electrolyte. The pH was adjusted to about 6.0 by adding sulfuric acid or $NiSO_4$ solution.

Electrodeposition experiments were carried out in potentials below -0.6V (vs Ag/AgCl reference electrode). In addition to electrodeposition on the surface of the working electrode (at the bottom of the first membrane), the inner pore wall surfaces in all membranes were filled with distinct and well-defined gold nanoparticles. The number of these nanoparticles gradually decreases with the distance from the bottom electrode. Figure 3.1 (b) show the scanning electron micrographs of these nanoparticles as formed within the pores of the second membrane. Figure 3.1 (c) shows accumulation of gold nanoparticles on top of the electrodeposited metal on the working electrode after dissolving the first membrane by using NaOH solution.

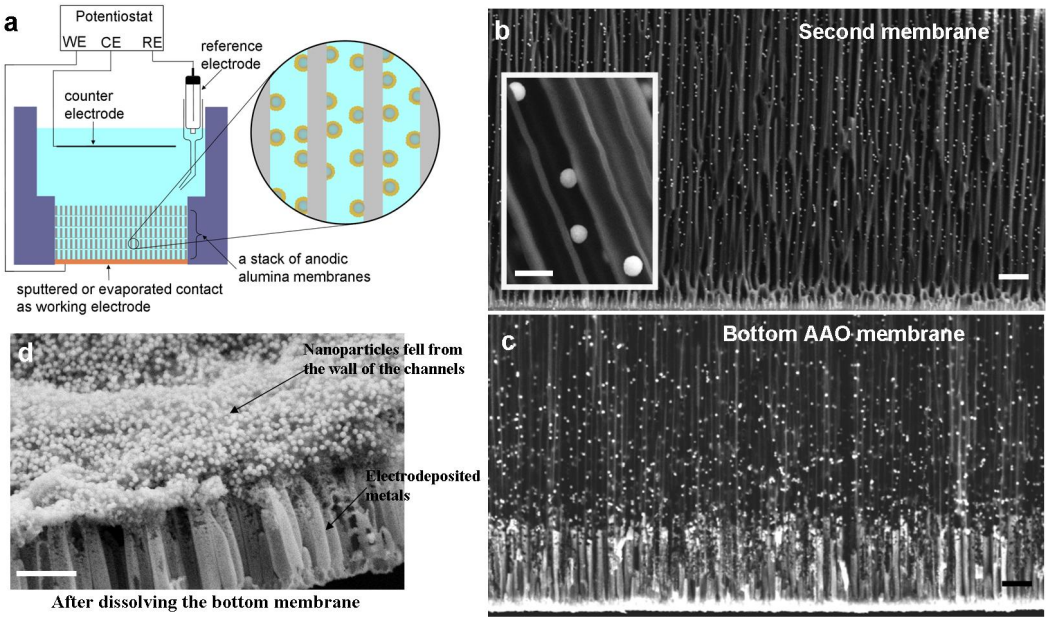

Figure 3.1 (a) the schematic of a typical three-electrode electrodeposition cell, (b) SEM image of gold nanoparticles inside the top membrane, and (c) and (d) SEM image of the gold nanoparticles on the top and inside the bottom membranes, respectively.

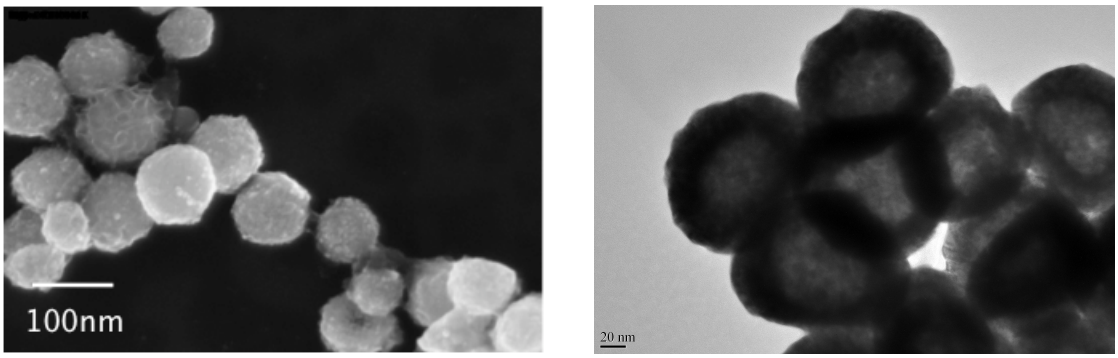

(a) (b)

Figure 3.2. (a) SEM and (b) HRTEM images of gold hollow nanoparticles

As shown in Figure 3.2, synthesizes sphere gold nanoparticle were observed using Scanning Electron Microscopy (SEM) and a hollow core inside these gold nanoparticles can be seen using High-Resolution Transmission Electron Microscopy (HRTEM), as shown in Figure 3.2(b).

A hypothesis to explain the formation mechanism of hollow gold nanoparticles has been proposed. The formation mechanism of hollow gold nanoparticles can be described as a three stage processes.

1. Hydrogen nanobubbles were electrochemically generated inside the gold (I) sulfite solution during electrodeposition when the applied potential is more negative than hydrogen evolution potential.
2. Then, hydrogen nanobubble served as templates and high concentration of hydrogen molecules at the nanobubble boundary reduced gold complex cations to form gold clusters on the hydrogen nanobubble surface, as shown in the equation (3.1) to (3.3).

$$Na_3Au(SO_3)_2 \rightarrow 3Na^+ + Au(SO_3)_2^{3-} \quad (3.1)$$

$$Au(SO_3)_2^{3-} \rightarrow Au^+ + 2SO_3^{2-} \quad (3.2)$$

$$H_2 + 2Au^+ \rightarrow 3Au + 2H^+ \quad (3.3)$$

3. After that, these gold clusters act as a catalysts to trigger the autocatalytical disproportionation reaction, as shown in the equation (3.4), so more metal gold forms and completely covers the hydrogen nanobubbles and become hollow gold nanoparticles.

$$3Au^+ \rightarrow Au^{3+} + 2Au \quad (3.4)$$

To prove our hypothesis, a silver stripe patterns on microscopy glass slide has been designed to use as a working electrode for electrodeposition to demonstrate the formation mechanism of electrochemically evolved hydrogen nanobubbles, and subsequently to generate hollow gold nanoparticles through the electroless deposition in sodium gold sulfite electrolyte as shown in Figure 3.3. In this chapter, the formation mechanism of hydrogen nanobubbles on the non-conductive area of silver stripe pattern is represented.

The silver stripe pattern was fabricated on microscopy glass substrate by photolithography technique. The silver stripe pattern is composed of 50 μm wide of conductive areas (Ag strip) and 100 μm wide non-conductive areas (glass), as shown in Figure 3.3. This bubble template synthesis process was conducted inside a typical three-electrode electrodeposition cell. A commercial gold sulfite ($Na_3Au(SO_3)_2$) electrodeposition solution (TECH-GOLD 25ESRTU, TECHNIC Inc.) was used as electrolyte. The pH of the solution is adjusted by adding sulfuric acid to about 6 to 6.5. A silver/silver chloride electrode was used as reference electrode and platinum mesh, the same diameter with deposition are, was used as counter electrode.

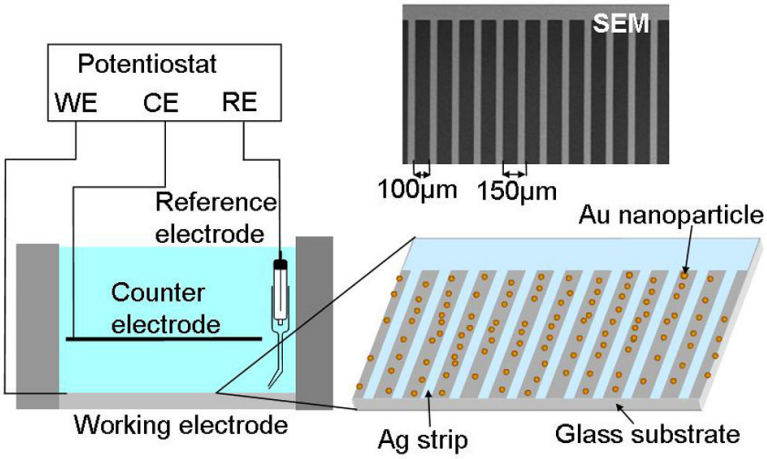

Figure 3.3 The schematic of a typical – three electrode electrochemical cell

The conductive area of working electrode, silver strip, is used to electrochemically generate hydrogen molecule in the system and hydrogen nanobubble will form inside electrolyte and on silver strip surface. However, the hydrogen bubble cannot be observed on silver strip area because the electrodeposition of gold and nickel also took place on silver strip surface. Only on non-conductive area, glass surface, the hollow gold nanoparticles can be formed by electroless reaction without the interruption of electrodeposition process. The hollow gold nanoparticles that were formed on the glass area can be used as an indicator for studying the formation mechanism of hydrogen nanobubbles. Therefore, these gold nanoparticles can give us an idea about the number, size, and shape of hydrogen nanobubbles.

Following our hypothesis, the hydrogen evolution occurs, when a potential more negative than hydrogen evolution equilibrium potential is applied to the silver strips. The concentration of hydrogen molecules will be increased and becomes supersaturated in the solution close to the electrode surface. The supersaturated hydrogen molecules are expected to form hydrogen nanobubbles on both silver strip and the glass area. (metals, 1993) (H. Riegel, 1998)

To prove such hypothesis, the experiment was conducted at -0.5V that is lower than hydrogen evolution potential -0.55V (vs Ag/AgCl). No particles were observed on the glass

area, only gold and nickel deposited on silver strip surface, as shown in Figure 3.4(a). Then, the applied potential is increased to -0.7V, that is more negative than hydrogen evolution potential, well-defined gold nanoparticles formed on the glass area, as shown in Figure 3.4(b). The applied potential is increased again to -0.9V, gold nanoparticles with well-controlled size were observed on the non-conductive area. Moreover, It was observed that the number of gold nanoparticles increases with the increasing of applied potential, as shown in Figure 3.4(c). These results have a good agreement with our hypothesis. This hollow gold nanoparticle fabrication method has a relationship of electrochemically evolved hydrogen nanobubble.

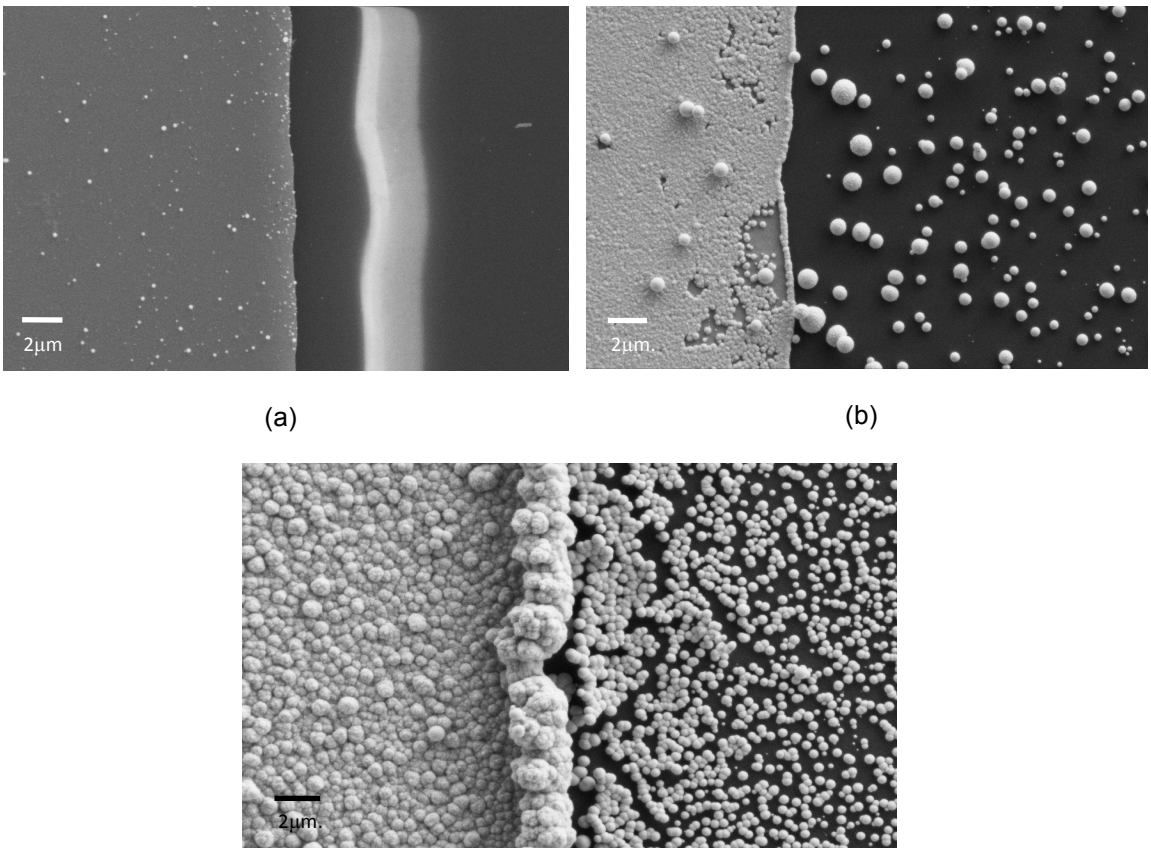

(a) (b)

(c)

Figure 3.4 The nucleation of hydrogen nanobubble at the different overpotentials, at 100 second (a) -0.5V., (b) -0.7V., (c) and -0.9V.

The formation of gold nanoparticles on the glass areas is observed when the applied potential is more negative than hydrogen evolution potential and it can be controlled by the degree of applied potential. This result indicates that the electrochemically evolved hydrogen playing a decisive role in the formation of hollow gold nanoparticles. Moreover, the applied potential also has an influence on the size and the number of nanoparticle.

From SEM images, Figure 3.4, one can see that the number of hollow gold nanoparticles increases when the negative potential is increased. On the other hand, we can see that the size of nanoparticles decreases when the negative potential is increased. The size of nanoparticles would represent the size of hydrogen nanobubble, so we can conclude that the size critical size of hydrogen nanobubbles will decrease when the overpotential is increased. These are following the classical nucleation theory, as shown in Equation 3.5, and Equation 3.6

$$r^* = -\frac{2\gamma}{\Delta\, G_v} \tag{3.5}$$

$$n^* = n_1 \exp\left(-\frac{\Delta G^*}{kT}\right) \tag{3.6}$$

From our results, it is clearly seen that the formation of hollow gold nanoparticles using this method has a close relationship with the formation of hydrogen nanobubbles. Moreover, the overpotential can be used for controlling number and size of hydrogen nanobubbles which in turn control the number and size of gold nanoparticles. The formation mechanism of hydrogen nanobubbles and the reduction of gold shells will be described in the next chapter.

CHAPTER 4

IN-SITU MONITORING HOLLOW GOLD NANOPARTICLE FORMATION MECHANISM USING PHASE SENSITIVE INTERFEROMETRY

The bubble template synthesis method composes of two main formation processes, the process of hydrogen nanobubble formation and the formation process of gold shell. We used phase sensitive interferometry (PSI) to in-situ monitoring these two processes, which is discussed in detail in this chapter. This is the first time that interferometry technique has been used for observing an electrochemical process in real time.

4.1 Phase Sensitive Interferometry

Interferometry has been used in extensive application areas of astronomy, fiber optics, metrology and biosensing. Interferometric measurements have redefined international standard of length in terms of speed of light. Interferometry is used for accurate measurements of distances, displacements, vibrations and surface topologies.

Interference signal or interferogram is formed when interference occurs between electromagnetic waves. When light is split into two paths, the split same frequency beams have exactly same properties. Light and the spectrum travel through two optical paths (sample and reference path) and reflected off, and then they are recombined. Interference occurs from superimposed reflection from the surfaces or interfaces. Interference can either be constructive for which the waves reinforce each other (in phase) or destructive where waves cancel each other (out of phase). Any optical change experienced by one path changes the phase of the light signal which when recombined with light from other unchanged path creates an interesting phenomenon of interference. Optical interference can measure optical path changes with

longitudinal resolutions better than the most sensitive surface-scanning microscopic techniques, such as atomic force microscope.

Interferometry has been utilized to detect nanoparticles. Bradled and co-worker developed an interferometric detection system that decouples amplitude and phase using two orthogonal, simultaneous measurements using passive optical elements. They have shown sensitivity to single 30-nm gold nanoparticles. For this measurement method, light is focused on a nanometric channel etched in glass and filled with the particle solution. A particle takes about 1 ms to pass through the focus, scattering light as it goes. The light is collected with a dual-phase interferometer, as shown in (a) of the figure 4.1. The optical signal is combined with a circularly polarized reference beam, and a polarizing beamsplitter directs the two orthogonal polarizations on to two detectors. Since the relative phase between reference and signal differs by 90^0 at the two detectors, amplitude and phase can be decoupled. The amplitude of the collected signal indicates signal indicates the size of the particle and contains material information. By collecting signals from many particles, they can construct histograms that represent the population of particles in a sample, as shown in (b) of the figure 4.1. Bradley et al. measured three immobilized gold particles of different sizes that are moved through the focus on a microscope coverslip. Decoupling amplitude and phase improves measurement precision drastically and effectively separates the peaks. The remaining width is due to electronic noise. (Bradley Deutsch)

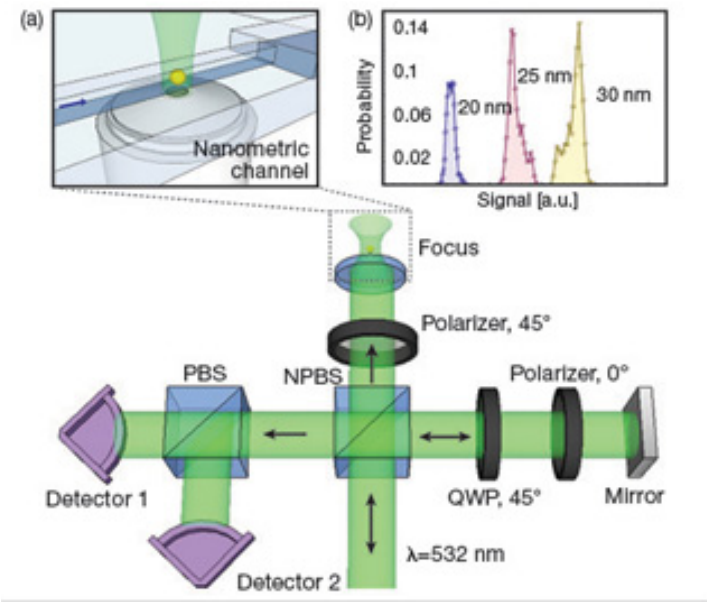

Figure 4.1 Dual-phase apparatus and histograms of particle-detection events. (a) A microscope objective focuses light onto a nanometric channel, and particles flow past. Scattered light is collected by a dual-phase interferometer. (b) Histogram showing results from three different immobilized particles.

4.2 Types of Interferometry Source

Depending on type of source used, interferometry can be categorized into 2 types: Low coherence interferometry and Laser interferometry. Due to long coherence length of Lasers, interference signal produced in Laser interferometry does not need precise path length matching. However, any stray reflections in Laser Interferometry can also generate interference pattern, which can result in incorrect measurements.

In low coherence interferometry, low coherence source with coherence length in micrometers is used. Low coherence length ensures that interference occurs only within coherence distance. The fringe visibility of interference pattern is maximum when the optical path length between two beams is matched perfectly. When optical path length (OPL) is greater than coherence length, fringe visibility decreases as the optical path length increases and completely disappears. Hence, depth resolution depends on coherence length of source; shorter coherence length gives better spatial resolution. Low coherence interferometry can be

performed in time domain or in spectral domain. In time domain low coherence interferometry, scanning mirror is used to achieve a depth probing, so recorded interferogram is a function of reflector position. Spectral domain interferometry produces interferogram as a function of wavelength and the depth information is provided form coherence grating.

4.2.1 Spectral Domain Low Coherence Interferometer (SD-LCI)

Spectral Domain Low Coherence Interferometer (SD-LCI) is a non-contact sensing modality. The interference signal obtained from low coherence light source is spatially and temporally localized which allows for measurement of small distances reflected from different layers of the sample. The SD-LCI analyses superposition of spectrums reflected from sample and reference arms and hence uses spectrometer as the detection system to measure a total intensity as a function of wavelength.

4.2.1.1 Working principle of SD-LCI

SD-LCI can be performed using either two path or common path geometry. In two-path geometry, two beams travel in physically separated paths and recombine after reflected off to produce interferogram. In common path geometry, two beams travel along the same path and recombine after reflected off to produce interferogram.

Figure 4.2 shows a simplified low coherence two path interferometric setup. As shown in the figure, light from broadband source is split into two beams using beam splitter. One beam travels towards the reference (mirror) and is reflected back. The other beam travels towards the sample and is reflected back. LCI measures the delayed echo time between the backscattered light from sample and reference path. These two beams are superimposed and create an interference pattern, which is detected by spectrometer. This interference pattern gives the information about the sample. SD-LCI cannot be used to measure a thin metal layer because of phase noise from two-path interferometer is in hundreds of nanometers. For measuring a thin metal layer, a below picometer range of noise is needed for sensitive detection.

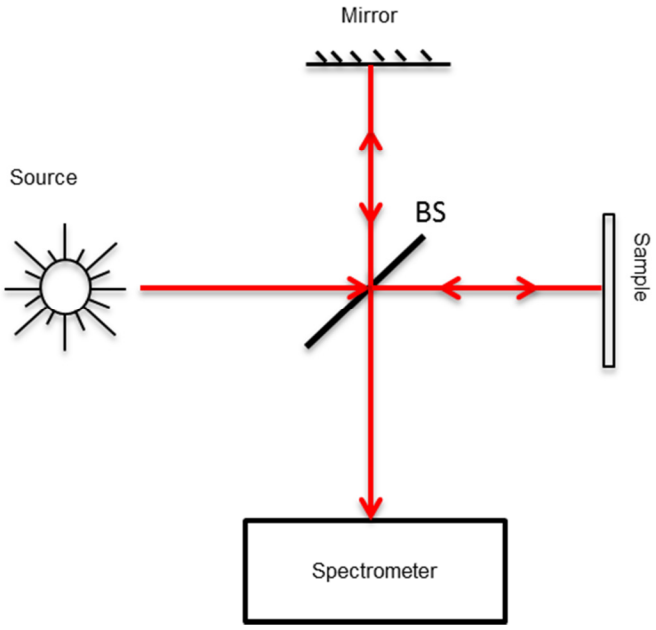

Figure 4.2 Low coherence two-path interferometric setup. Light from source is split in two using beamsplitter (BS) which after reflecting back from reference and sample path are recombined to produce interference fringes detected by spectrometer.

In order to perform sensitive phase measurements using low coherence single-path interferometry, only one path geometry is used which is shown in Figure 4.3. Both sample and reference beam travel along same path. The reference signal is generated from bottom of sample (microscopy glass slide) and sample signal is generated from top of sample. This geometry can help in quantification of phase changes that occur when there is any optical path length change in sample and hence helps in ultrasensitive detection. As compared to two-path geometry, common path interferometry is resistant to environmental factors because the environmental factors affect both reference and sample beams equally. This setup cancels noise and gives the higher stability and sensitivity system.

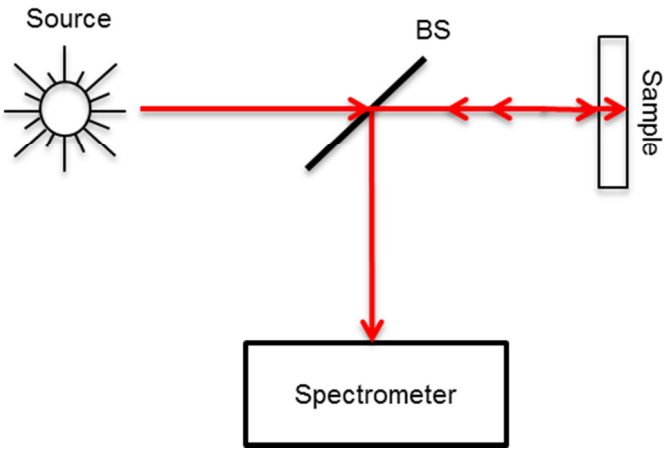

Figure 4.3 Low coherence single-path interferometric setup (common mode interferometry). Light from source is transmitted through beamsplitter (BS), which gets reflected back from top and bottom surface of sample and are recombined to produce interference fringes detached by spectrometer.

This technique is a real-time measurement with sensitivity in picometer to nanometer range. This technique can be applied for detection of a thin metal layer. Signal detected by spectrometer has interferometric component that contains information about amplitude and the phase of the sample. Extraction of phase information quantifies sub wavelength variations occurring in the sample. The phase changes occur due to optical path length (OPL) changes in the sample. Optical path length is the product of distance (L) traveled by light in media of given refractive index (n)

$$OPL = n * L \tag{4.1}$$

4.2.2 Spectral Domain-Phase Sensitive Interferometry (SD-PSI)

Fiber optic configuration of spectral domain phase sensitive interferometry is implemented in the work for phase transformation process. Fiber optic configuration offers advantages of phase difference by electromagnetic interference, flexibility of using them in different environmental conditions, and higher sensitivity.

4.2.2.1 Working Principle of SD-PSI

The SD-PSI setup consists of superluminescent diode (SLD), 635 nm visible light source, 90:10 fiber coupler, 50:50 fiber coupler and home built spectrometer. Bandwidth of the light source affects the smallest thickness of the transparent substrate that can be used and precision with which thickness of the nanobubble can be measured. The broadband SLD light source operates at 800 nm center wavelength with full-wave half-maximum (FWHW) and coherence length of 20 nm and 14 μm respectively. Fiber coupled superluminescent diodes (SLD) are an excellent choice as broadband light sources for SD-PSI. These compact sources have a stable spectral and power output. Given the potential of damage to the SLD due to back-reflection from the optical setup, a fiber isolator should be inserted between the SLD source and the input port of the 2x2 SMF coupler. The isolator in the system is incorporated to protect SLD source from back reflections that can damage or create instability in performance of SLD source. After isolator light is input in single axis fiber bench. This is used to attenuate the power on the sample when signal goes in saturation.

The output port of fiber act as input to 90:10 fiber coupler. To other input arm of coupler, 635 nm red light source is connected to visualize the light focused on the sample. The arm with 90% of power is coupled into a 2x2 (50:50 split ratio) single mode fiber (SMF) splitter. The second coupler splits power equally in two sample paths. As shown in Figure 4.4, in the common path configuration only one port of the coupler is used for sensing. Any broadband light source can be used as long as the spectrum of the light source is stable and sufficient light can be coupled into a single mode fiber. This single mode fiber maintains a signal-to-noise ratio that is necessary to detect a desired phase change in the special interference fringes. The port that is not used should be angle polished or angle cleaved to avoid any back reflection from the fiber-air interferometric signal. The other port of the fiber coupler should be terminated with a FE/APC connector.

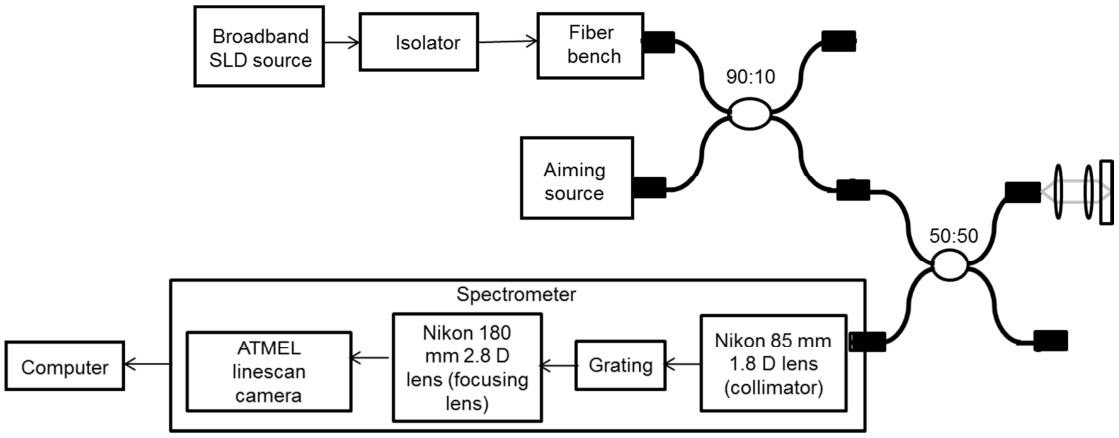

Figure 4.4 Optical setup of spectral domain phase sensitive interferometer. 90:10 coupler splits combined power of 800 nm and 635 nm Laser in 90:10 ratio. 90% is input to 50:50 coupler which after reflecting back from sensor surface is detected by spectrometer. Computer stores acquired interference spectrums.

Light from the fiber port is first collimated and then focused onto the sample surface. The light is reflected back from reflective surfaces to detector. The interference signal caused due to the light reflecting back from the reflective surfaces of the sample is coupled to a home built spectrometer.

In home built spectrometer, light input to spectrometer is first collimated and is then directed to diffraction grating (1200 lines/mm). Diffraction grating splits the light into its frequency components. Focusing lens is used to focus light on CCD camera. The spectrally dispersed output of spectrometer is captured by attached 12-bit line scan camera CCD records the amount of light that hits each pixel and converts to voltage level. As camera is 12 bit, each pixel in the camera can handle 4096 brightness units. The camera communicates with Ni 1428 camera link acquiring digital frames and stores them on system hard drive. The spectrometer can acquire 20 K spectra/sec with a resolution of 0.06 nm.

A simple and robust setup for the sample path optics would be to mount all the opto-mechanical components on a cage system, as shown in Figure 4.5 and Figure 4.6. Optical

components are mounted on cage plates and kinematic mirror mount to enable make fine adjustment of collimated beam tip and tilt orientation with respect to the focusing lens.

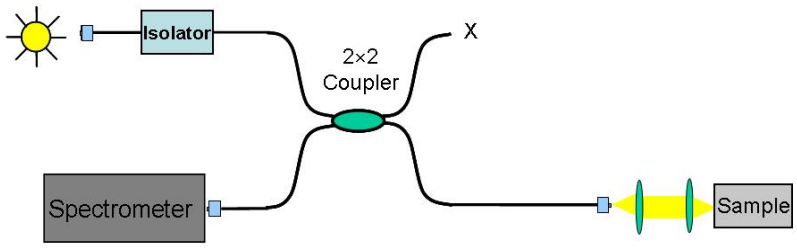

Figure 4.5 Setup of a fiber-based spectral domain phase sensitive interferometer.

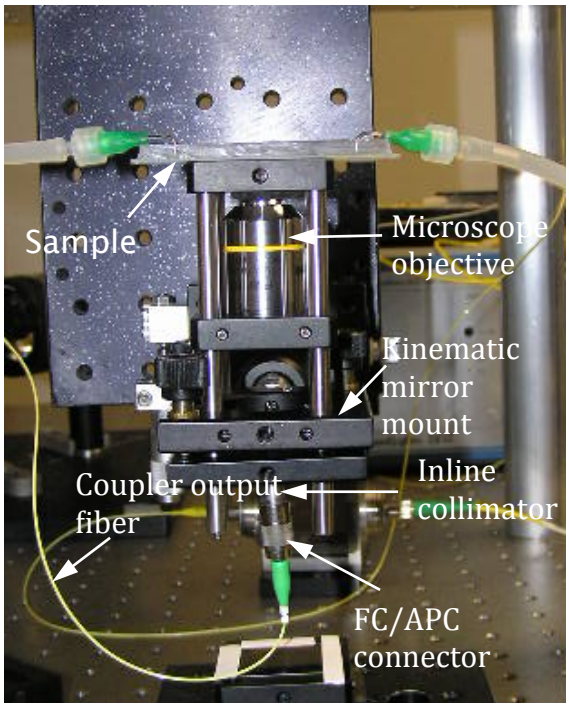

Figure 4.6 Photograph of the SD-PSI sample path configuration showing various components.

Suitable sample geometry for SD-PSI measurement is any transparent substrate (glass or plastic) of suitable thickness. The thickness of the transparent substrate that can be used is only limited by the resolution of the spectrometer used in the setup. The spectral modulation frequency is proportional to the thickness of the substrate and the deposited layer. In the sample optical configuration shown in Figure 4.7, light will reflect back onto the interferometer

from the interface 1, interface 2, and interface 3. Spectral modulation of various frequencies will occur due to interference between light reflections of the ratio of the reflectivities of the two interfaces involved. Interference will also occur due to multiple reflection of light from the various interfaces by the modulation depth is far smaller than the primary interference signal and the modulation frequency will be a multiple of the primary modulation frequency. Each interference signal occurs at a fixed spatial frequency band that is proportional to the optical thickness of the interfaces involved and can be measured by Fourier transformation of the recorded spectral interference.

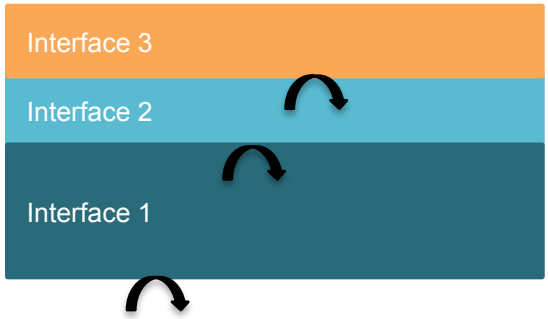

Figure 4.7 the optical configuration of the formation of hollow gold nanoparticles in a interferometry.

In the case hollow gold nanoparticles formation study (Figure 4.8), recording of kinetics and ultimately the detection of hollow gold nanoparticles formation can be achieved by measuring the optical thickness changes that occurs due to formation of hydrogen nanobubble layer 2 with the deposition of gold shell to the recognition of layer 3. The spectral interference signal of interest is the interference signal that occurs between interface 1 and 3 or 2 and 3 or 1 and 3. Even if one atom layer of metal deposit to the recognition site a change in the phase of the interference signal will occur. When any other test sample with different refractive index is introduced, there is shift in phase of the multiplexed interference signal. This change is seen by all reflective surfaces. In this example all interference patterns will show a phase shift. The phase change can be extracted from any of the above surfaces, to quatify the change in reflective index. As no deposited layer on the glass surface, a constant physical length is

assumed. Hence any shift in phase signal is attributed to change in refractive index that occurs on substrate surface

4.3 In Situ Study of the Formation of Hollow Gold Nanoparticle Using Phase Sensitive Interferometry Technique

From our hypothesis, hydrogen nanobubbles are electrochemically generated inside the gold (I) sulfite solution during electrodepostion. Then, hydrogen nanobubble served as template and the high concentration of hydrogen molecules at the nanobubble boundary reduced gold cation to form gold clusters on the hydrogen nanobubble surface. After that, these gold clusters act as a catalysts to trigger the autocatalytical disproportionation reaction, so more metal gold forms and completely covers the hydrogen nanobubble and become the hollow gold nanoparticle.

A silver stripe patterns as shown in Figure 3.2 on microscopy glass slide has been used as a substrate to in-situ monitor the whole process using PSI. The silver stripe pattern is composed of 50 μm width of conductive area (Ag strip) and 100 μm width of non-conductive areas (glass). The formation mechanism of hydrogen nanobubbles and the formation of gold shell occur on the non-conductive area of silver stripe pattern. Therefore, this non-conductive area is the target area for PSI. The silver stripe pattern substrate is fit on the bottom of electrochemical cell, as shown in Figure 4.8. The electrochemical cell is placed at the sample position, shown in Figure 4.6. Then, light is focused onto the non-conductive glass area in the stripe pattern substrate. During the electrodeposition, the light reflected back from reflective surfaces have been detected and recorded. The interference signal caused due to the light reflecting back from the reflective surfaces of the sample is coupled to a home built spectrometer.

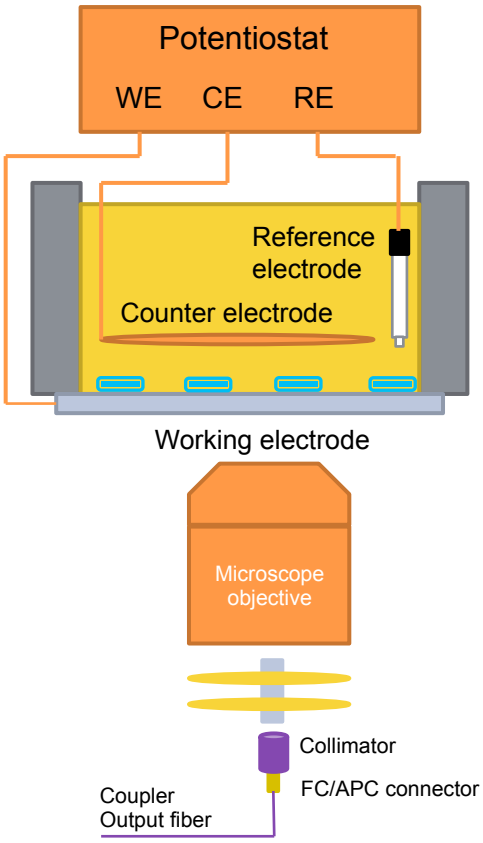

Figure 4.8 The schematic of PSI and electrochemical setup for in situ study of the formation mechanism of hollow gold nanoparticles.

Figure 4.9 shows a simplified spectral domain phase sensitive interferometry setup. During measurement, light incident on the coverslip is reflected from bottom of the glass slide (air-glass interface) and top of the glass slide (glass-electrolyte interface) as shown in Figure 4.9. Two beams of reflected light interfere and the interference pattern (green) is recorded as an original modulation as shown on top right panel of Figure 4.9.

After hydrogen nanobubble formed, the source of reflective surface change. Reflections now occur at the interface of air-glass substrate, glass-nanobubble and the nanobubble-electrolyte resulting in the interference signal (gray). The fringe shifted with respect to the previous interference pattern as shown by middle right panel of Figure 4.9. When the gold shell starts to form on hydrogen nanobubbles surface, the shift occurs again due to the changed in

the optical path length as a result of the physical increase in thickness caused by the hydrogen nanobubble layer and gold shell formation onto the glass slide surface and the amplitude of the modulation is increased due to the refractive index of gold shell (red), as shown by bottom right panel of Figure 4.9.

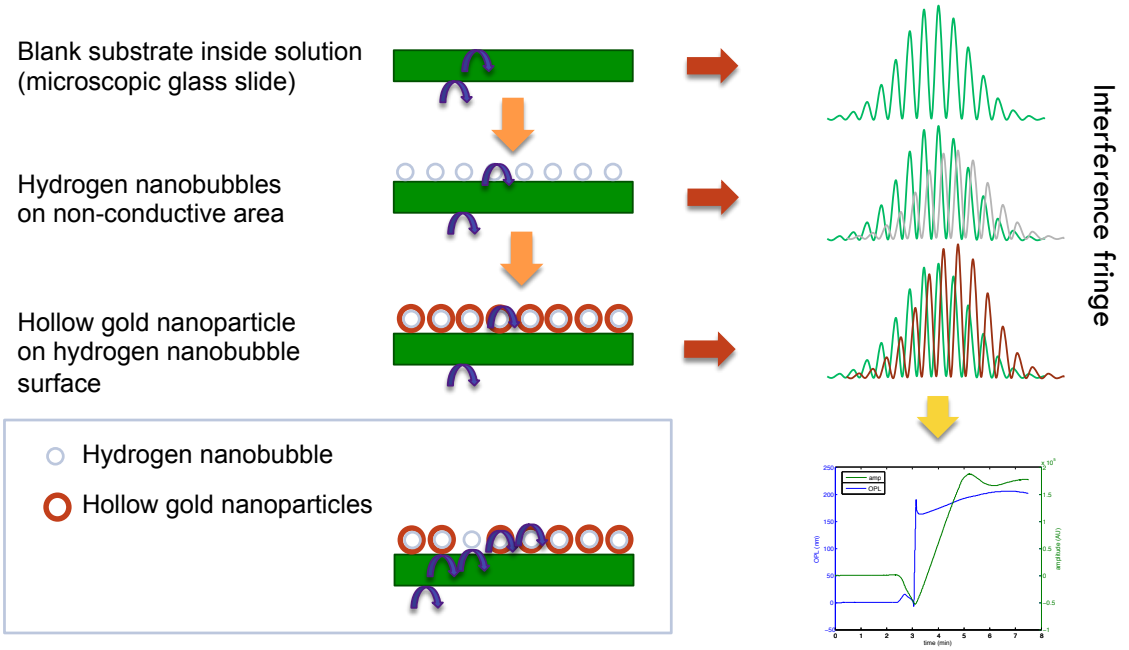

Figure 4.9 Cartoon illustration of working principle of SD-PSI. Upper panel shows the source of reflective surfaces for interference from hydrogen nanobubbles. The bottom panel shows change in reflective surfaces after gold ions deposited on hydrogen nanobubbles surface causing shift in the interference pattern.

The sub-wavelength change in the length due to reaction can be precisely quantified as change in phase. When light is focused on the optically clear coverslip, light is reflected from the top surface of the coverslip and then again from the bottom surface of the coverslip. In spectral domain systems, the time varying signal along the optical axis is converted into the frequency Fourier domain. Then, these two beams are combined to form interference signal. This interference signal can be mathematically represented by equation 4.2.

$$S(k) = S_0(k)\{R_1 + R_2 + \sqrt{R_1}R_2|\mu(k)|cos(4\pi\Delta pk)\} \quad (4.2)$$

where, $S_0(k)$ is incident spectral intensity, R_1 and R_2 are reflectivities of two surfaces, μ_k is the spectral degree of coherence which is assumed one as the light exiting a single mode fiber is spatially coherent, Δp is optical path length difference between the two surfaces and k is the wave number. The cosine term is equation 4.2 causes modulation in the signal, which is function of optical path length difference between two reflective surfaces of the coverslip. Fourier transforming equation 4.2 can quantify the magnitude of the reflected light as a function of optical path length difference between two reflective surfaces of the sensor.

$$\Delta\varphi = tan^{-1}\left\{\frac{Im\,F(S(k))}{Re\,F(S(k))}\right\} = \frac{4\pi\Delta p}{\lambda_0} \tag{4.3}$$

From Equation 4.3, change in the phase of interference signal due to hydrogen nanobubble and gold nanoparticle formation can be related to the change in the optical path length. Here λ_0 is center wavelength of the low coherence source. The phase change that occurs when hollow gold nanoparticles form depends on OPL change that in turn depends on size and refractive index of hydrogen nanobubble and gold shell on the substrate surface.

4.4 Results and Discussion

The formation of hollow gold nanoparticles took place when the applied potential is higher than hydrogen evolution potential and the hydrogen nanobubbles form as shown in Figure 4.10. The changing in OPL are seen from PSI due to change in physical length on the surface of the coverslip. The modulation pattern from the light reflected from top and bottom surface of coverslip without deposition was recorded to be an original modulation. As hydrogen nanobubbles and nanoparticles form on interface 1, the refractive properties of interface 1 will changes. There is a change in OPL and amplitude of reflected light, as shown in Figure 4.10.

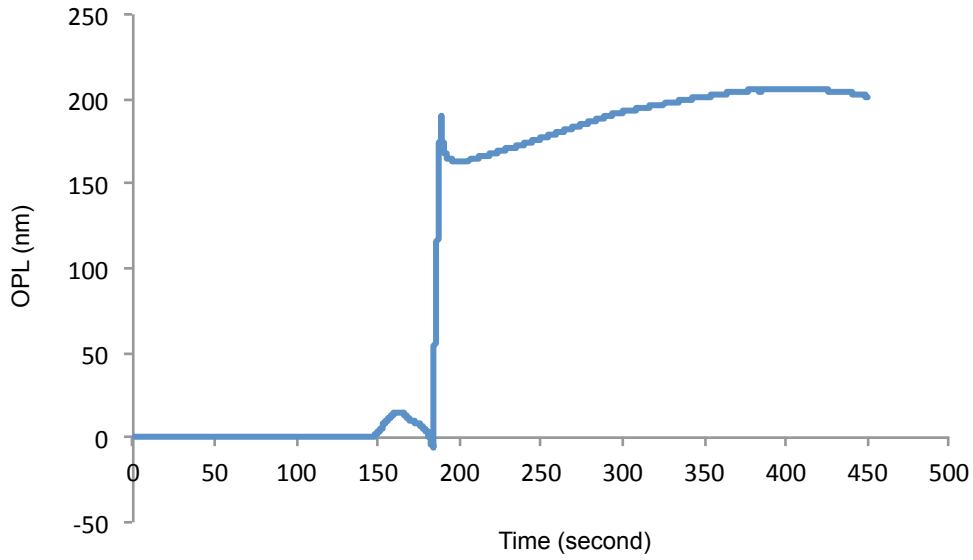

Figure 4.10 The phase shift due to the formation of hydrogen nanobubbles and gold shells.

As shown in Figure 4.10, after 150 seconds of applying potential to the substrate, hydrogen nanobubbles form, which changes the optical path length difference and be detected using PSI. After 180 seconds, the optical path length difference dramatically increases. This is due to the formation of gold shells. This result can be confirmed by detecting the amplitude changed of reflected light, as shown in Figure 4.11. After 150 seconds, the amplitude of modulation is decreasing. This result shows that hydrogen nanobubbles formed on the top of substrate surface, the light is scattered away by hydrogen nanobubbles, causing less light to get into the detector. After 180 seconds, the amplitude of modulation starts to increase, resulting from the fact that gold shell reflects much more light. This result is confirmed ex-situ by examining the glass area after the deposition using scanning electron microscopy (SEM), as shown in Figure 4.12

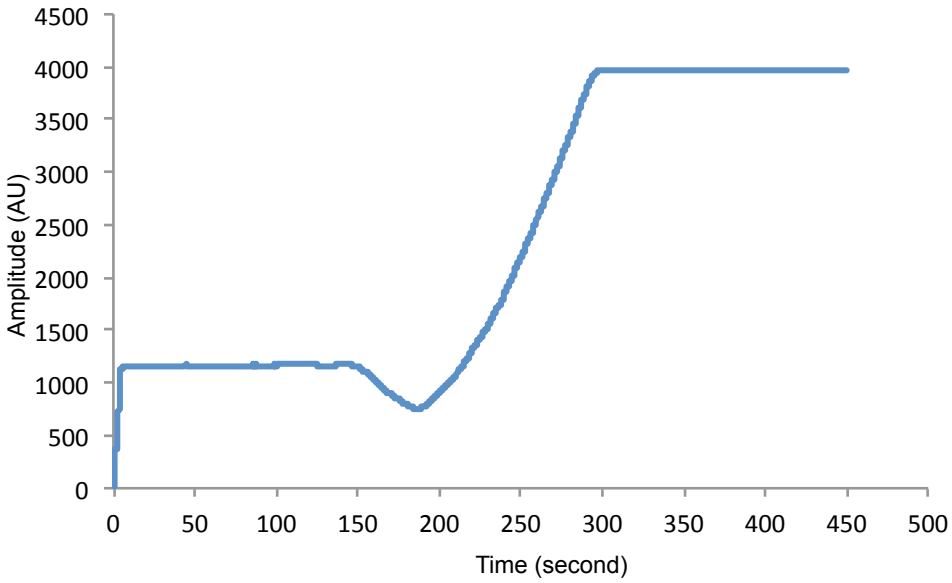

Figure 4.11 The amplitude changed due to the formation of hydrogen nanobubbles and gold shells.

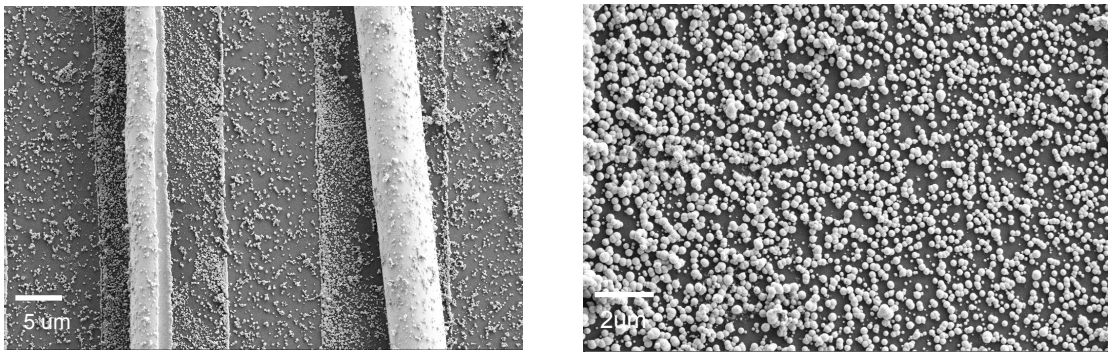

(a) (b)

Figure 4.12 SEM images of hollow gold nanoparticles on silver stripe pattern substrate after it was in-situ studied using Phase Sensitive Interferometry.

The hydrogen evolution process should occur immediately when the overpotential was applied. From PSI, hydrogen nanobubbles was detected when the deposition is around two and a half minutes. This can be explained that the hydrogen molecules need time to reach supersaturation to form hydrogen nanobubbles. Then, after three minutes, a deposited gold metal on hydrogen nanobubbles surface was detected showing a dramatically increasing of

amplitude. These results are direct confirmation of our hypothesis that hydrogen nanobubbles are first electrochemically generated inside electrolyte and serve as templates for gold deposition.

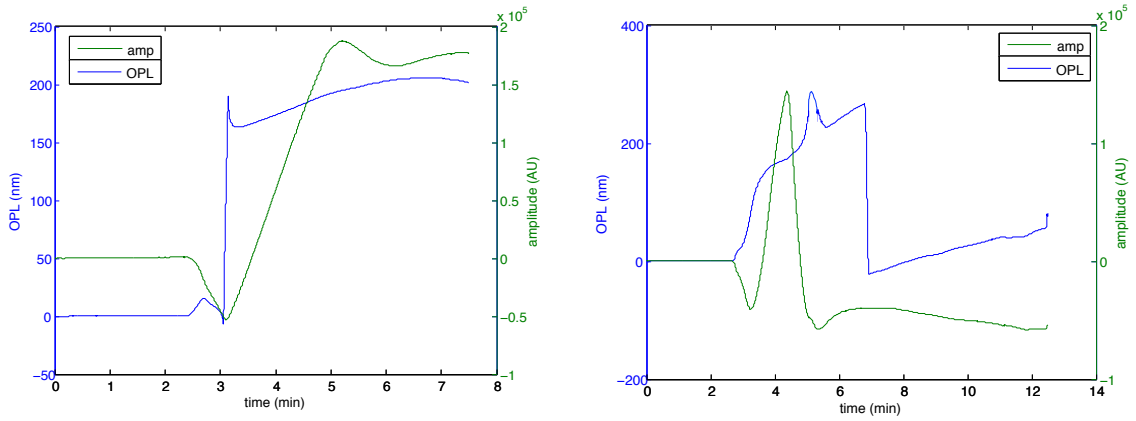

(a) (b)

Figure 4.13 The change of interference due to the formation of hollow gold nanoparticles in Phase Sensitive Interferometer

From these PSI results, we can see that the detection of hollow gold nanoparticles formation can be clearly achieved by measuring the optical thickness changes that occurs due to formation of hydrogen nanobubble and the deposition of gold shell. Therefore, we believe that this PSI technique has the potential for in-situ study of other electrochemical deposition process.

CHAPTER 5

SIZE AND MORPHOLOGY CONTROL OF HOLLOW GOLD NANOPARTICLES

The optical properties of hollow gold nanoparticles are strongly dependent on the size, shape, and morphology of shell structure. The bubble template synthesis method can create a large amount of hollow gold nanoparticle with well-controlled size, hollow dimension, and shell structures. In this chapter, the effects of electrolyte composition and electrodeposition conditions on, particle size, core size and shell structure of hollow gold nanoparticles are discussed.

5.1 Experiment Setup for Ex-Situ Study of Gold Nanoparticles

In chapter 3 and 4, the silver stripe pattern substrates have been used for studying the formation mechanism of hollow gold nanoparticles. It is clearly seen that in these experiments, the size of hollow gold nanoparticles cannot be controlled, as shown in Figure 5.1 Hydrogen nanobubbles are nucleated from the supersaturation mechanism of hydrogen molecule and the formation of hydrogen bubbles is a typical nucleation and growth process of a second phase precipitation. Hydrogen evolution includes several atomic processes. Protons from solution combine with electrons at the conductive area to form hydrogen atoms, which are chemisorbed at the electrode surfaces and form H_2 molecules. H_2 molecules dissolve in the electrolyte and become supersaturated in the solution close to the electrode, from which H_2 bubbles nucleate on the electrode surface. As a result, the size and number of gold nanoparticles next to conductive area is larger than in the middle of non-conductive area. However, gold nanoparticles on conductive area are also created but it is rarely observed the electrodeposition of gold and nickel on conductive area covers those bubbles. Additionally, gold nanoparticles on non-conductive area and inside solution can freely move, so it is easier to create the

aggregation of gold nanoparticle. As shown in Figure 5.1, the distance from conductive area affect on the size of gold nanoparticles.

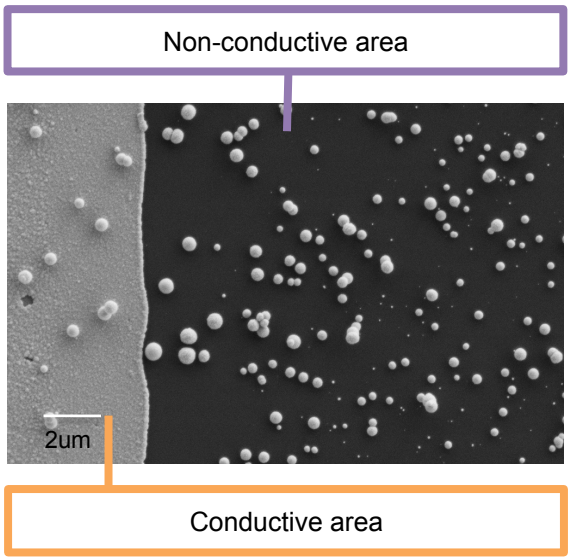

Figure 5.1 The effect of mass transfer on hydrogen nanobubble nucleation

Anodic Alumina Oxide (AAO) membranes were employed for synthesizing hollow gold nanoparticles with well-controlled sizes. The synthesis of hollow gold nanoparticles using AAO membranes was also conducted inside a typical three-electrode electrodeposition cell, as shown in Figure 5.2. The same commercial gold sulfite electrodeposition solution (TECH-GOLD 25ESRTU, TECHNIC Inc.) was used as electrolyte. Anodic Alumina Oxide membranes (AAO) were used as working electrode to synthesize hollow gold nanoparticles. The AAO membranes used were Anadisc^{TM} 13 (Whatman Ltd.) membrane disks with a macroscopic diameter of 13 mm. This kind of AAO membrane consists of 200 nm diameter and 60 microns length channels. One side of the channel opening of AAO is covered by a 400 nm thick of evaporated copper film. Another AAO membrane on the top of the bottom membrane act as the non-conductive substrate to capture electrochemically evolved hydrogen nanobubble and subsequently to produce a large number of separated hollow gold nanoparticles. The inner pore wall surfaces in

all membranes are filled with distinct and well-defined gold nanoparticles. The number of these nanoparticles decreases with the distance from the bottom electrode.

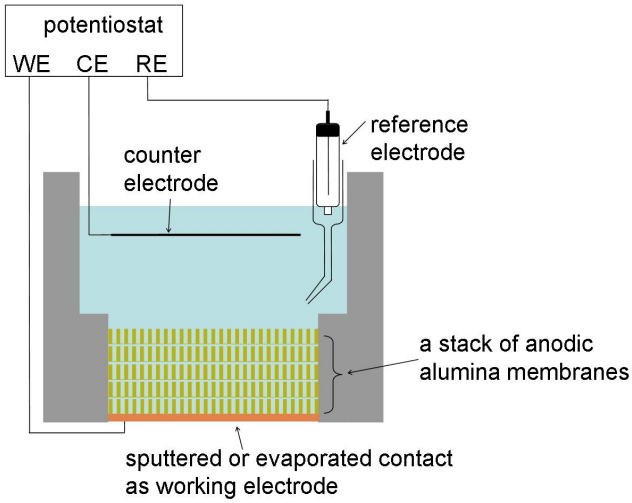

Figure 5.2 The schematic of a typical – three electrode electrochemical cell for Anodic Aluminum Oxide Membrane (AAO)

The top AAO membranes were dissolved by 2M NaOH to release hollow gold nanoparticles. Nanoparticles were then cleaned with deionized water by using centrifugation and sonication, respectively. The cleaning process has been repeated at least 5 times. After that, SEM and TEM were used for ex-situ studying the microstructure of these nanoparticles.

From SEM images, Figure 5.3 (a) and (b), both of half-spheres and completely spheres shape are found inside the top membrane. These results show that the nucleation of hydrogen nanobubbles can occur on pore wall and also inside channels. This is in a good agreement with the classical nucleation theory.

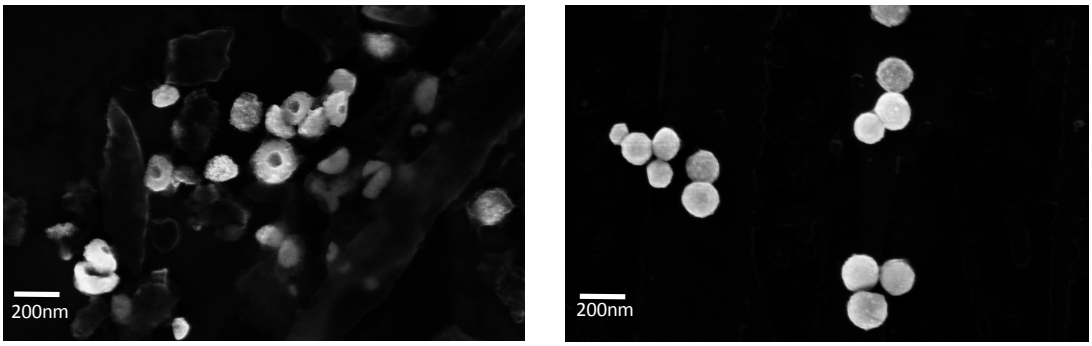

(a) (b)

Figure 5.3 Half-sphere (a) and completely sphere gold nanoparticles (b) from the top AAO membrane.

5.2 Classical Nucleation Theory

According to the classical nucleation theory, the nucleation can be categorized into two types: homogeneous and heterogeneous nucleation. Homogeneous nucleation occurs in the bulk of the solution away from any interface such as walls and particles. For heterogeneous nucleation, nuclei form at preferential sites such as phase boundaries, impurities or wall surfaces. Heterogeneous nucleation usually requires much less energy than homogeneous nucleation.

5.2.1 Homogeneous Nucleation

For the homogeneous nucleation, the net free energy changes in the system when a bubble forms inside the liquid phase. The net free energy consists of two contributors: the "surface" term and "volume" term. The surface term is due to the energy that is required to form a gas-liquid interface of a bubble, which is having a radius r and specific surface free energy γ in the form:

$$\Delta G_s = 4\pi r^2 \gamma_{VL} \tag{5.1}$$

$$\Delta G = \frac{4}{3}\pi r^3 \Delta G_v \tag{5.2}$$

$$\Delta G_r = \Delta G_s + \Delta G \tag{5.3}$$

$$\Delta G_r = 4\pi r^2 \lambda_{VL} + \frac{4}{3}\pi r^3 \Delta G_v \tag{5.4}$$

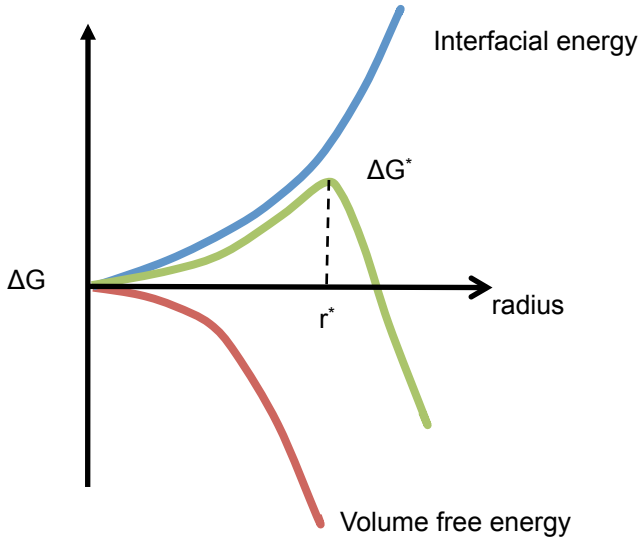

Figure 5.4 Free energy of a bubble in liquid as a function of its radius

The energy function is plotted against the bubble size for a typical case in Figure 5.4. The curve rises to a sharp maximum in positive free energy, the "critical energy" (ΔG^*) at a well-defined bubble radius, which is called the "critical bubble size" (r^*) before falling to a negative free energy and thus a stable state. The positive peak in Figure 5.4 is due to the great energy cost of forming a gas-liquid interface. The sharp drop in energy for a larger bubble is caused by the negative chemical potential term in equation 5.2. Bubbles that are smaller than the critical size will tend to disappear spontaneously, whereas bubbles of the critical or larger size will have a strong driving force to grow. As will be seen the location and magnitude of this energy barrier that depend heavily on gas supersaturation and surface tension. (P. K. Weathersby, 1982) (Katz, 1975) (Peter G. Bowers, 1995) The critical radius relation may be obtained by setting the derivative of equation 5.4 to zero and solving for r^*, which becomes equation 5.5 and the critical free energy becomes equation 5.6, respectively. (Oxtoby, 1998)

$$r^* = \frac{2\gamma_{VL}}{\Delta G_v} \tag{5.5}$$

$$\Delta G^* = \frac{16\pi\gamma_{VL}^3}{3(\Delta G_v^2)} \tag{5.6}$$

$$J = Z\exp\left[-\frac{16\pi\gamma_{VL}^3}{3kT(\Delta G_v^2)}\right] \tag{5.7}$$

$$J = Z\exp\left[-\frac{\Delta G^*}{kT}\right] \tag{5.8}$$

The rate of bubble production in a particular volume of fluid, J can also be calculated, where. Z is a pre-exponential term or frequency factor referring to the speed with which gas molecules can rearrange in solution and thus collect in sufficient numbers to form a bubble. ΔG^* is the free energy difference between the dissolved and critically nucleated states (Peter G. Bowers, 1995) (Debenedetti, 2003) (McGraw, 1996) According to equation 5.8, the number of nanobubbles will be increased by increasing the overpotential.

5.2.2 Heterogeneous Nucleation

For heterogeneous nucleation, nuclei form at preferential sites, as show in Figure 5.5. Heterogeneous bubble nucleation requires less dissolved gas supersaturation than homogeneous nucleation in the bulk. This phenomenon can be explained by considering two main parameters, the contact angle of solid-gas-liquid interface (θ) and the nucleation site. The free energy of heterogeneous nucleation depends on the surface properties of substrate. (Vincent Stuart, 2011)

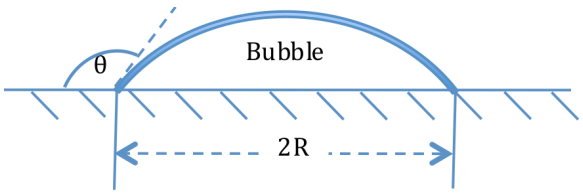

Figure 5.5 The schematic of heterogeneous nucleation on the solid surface

$$\Delta G^{het} = \Delta G^{\hom} \cdot f(\theta) \tag{5.9}$$

Where $\Delta G^{\hom}$ is the free energy of a spherical nucleus of radius equal to the radius of the cap and $f(\theta)$ is given by:

$$f(\theta) = \frac{2 + 3\cos\theta - \cos^3\theta}{4} \tag{5.10}$$

The variation of the ratio of ΔG^{het} to $\Delta G^{\hom}$ is the same as value as the function of contact angle as shown in Equation 5.9. In the other words, the competition between $\Delta G^{\hom}$ and ΔG^{het} depends on the properties of surface, hydrophobic or hydrophilic surface. For example, if the substrate is hydrophilic materials, θ = 10°, the liquid almost completely wets the surface and $\Delta G^{het} = 0.99983\Delta G^{\hom}$. Conversely, at θ of 170° (hydrophobic surface) yields $\Delta G^{het} = 0.00017\Delta G^{\hom}$. Thus, a surface that has poor wetting characteristics (i.e. $\theta \rightarrow 180^{\circ}$) should promote heterogeneous nucleation much more easily than well-wetted surface.

For the case of bubble nucleation from a dissolved gas in a solution, Equation 5.8 can be modified to take account of variations in contact angle as:

$$J = Z \exp\left[-\frac{\Delta G^*}{kT} \cdot f(\theta)\right] \tag{5.11}$$

There is a small change in contact angle in this case, that results in large negative values from the exponential term. Therefore much less supersaturation of dissolved gas is needed to cause heterogeneous nucleation than it is needed for homogeneous nucleation.

(Westwater, 1964) Following the classical nucleation theory, gold nanoparticles can nucleate both on pore wall and inside gold solution by deposited on both homogeneous and heterogeneous hydrogen nanobubble boundary.

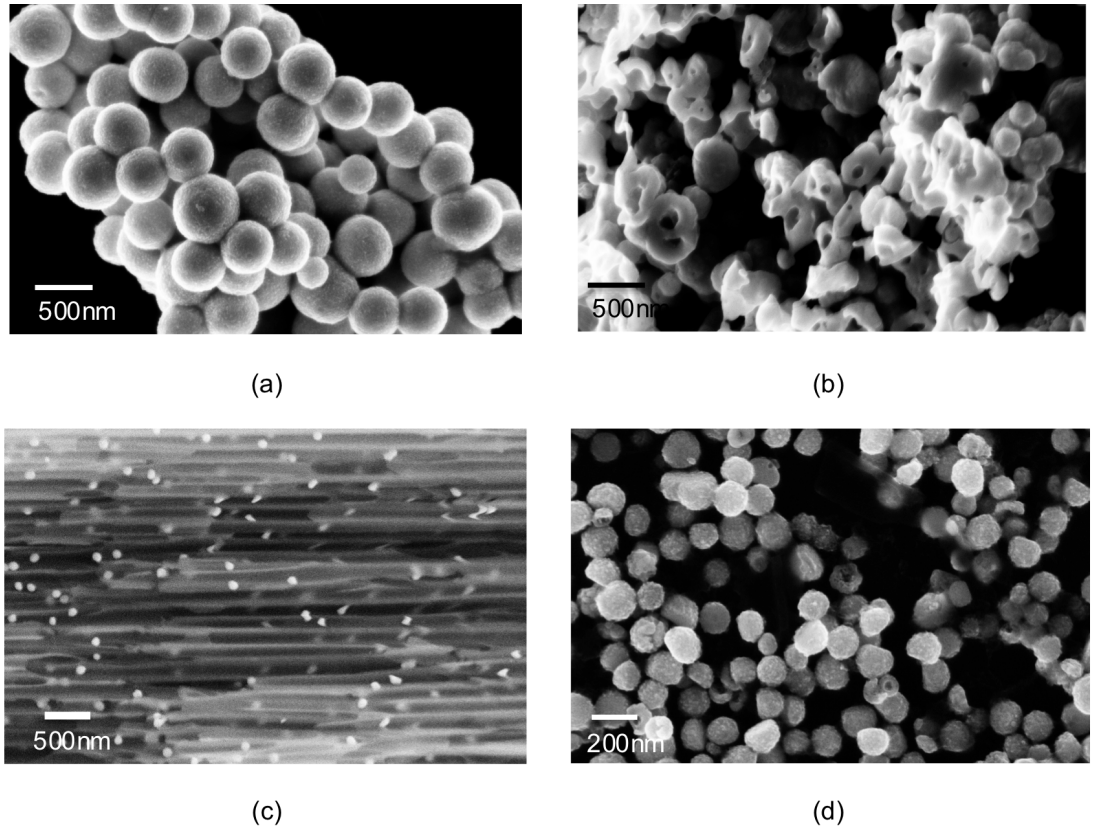

Figure 5.6 (a) and (b) gold nanoparticles inside deposited gold solution, (c) and (d) gold nanoparticles inside AAO membrane

To confirm such hypothesis, gold solution has been collected after electrodeposition process and gold nanoparticles were found in the solution. These nanoparticles were cleaned inside deionized water by centrifugation and sonication, and then were cross-sectioned using ion milling and SEM micrographs were taken. As shown in Figure 5.6 (a), it clearly shows the hollow structure. From this result, it can be confirmed classical nucleation theory that hydrogen nanobubbles also nucleate inside solution by homogenous nucleation. Moreover, gold nanoparticles inside AAO template also have both half-sphere and completely-sphere shape, as

shown In Figure 5.6 (c) and (d). There are nucleated by both heterogeneous nucleation and homogeneous nucleation inside the channels.

5.3 Effect of Process Parameters on the Formation of Hydrogen Nanobubbles

Following our hypothesis, the formation process of hollow gold nanoparticles using hydrogen nanobubble template synthesis method can be separated into two integrated electrochemical processes: 1) hydrogen evolution and 2) electroless deposition around the hydrogen bubbles. In this section, parameters that affect both processes will be discussed.

First, electrochemically generated nanobubbles on electrode surfaces have to be investigated. The synthesis parameters in the formation of hydrogen nanobubbles include: 1) applied potential, 2) hydrogen evolution enhancer, 3) deposition time, and 4) the diameter of template channel.

5.3.1 Applied Potential

Hydrogen evolution occurs electrochemically at a potential more negative than the H^+/H_2 equilibrium potential (e.g. -0.55V vs Ag/AgCl at pH 6.0). But the formation of hydrogen bubbles is a typical nucleation and growth process of a second phase precipitatation. Hydrogen evolution includes several atomic processes. Protons from solution combine with electrons to form hydrogen atoms, which are chemisorbed at the electrode surfaces and form H_2 molecules. H_2 molecules dissolve in the electrolyte and become supersaturated in the solution close to the electrode, from which H_2 bubbles nucleate on the electrode surface. Bubble nucleation requires certain supersaturation level of hydrogen molecules, which is dependent on the overpotential (the difference between applied potential and equilibrium potential).

Following classical nucleation theory, the critical nucleus size is inversely proportional to the supersaturation. As applied potential become more negative than the equilibrium potential, supersaturation increases, and critical nucleus size decreases, resulting in smaller nanobubbles. The void size of hollow gold nanoparticles can be used as a measure of the

critical nucleus size of the hydrogen nanobubble, assuming electroless deposition of gold metal takes place immediately after the formation of the bubbles.

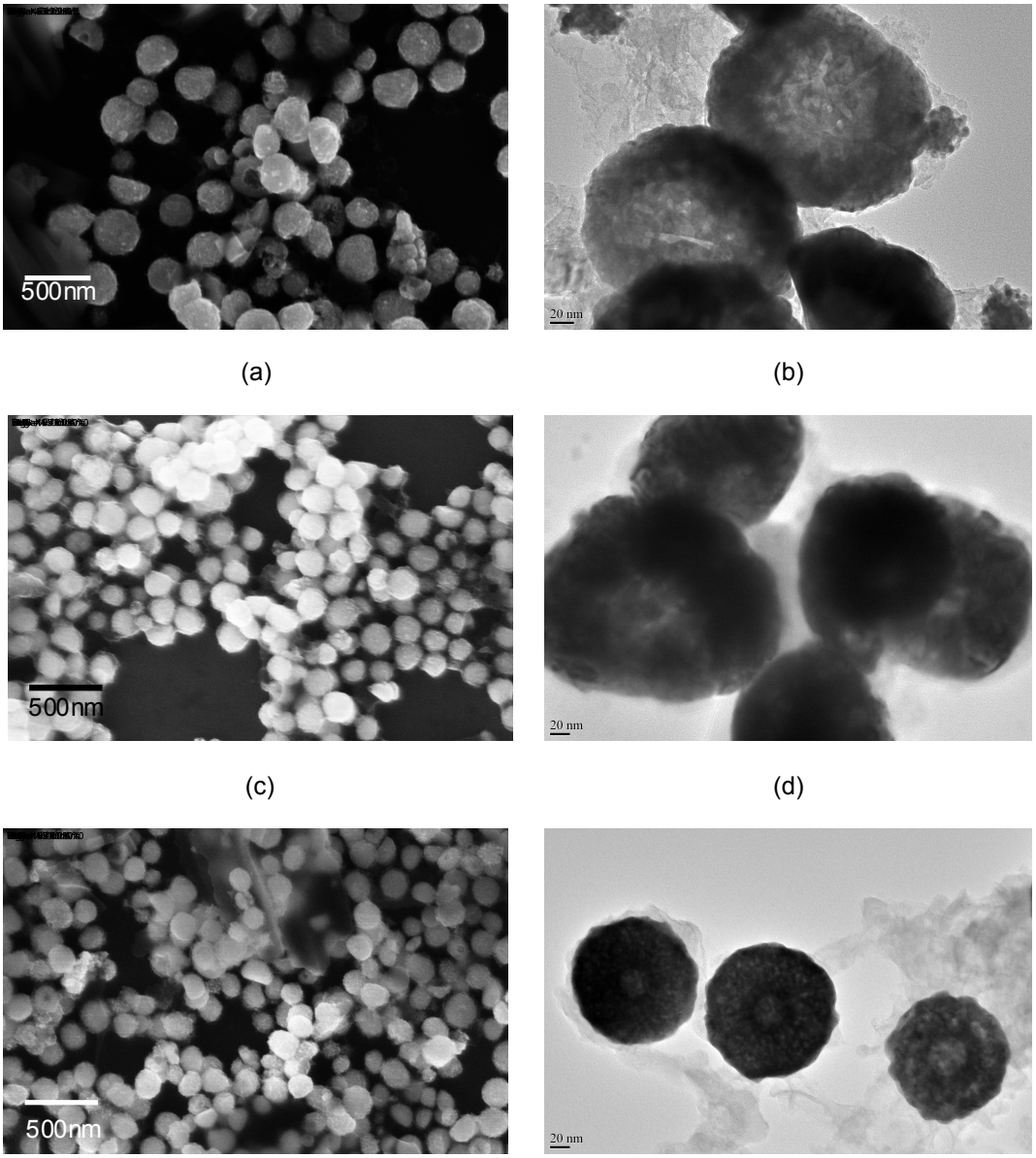

Figure 5.7 The nucleation of hydrogen nanobubble at the different overpotentials, at 800 second (a) and (b) -0.7V., (c) and (d) -0.8V., and (e) and (f) -0.9V.

Gold nanoparticles from AAO template have the same trend with gold nanoparticles from the stripe pattern substrate. When the negative potential is increased, the number of

hydrogen nanobubble increases but the size of nanobubbles decreases. Therefore, the size and the number of gold nanoparticles can be controlled by deposition potential, as shown in Figure 5.7.

5.3.2. Hydrogen Evolution Enhancer.

Hydrogen evolution can be enhanced by adding a hydrogen evolution enhancer into the electrolyte. It is known that Ni metal can significantly increases the hydrogen evolution efficiency. With the addition of Ni^{2+} ion in the electrolyte, electroplated nickel metal is exposed on the electrode surface during the electrodepposition, which greatly increases the formation rate of H_2 molecule.

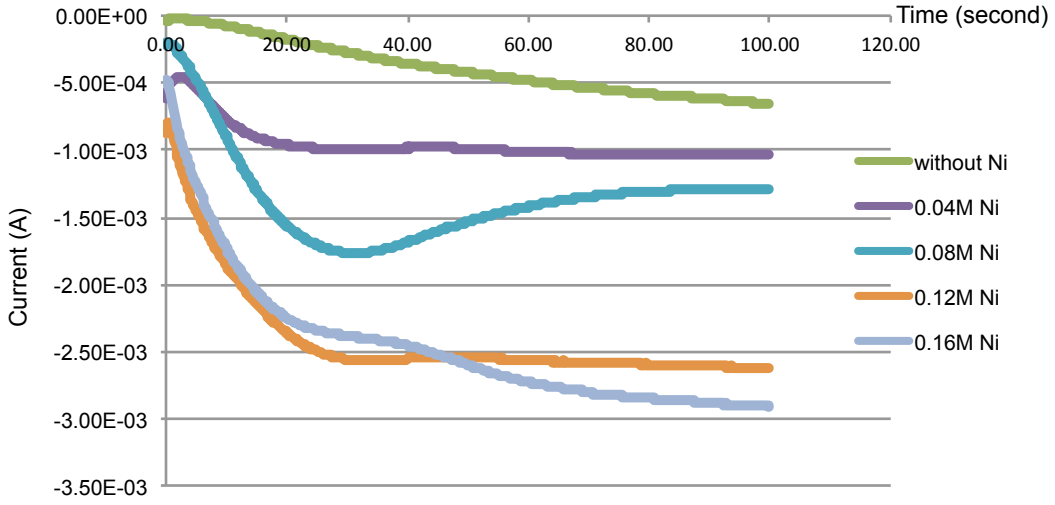

Figure 5.8 The relationship between a current density and the concentration of Ni metal ions

Using silver stripe pattern substrate, we can see that the number of gold nanoparticles hydrogen increases with increasing the concentration of nickel sulfamate, as shown in Figure 5.9., which indicates the increasing of the number of hydrogen nanobubbles. This result has the same trend with the effect of potential, so the size of gold nanoparticle at low concentration of nickel sulfamate will be smaller than the size of gold nanoparticles at high concentration of nickel sulfamate. For using AAO membranes to produce gold nanoparticles, as shown in Figure

5.10, increasing the concentration of nickel sulfamate indeed decreases the size of gold nanoparticles.

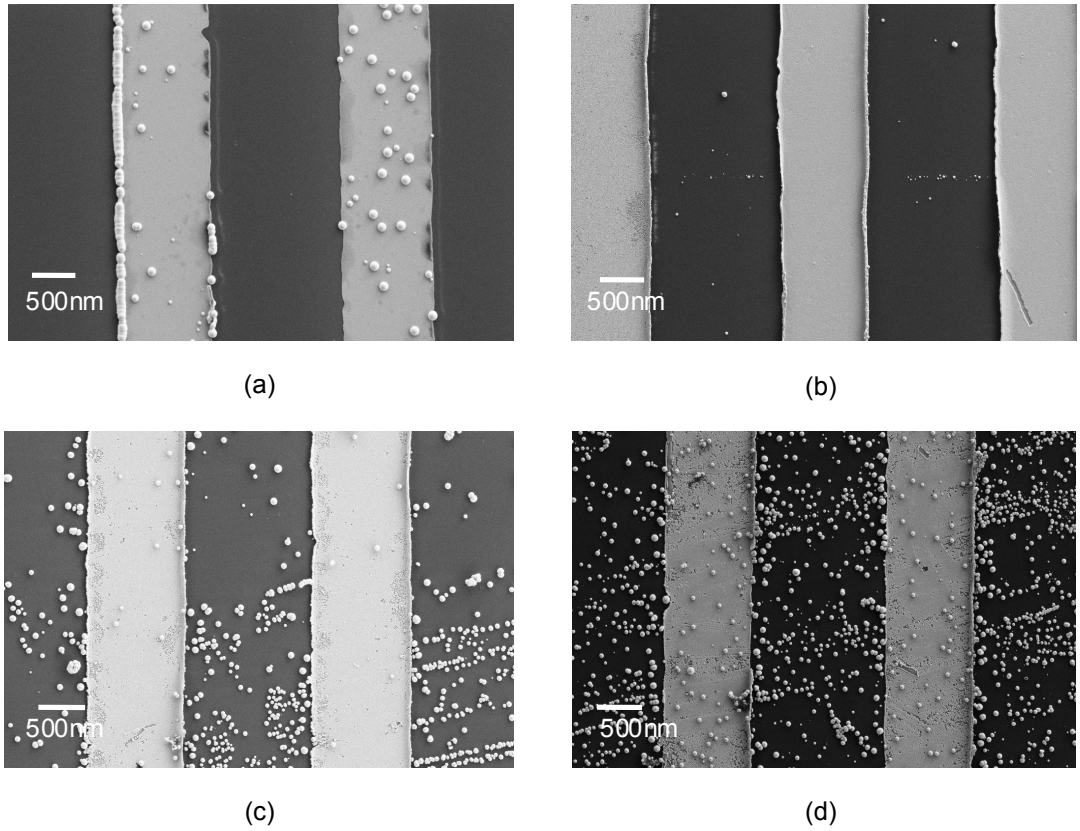

(a) (b)

(c) (d)

Figure 5.9 The effect of nickel concentration on the formation of gold nanoparticles at -0.7V for 100 sec with (a) absence of Ni^{2+} ions, (b) - (d) presence of Ni^{2+} ions with 0.2M, 0.6M, and 0.8M of Ni sulfamate solution, respectively.

Also shown in Figure 5.10, the concentration of nickel sulfamate affects to the size of gold nanoparticle in the same trend with the applied potential. At the low concentration of nickel sulfamate, the size of gold nanoparticles is larger.

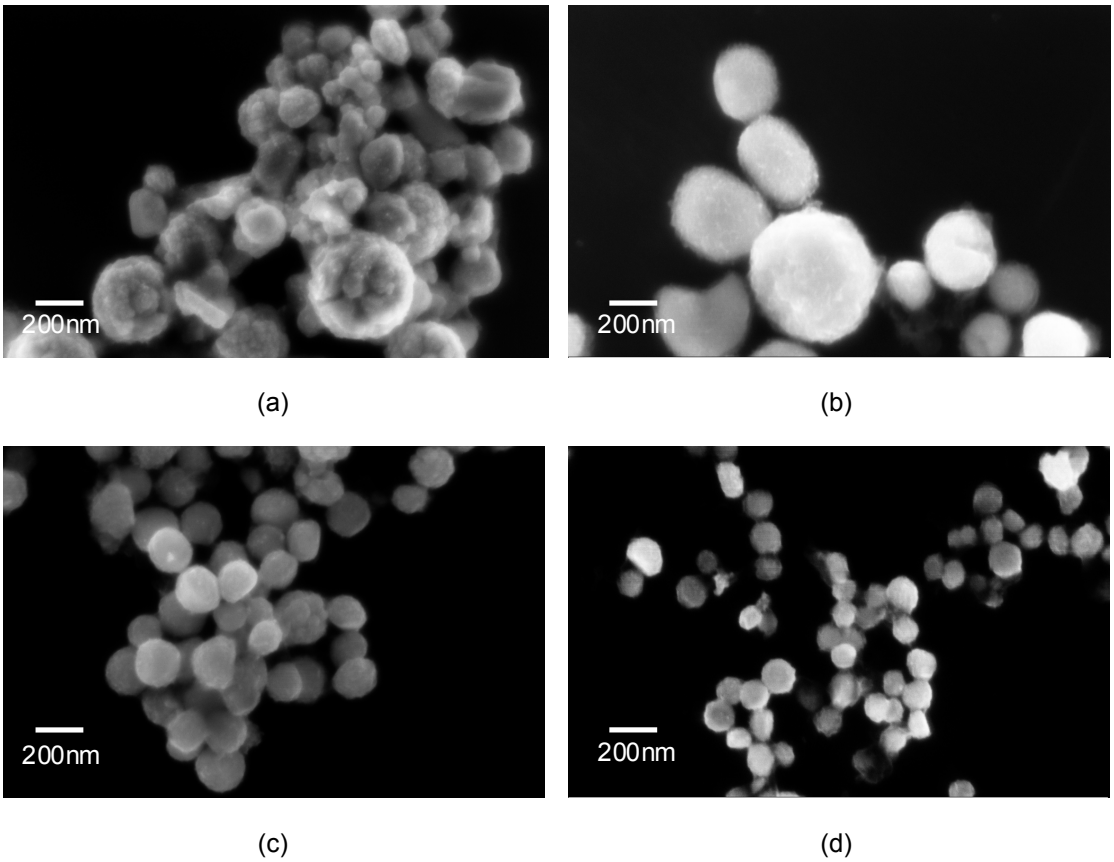

Figure 5.10 The effect of nickel concentration on the formation of gold nanoparticles at -0.7V for 800 sec with(a) absence of Ni^{2+} ions, (b) - (d) presence of Ni^{2+} ions with 0.2M, 0.6M, and 0.8M of Ni sulfamate solution, respectively.

5.3.3 Deposition Time

During the electrodeposition, hydrogen nanobubbles are being continuously generated, so number of gold nanoparticles will be increased with deposition time. Silver stripe pattern substrates were employed for studying effect of deposition time. As shown in Figure 5.11, number of gold nanoparticles that is represented number of hydrogen nanobubbles increasing with the deposition time.

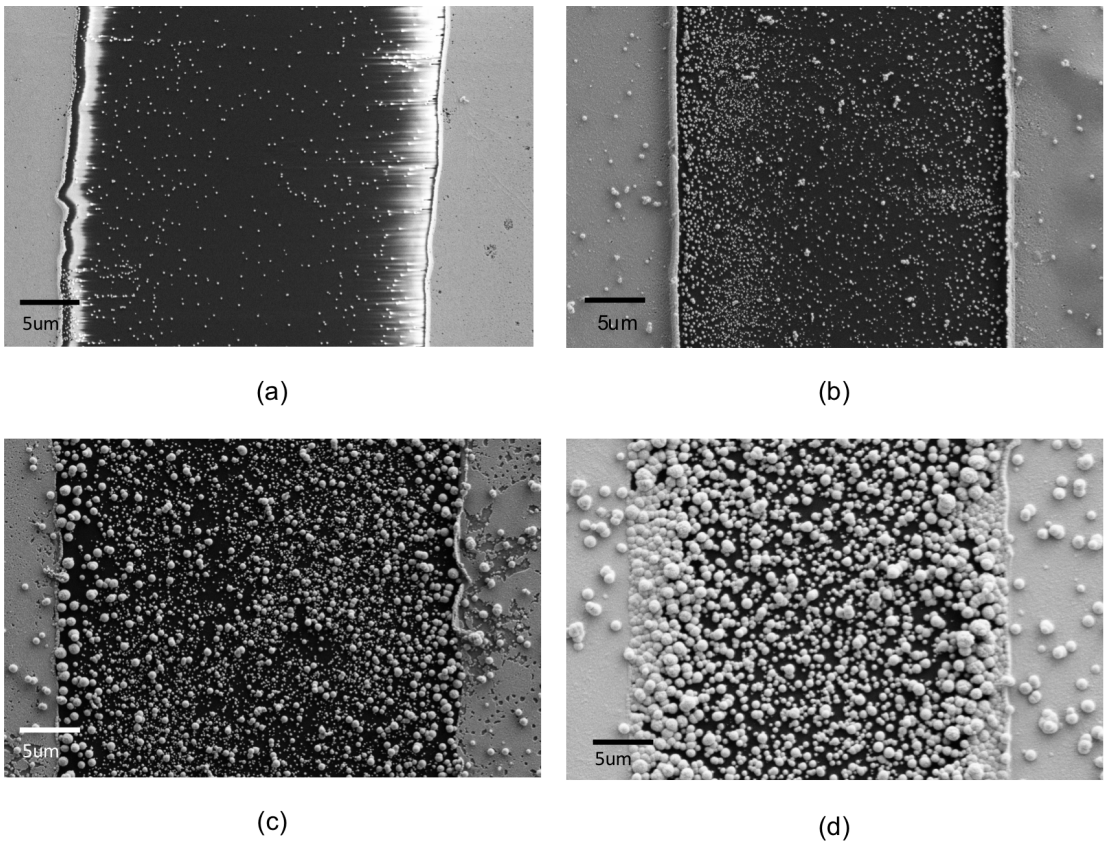

Figure 5.11 the effect of deposition time on the formation of hydrogen nanobubble at -0.7V for (a) 10 sec, (b) 100 sec, (c) 200 sec and (d) 400 sec, respectively.

5.3.4 Pore Size of AAO Template

in our previous experiments, size of gold nanoparticles that are created inside 200nm pore-diameter AAO membrane are around 150-200 nm at -0.7V. the particle size must be smaller than pore diameter, 200 nm. To study the effect of pore size on the particle size, homemade AAO membranes were used as working electrodes to synthesize hollow gold nanoparticles. Our homemade AAO membranes consist channels with 80 nm pore diameter and 15 microns length channels. Our homemade AAO membranes have well-controlled pore diameter and periodicity, narrow distribution of pore size and cylindrical pore shape, as shown in Figure 5.12 (a).

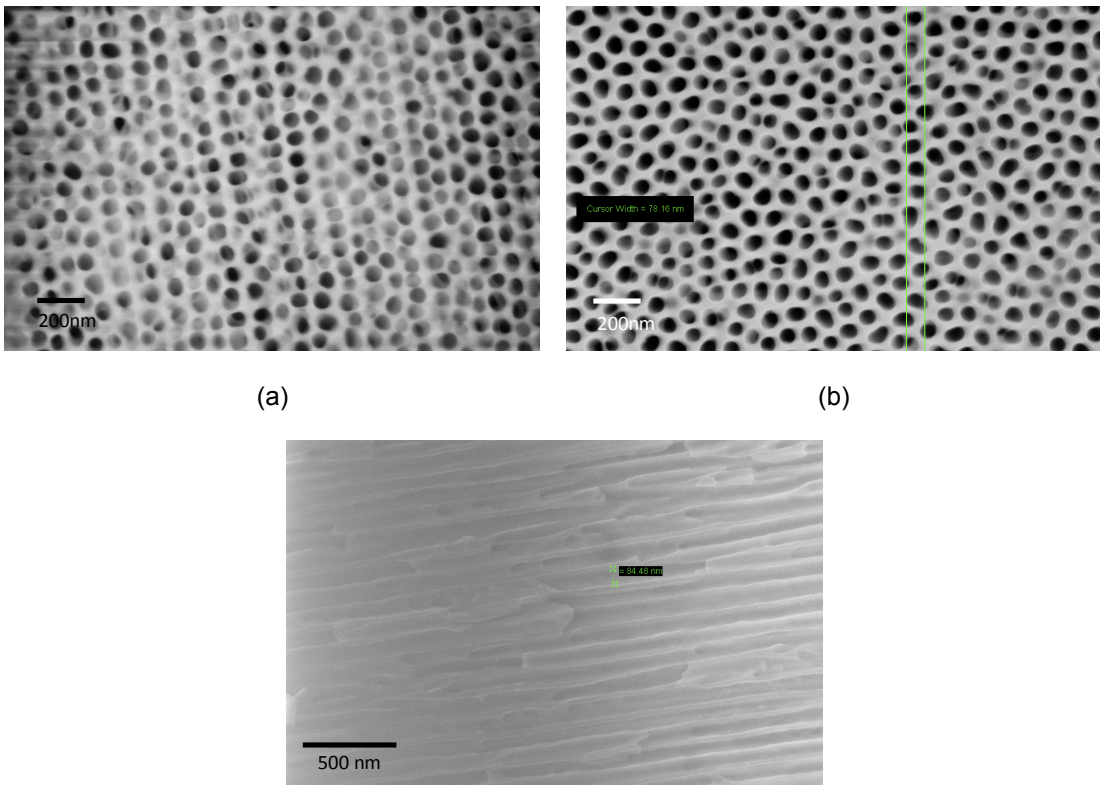

(a) (b)

(c)

Figure 5.12 SEM images of homemade AAO membrane consists of 80 nm pore diameter (a) top, (b) bottom, and (c) cross-sectioned of template.

Using homemade 80 nm AAO membranes, as shown in Figure 5.13, 50-80 nm of gold nanoparticles can be produced. From TEM image, Figure 5.13(b), one can see that core size of gold nanoparticles is around 10-20 nm, and size of gold nanoparticle is around 50-80 nm. This experiment shows that the dimension of pore size can limit size of hydrogen nanobubble, and also can limit size of hollow gold nanoparticles. It is possible the size of pore limits the volume of electrolyte, and therefore limit the available number of hydrogen cations and gold ions.

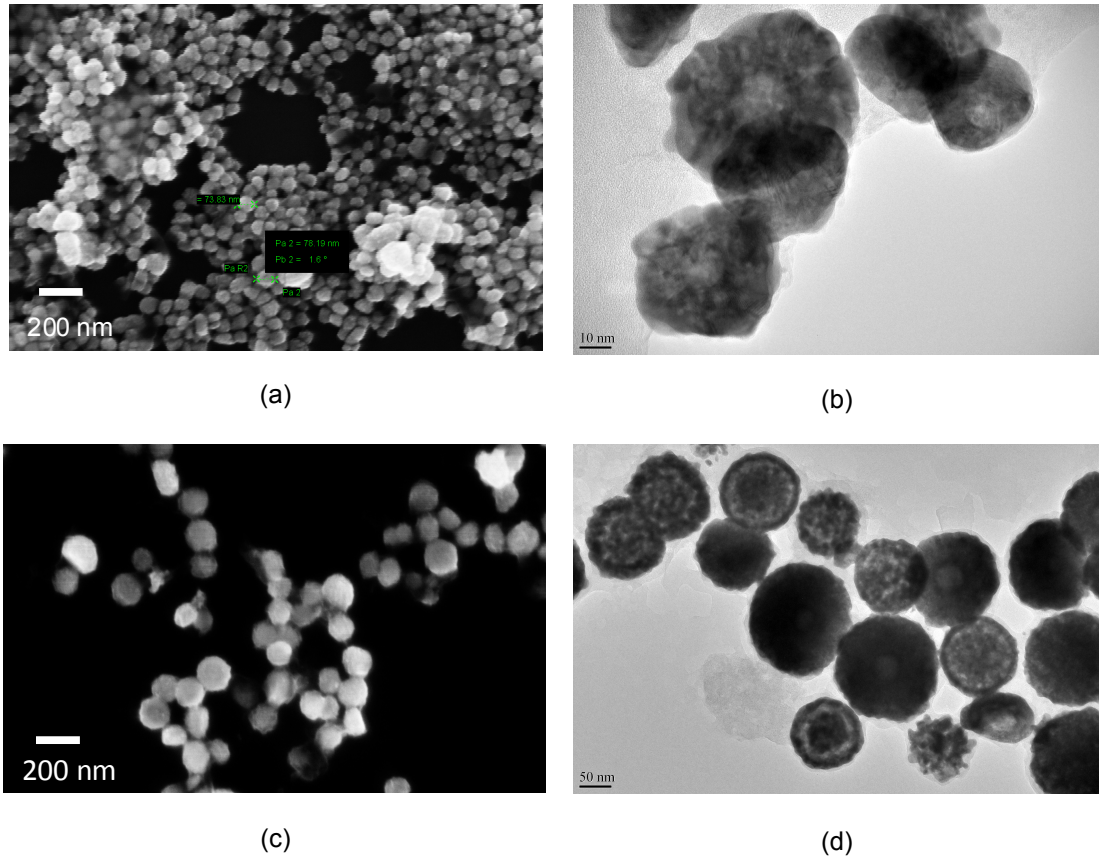

(a) (b)

(c) (d)

Figure 5.13 Gold nanoparticles (a) and (b) made by using 80 nm pore diameter AAO membrane and Gold nanoparticles (c) and (d) made by using commercial 200 nm pore diameter AAO membrane.

5.4 The Effect of Process Parameters on the Formation of Gold Shells

The synthesis parameters affecting the formation deposition of gold nanoshells include: 1) concentration of gold ions, 2) stabilizer, and 3) deposition time.

5.4.1 Gold Ion Concentration in Electrolyte

In our hypothesis, gold ions are reduced on the surface of hydrogen nanobubbles to form gold cluster. After that, the gold clusters will act as catalysts to trigger the autocatalytic disproportionation reaction to convert gold ions into gold metals. So, the concentration of gold ions plays a critical role on the growth rate of gold nanoparticles. Also as shown in Figure 5.14, the concentration of gold ions has influence on the number, size and morphology of gold

nanoparticles. When the gold concentration is low, the number of gold nanoparticles will decrease while the size of gold nanoparticles increases. It is possible that when the gold concentration is very low, free gold ions are not enough to deposit on every hydrogen nanobubbles. Therefore, only some hydrogen nanobubbles were completely covered by gold shell, so the number of nanoparticles will be small, as shown in Figure 5.14 (a). When the gold concentration is high, number of free gold ions in the channel will be high enough to deposit and cover most of newly generated hydrogen nanobubble surface. Therefore, number of nanoparticles will be increased with the concentration of gold ions, as shown in Figure 5.14 (d).

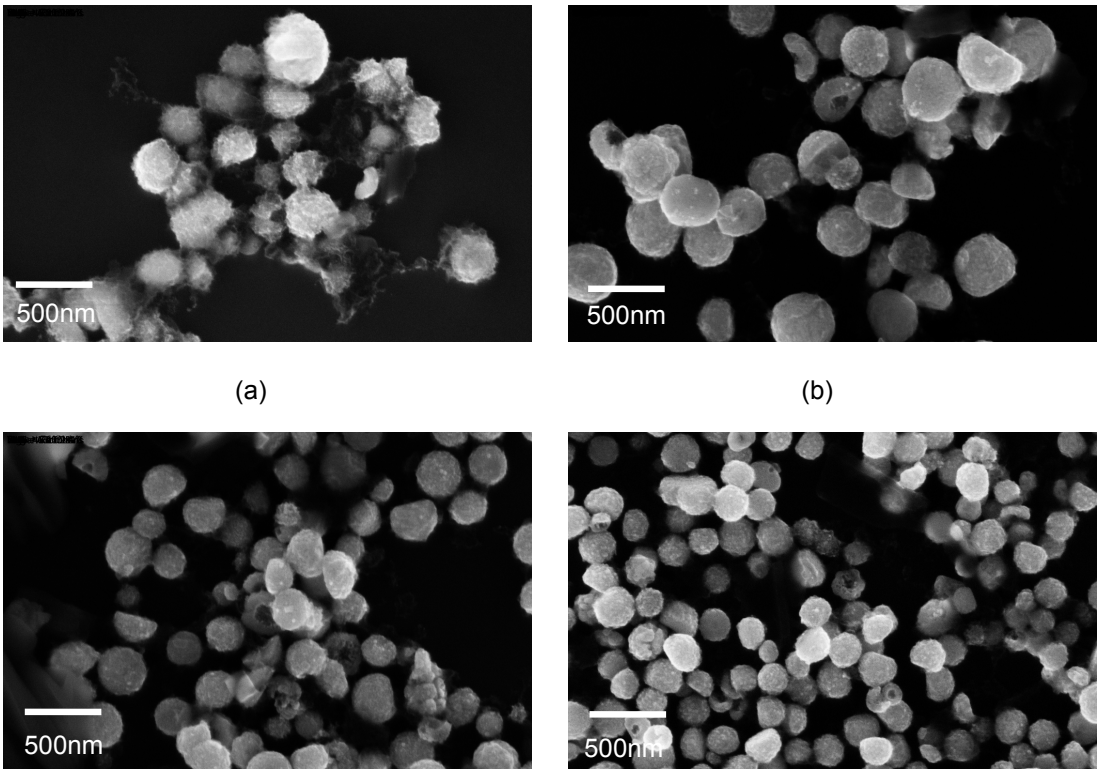

(a) (b)

(c) (d)

Figure 5.14 SEM images of hollow gold nanoparticle at the different concentration of gold (a) 1.3mM, (b) 3.9mM. (c) 6.45mM, and (d) 13mM, respectively.

The concentration of gold ions in the electrolyte also has an influence on the morphology of nanoparticles. TEM images show very rough particle surface and more porosity

of gold shell when low concentration of gold ions were used. The formation of dendrite-like structure with the low concentration of gold can be attributed to that the reaction becomes diffusion limited when the gold concentration is too low. TEM image shows a smoother particle surface and denser shell while the concentration of gold is increased, as show in Figure 5.15 (b), (c) and (d), respectively.

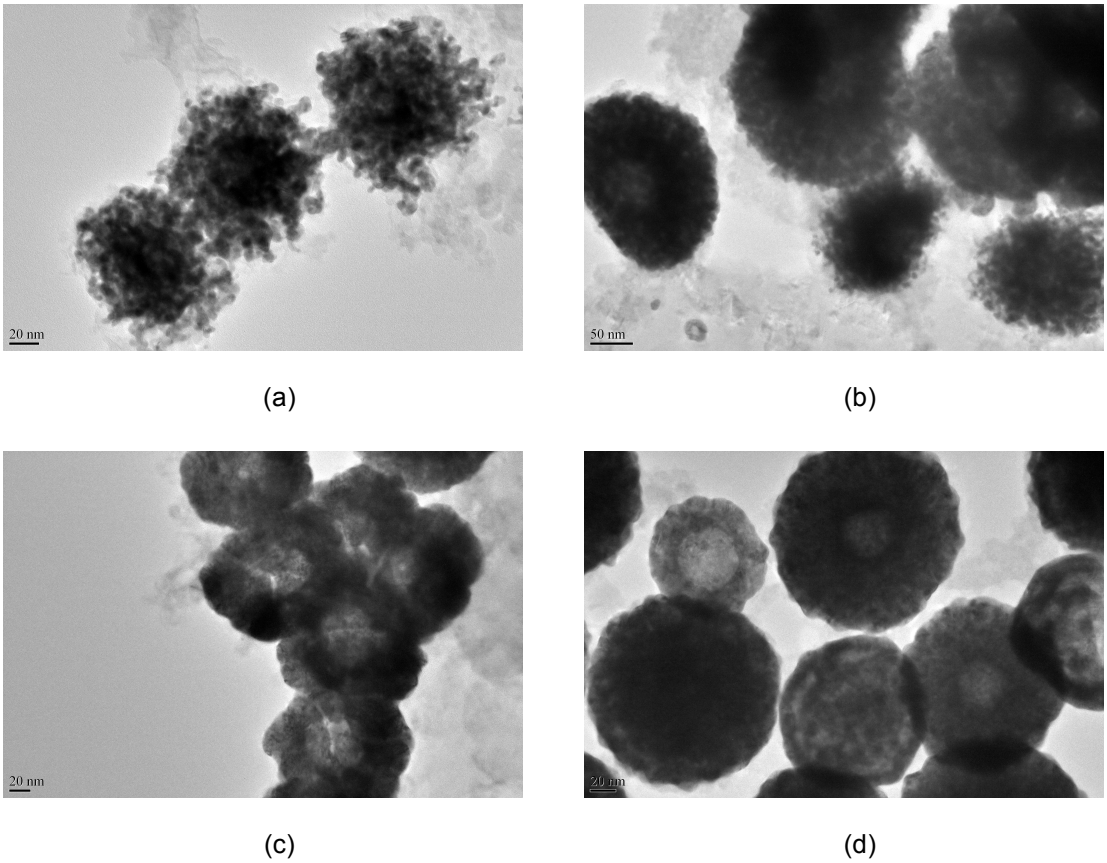

(a) (b)

(c) (d)

Figure 5.15 TEM images of hollow gold nanoparticle at the different concentration (a) 1.3mM, (b) 2.6mM, 6.45mM, and 13mM, respectively.

5.4.2 Stabilizer

It is widely known that the gold sulfite electrolyte is not stable without a stabilizer. Gold ions in solution will go through disproportionation reaction and precipitate out as gold metal. On the other hand, it should be realized that bath instability can be triggered by the introduction of

certain impurities. As a method of preventing bath decomposition resulting from the presence of ions of the transition metals, Ali and Christie added ethylenediaminetetraacetic acid (EDTA) and ethanolamine, which form highly stable complex ions with the metals and suppress their reactions with the reducing agent. The stabilizer that was used in this commercial gold(I) sulfite electrolyte is ethylenediamine (EDA). Ethylenediamine is the organic compound with the formula ($C_2H_4(NH_2)_2$), as shown in Figure 5.16. The complex of EDA can suppress the disproportionation reaction in the solution by bonding with free Au ions in the solution. (Hassan O, 1984) (A. Vaskelis, 2002)

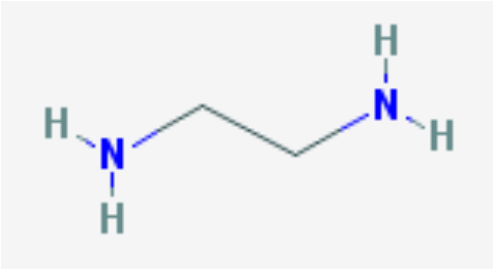

Figure 5.16 The molecular formula of ethylenediamine

We investigated the effect of EDA on the formation of gold nanoparticle by varying the concentration of EDA in electrolyte using AAO membrane. As shown in Figure 5.17, It shows that at the low concentration of EDA, the size of nanoparticles is small and the number of nanoparticles is large. When the concentration of the EDA is high, the number of particles will decrease while the size of particles will increase. Also, the surface of nanoparticles becomes very rough, as shown in Figure 5.17(c). When the concentration of the EDA is high, the number of the free gold ions decreases. So the effect of concentration of EDA is the same as the effect of gold ion concentration. (Kuveshni Govender, 2004) (Mustafa Anik, 2008) (M. Thambidurai, 2009)

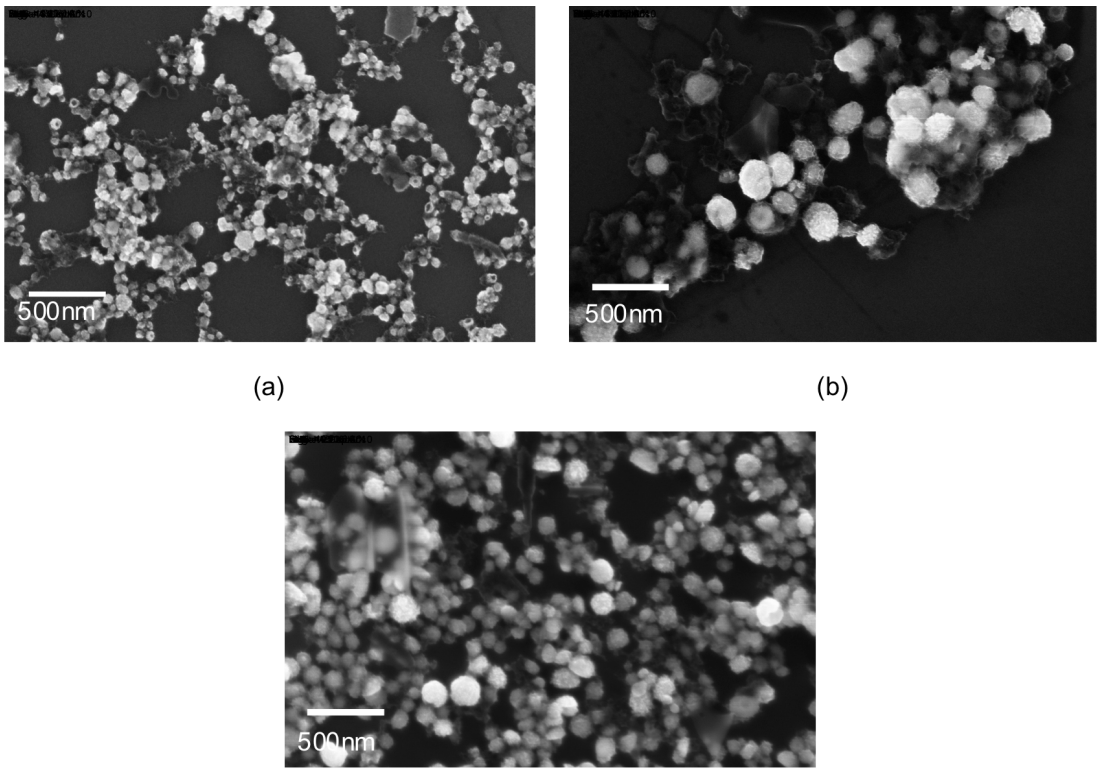

(a) (b)

(c)

Figure 5.17 Gold nanoparticles at the different concentration of EDA (a) 0.01M, (b) 0.02M and (c) 0.04M

To confirm the effect of EDA on the number of gold nanoparticles, silver stripe patterns were used. As shown in Figure 5.20, the result has the same trend with the results from AAO membrane results. Size of gold nanoparticles increases while the number of gold nanoparticles decreases with the increase of the EDA concentration. However, no gold nanoparticle can form when the EDA concentration reach to 0.1M, because the concentration of EDA is high enough to bond with all of free active gold ions inside solution, therefore, no more free active gold ions to deposit on hydrogen nanobubble surface.

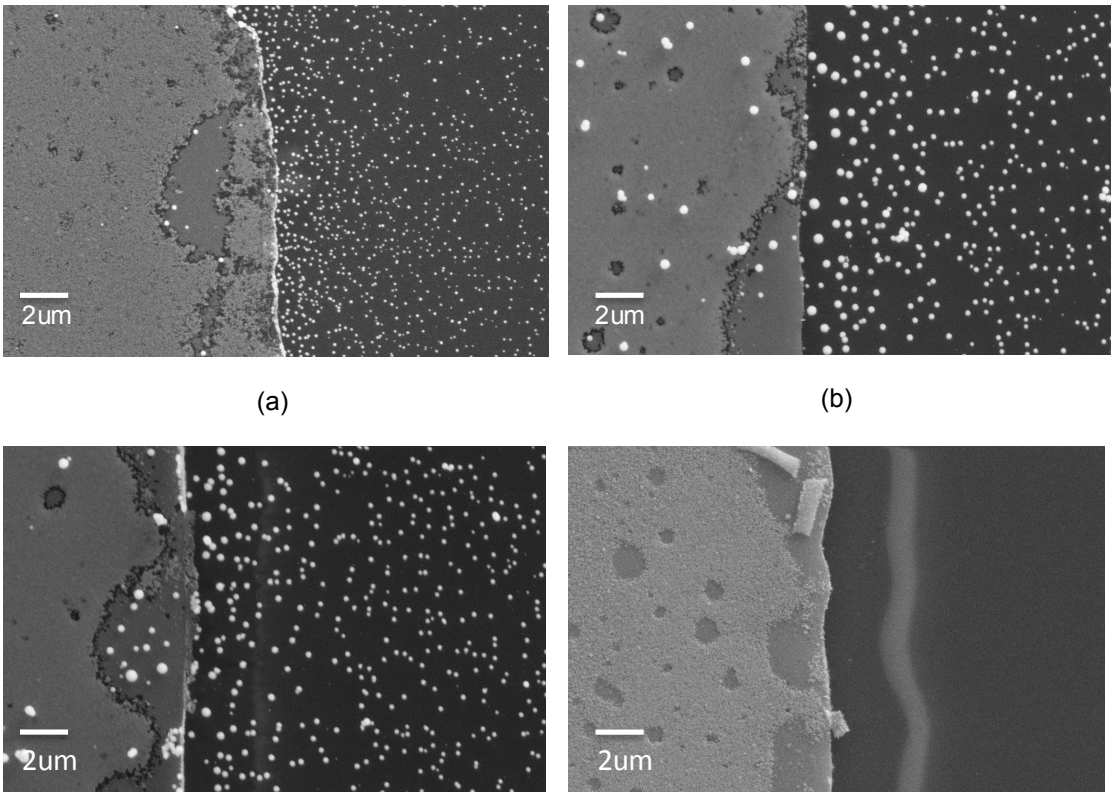

Figure 5.18 Gold nanoparticles at the different concentration of EDA (a) 0.01M, (b) 0.02M, (c) 0.05M and (d) 0.1M, respectively

5.4.3 Electroless Deposition Time

In our hypothesis, electroless plating is involved for the growth of gold nanoparticles. Unlike electroplating, in electroless plating process it is not necessary to pass an electric current through the solution to deposit gold. The thickness of gold shell should continue to increase although eelectroless reaction. AAO membranes were used to study the effect of deposition time on the particle size. The overpotential was applied to AAO working electrode for 400 sec and 800 sec, respectively.

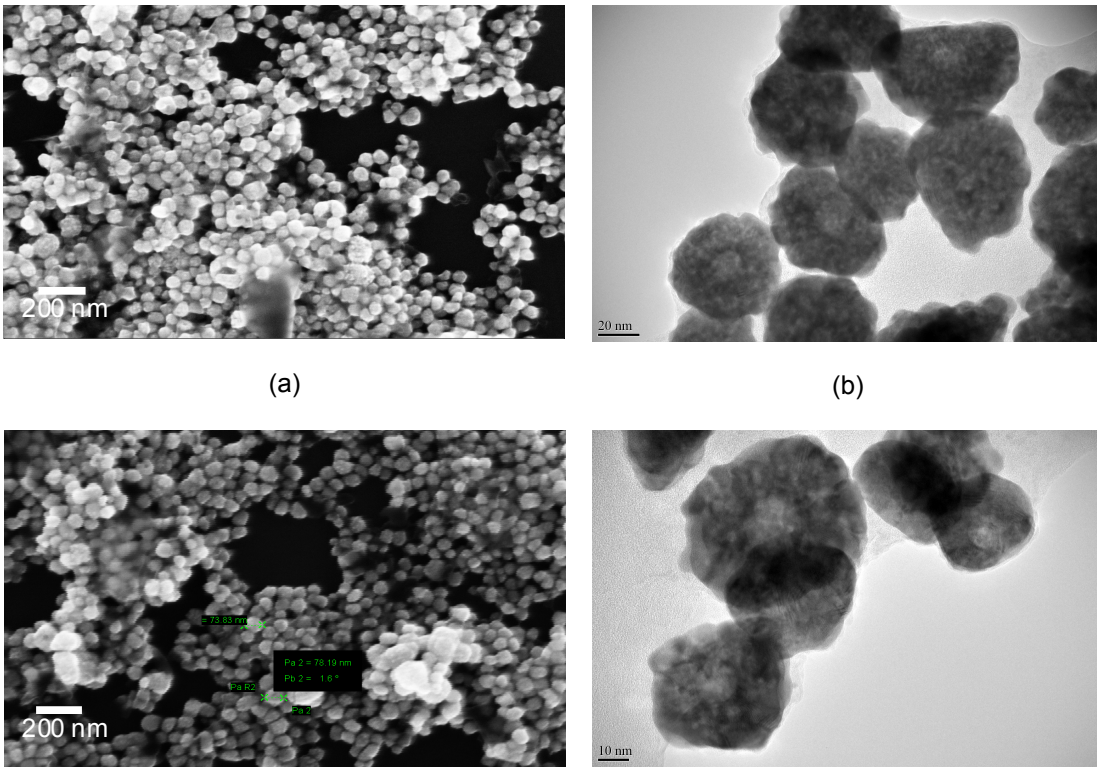

Figure 5.19 The size of particle and thickness of gold shell inside 80 nm diameter AAO membrane that (a) and (b) were created at 400 sec and (c) and (d) at 800 sec.

As shown in Figure 5.19, the size of gold nanoparticle does not significantly increase with the deposition time while the number of gold nanoparticle increase. Considering, hydrogen nanobubbles are continuously being generated during the electrodeposition, so gold ions can be reduced on other hydrogen nanobubble surface, instead of electroless deposition. Silver stripe pattern substrates were used to study the effect of electroless deposition time by changing the soaking time. The overpotential was first, applied to silver stripe pattern for certain time (100 sec). Then, patterns were left inside the solution without applying the potential for different time. Size of gold nanoparticle at different soaking time were investigated using SEM, As shown in Figure 5.20, the size of gold nanoparticle is increased with soaking time. However, the growth rate is very slow, so electroless may not be the main reason of the growth of gold

nanoshells. According to SPI results, the reduction of gold atom on hydrogen nanobubble is very fast, so the formation of gold nanoshell may be due to the hydrogen reduction mechanism, not the electroless deposition

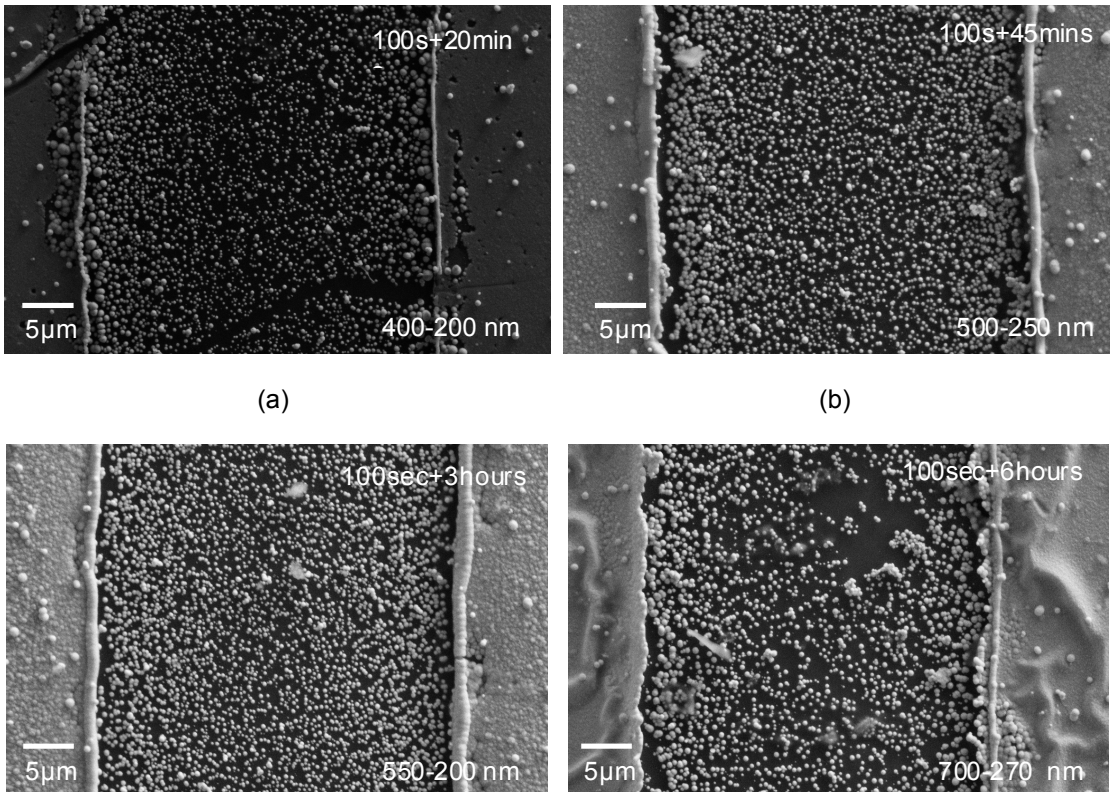

Figure 5.20 The size of gold nanoparticles on silver stripe pattern samples are increased with increasing the soaking time (a) 20 min., (b) 45 min., (c) 3 hours, and (d) 6 hours, respectively.

CHAPTER 6

USING PHASE SENSITIVE INTERFEROMETRY TO STUDY UNDERPOTENTIAL DEPOSITION OF COPPER MONOLAYER ON GOLD SUBSTRATE

The bubble template synthesis process is an electrochemical process. It is the first time that a phase sensitive interferometer (PSI) has been used to in-situ monitor an electrochemical process. The sensitivity of PSI is in the range of 100 pico nanometers. To further explore the potential of using PSI for monitoring electrochemical processes. We tested PSI for a well-established electrochemical process underpotential deposition (UPD) of Cu on Au surface.

Underpotential deposition (UPD) is the electrochemical deposition process of a submonolayer or monolayer of one metal on foreign substrate surfaces using a potential that is positive with respect to the potential for bulk deposition. It occurs when the adsorbate adatoms are more strongly bound to the foreign substrate than to a substrate of their own kind. This phenomenon has been know since the early years of this century, (Jun Zhang, 1996) (L.B. Rogers, 1949) (T. Mills, 1953) (Rogers, 1959) but its study has intensified only during the last two decades. (Kolb D' M', 1978) (Kolb D')

The early stages of adsorption/desorption along with the growth mechanism can control the structure and properties of the deposited layer. Metal adatoms and other adsorbates at submonolayer coverage are believed to have electronic properties that can deviate significantly from those of the bulk material itself. Such variations in electronic properties have been studied extensively in their application to catalytic systems.

Cyclic Voltammetry (CV) curve for UPD on single-crystal surfaces frequently display sharp current peaks. (J.W. Schultze, 1976) (D. Dickertmann, 1976) The shapes, positions, and number of these peaks depend on the substrate and the crystal plane on which the adsorption takes place, (J.W. Schultze, 1976) (D. Dickertmann, 1976) (O. M. Magnussen, 1991) as well as on the nature of the electrolyte. It was already suggested that the CV current peaks separate

ordered and disorder adsorbate structures, and it was later pointed out that the peaks themselves should correspond to phase transitions in the adsorbed layer. (Zhang, 1996)

In the past few years, the UPD of Cu on Au (111) in sulfate-containing electrolytes has been investigated by electrochemical methods using cyclicvoltammetry (CV), rotating ring disk electrode measurements, chronocoulometry, chronoamperommetry and quartz crystal microbalance (QCM). Many characterization techniques have been employed to observe the formation of underpotential deposition under active electrochemical control. It includes in-situ techniques including spectroscopic techniques such as Fourier-transform infrared spectroscopy (FTIR) Raman and second harmonic generation (SHG). The development of in situ structural techniques based on either X-ray based methods such as surface extended X-ray absorption spectroscopy (SEXAFS), X-ray absorption near edge structure (XANES) and in-situ X-ray surface diffraction (M. Cappadonia, 1997) or scanned probe microscopies like scanning tunneling microscopy (STM) (Ullmann, 1997), (Itaya, 1995), atomic force microscopy (AFM). (Katsuhiko Ogakit, 1995) (H. Bludau K' W', 1998) However, all these in-situ structural techniques require special electrochemical cells and often have an interference with the electrochemical process. (Evans D. Chabala. Bashir H. Harji, 1992)

Ex-situ techniques like Auger electron spectroscopy (AES), X-ray standing waves (XSW), Low-energy electron diffraction (LEED) (H. Bludau K. M., 1998), Reflection high energy electron diffraction (RHEED) and Auger electron spectroscopy (AES) (Enrique Herrero, 2001) that also have the ability to examine surfaces and surface structure at unprecedented levels of detail have been employed to investigate the monolayer structures.

All of these studies have provided a detailed knowledge, although still not complete, of these systems, especially for Cu UPD on Au (111) electrodes in sulfuric acid media. UPD provides a means of controlling the microscopic surface structure through the electrolyte composition and the applied potential. The fundamental understanding of UPD has a technological importance. The observation of metallic submonolayers has the ability of

significantly modify the catalytic activity of a substrate, and it is the first step in the liquid phase epitaxial growth of metallic heterostructures.

Phase sensitive interferometry can be a new alternative method for in situ monitoring the underpotential deposition of copper. PSI may not inform the information of surface structure but it will inform the deposition mechanism and kinetics. This experiment is not only the first time that optical measurement was employed to monitor a monolayer deposition but also pave a way for observing the deposition of multilayer of various monolayer metal.

6.1 Underpotential Deposition of Copper Monolayer on Gold Substrate in Sulfuric Acid Media

One of the most widely studied system is Cu UPD on Au(111). It is also a key example for studying the effects of anions and surface structure on UPD behavior as well as on surface electrochemistry. However, Cu UPD also has already been studied on polycrystalline and different single crystal surfaces including low index (such as Au(110) and Au(100)) and high index (such as Au(332), Au(775) and Au(554) surfaces (Akiyoshi Kuzume, 2004)

The effect of the deposit at underpotential conditions is more conveniently demonstrated with cyclic voltammetry experiments, where the current observed is due to the electrochemical reaction taking places as the potential is continuously changed. The application of an electrode potential (E) more positive than E_{eq}, brings about the dissolution of the metal. The metal ion will be reduced over the surface of the electrode, until a new equilibrium is reached. The formation (dissolution) of the first monolayer is easily to detected because pronounced current peaks at $E>E_{eq}$ become clearly apparent during the cathodic (anodic) potential scan, whereas the massive deposit (overpotential deposition OPD) or multilayers take place only when $E<E_{eq}$

As mentioned before, cyclic Voltammetry (CV) deposition process provides current-potential data for UPD on single-crystal surfaces frequently display sharp current peaks. (J.W. Schultze, 1976) (D. Dickertmann, 1976) The shapes, positions, and number of these peaks depend on the substrate and the crystal plane on which the adsorption takes place, (J.W.

Schultze, 1976) (D. Dickertmann, 1976) (O. M. Magnussen, 1991) as well as on the nature of the electrolyte. Electrolyte compositions used in several CV experiments are listed in Table 1 with potential scan rates and observed current-peak separations. The observation of the different electrolyte compositions in Table 1 do not qualitatively change the shape of the voltammogram indicates that within this range of compositions the adsorbates remain the same. The diagram shows that a limited amount of lead is deposited at potentials that are more positive than the Nernst potential. The reason for this is an adsorption of the metal ions on the substrate metal. The fact that the first layer forms at much more positive potentials than those necessary for the massive deposit, simply means that the metal ad-atoms develop a stronger interaction, basically dependent on the energetics of the particular system, with the nearby substrate of a different nature than their own, on which they will be bonded, than to a substrate of its own type. Electrolyte compositions used in several CV experiments are listed in Table 1 with potential scan rates and observed current-peak separations. The observation of the different electrolyte compositions in Table 1 not changing the shape of the voltammogram indicates that within this range of compositions the adsorbates remain the same.

TABLE 6.1. Representative experimental conditions employed in voltammetric studies. The peak separations are calculated as averages over positive- and negative-going potential scans.

Electrolyte	Peak separation	Scan rate
1 mM $CuSO_4$+0.1 mM H_2SO_4	100 mV	2 mV/s
1 mM $CuSO_4$+50 mM H_2SO_4	160 mV	1 mV/s
1 M $HClO_4$+1 mM Cu^{2+} +1 mM SO_4^{2-}	130 mV	20 mV/s
1 mM $Cu(ClO_4)_2$+5 mM K_2SO_4 +0.1 M $HClO_4$	140 mV	5 mV/s
5 mM $CuSO_4$+90 mM H_2SO_4	150 mV	5 mV/s

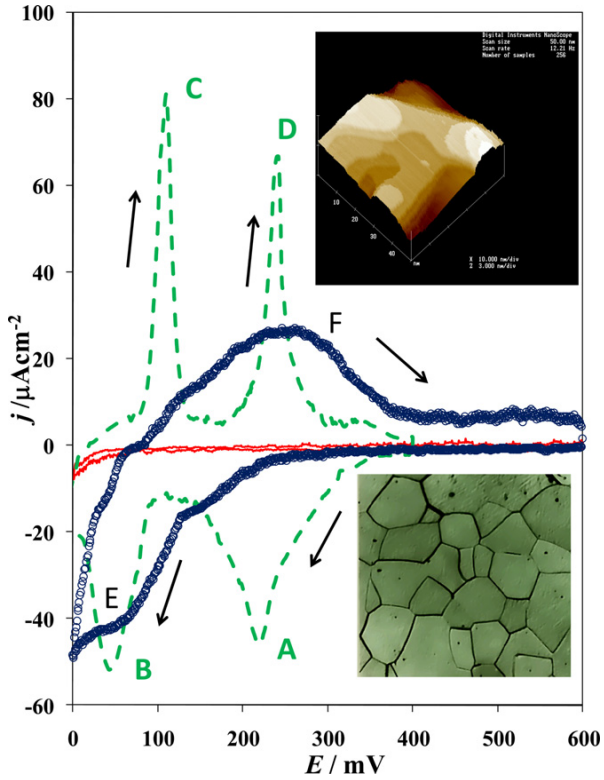

Figure 6.1 Typical cyclic voltammogram obtained for the system Au/1mM $CuSO_4$+0.1M H_2SO_4 with two different electrodes: single crystal (green) and polycrystalline (blue). The trace running almost flatly parallel to zero current (red) corresponds to the response obtained in the same system in the absence of the Cu(II) ions (blank). In all cases, the potential scan started at 800mV vs Cu^{2+}/Cu in the negative direction, as indicated by the arrows, at 15mVs^{-1} potential scan rate. Insets show the STM 40 nm x 40 nm x 10 nm, (up) and micrographic, 70x, (down) images corresponding to the electrode surface of the Au (111) and polycrystalline gold, respectively.

Figure 6.1 shows the cyclic voltammetry study performed in the system: 1.0mM $CuSO_4$, 0.1M H_2SO_4 at pH 1.0, with two different gold electrodes: Au(111) single crystal and polycrystalline Au. For both cases, it can be observed that copper deposition has taken place at potentials more positive than the equilibrium potential for the $Cu(H_2O)_6^{2+}$/Cu pair. On the Au (111) single crystal, the formation of two voltammetric peaks, namely A and B, can be distinguished when the potential was scanned toward more negative values. The peaks indicate the presence of at least two processes energetically different which are responsible for the copper underpotential electrodeposition onto the Au (111). However, when deposition took place on the polycrystalline electrode, the fist peak (Fig.1 peak A) appeared inhibited. Instead of

two peaks A and B, there only appears one peak E, Peaks C and D and peak F correspond to the oxidation of copper adlayer previously electrodeposited onto Au(111) and polycrystalline, respectively. From Figure 6.1 it is possible to see that reversing the potential scan toward more positive values, two peaks C and D become noticeable for the single crystal electrode, while just one peak F appeared for the polycrystalline. These peaks are associated with the dissolution of the copper deposited during the direct scan.

Kolb showed the structural change that the UPD copper deposit undergoes on Au(111) electrode, and the scheme of the structure attained by the deposit. It can be observed that for a lower degree of coverage, at a potential more than for peak A on the cyclic voltammetry plot referred above, the adsorption of copper atoms seems random; for intermediate coverage, that is at a potential between peaks A and B, the adsorption observed appeared ordered adopting a structure $(\sqrt{3}\times\sqrt{3})\,R30^0$ (honeycomb shape). Lastly, for more negative potentials as compared to peak B, a (1 x 1) structure indicateds the formation of the complete monolayer (ML), it is also important to mention that Wieckowski et al, from a computational and theoretical lattice-gas modeling approach and electrochemical and UHV experiments, clarify the situation about the structure of copper UPD on Au (111). They found that in the potential region between the two sharp CV peaks, the electrode is covered by a mixed adlayer of $(\sqrt{3}\times\sqrt{3})\,R30^0$ symmetry, consisting of 2/3 ML Cu and 1/3 ML sulfate. This ordered-phase region is limited on the positive-potential side by a first-order phase transition to a disordered low-coverage phase, followed at still higher potentials by transitions to pure sulfate phases. On the negative-potential side the mixed phase terminates at a second-order phase transition to a full monolayer of Cu. Moreover, they pointed out the necessity to investigate the kinetics of the deposit's formation. (M. Palomar-Pardave, 2011)

6.2 Experimental Setup and Results

We conducted in situ optical monitoring of the UPD of Cu on a transparent gold-coated mica electrode in sulfate-containing electrolytes. Underpotential deposition of copper was conducted inside a typical three-electrode electrodeposition cell using Cyclicvoltammetry technique. Cyclicvoltammogram can provide, the current peaks and measure the total charge transferred during the adsorption/desorption processes. Mica sheets V1 (Ted Pella, Inc.) (Muscovite Mica), which is transparency material were used as substrate. Mica is a silicate (phyllosilicate) minerals that have a layered or platy texture. Muscovite, potash type mica, sometimes known as granitic mica, is the best of all micas in dielectric strength, perfection of cleavage, and transparency. It has the following chemical formula: $H_2KAI_3(SiO_4)_3$. These mica sheets were coated with 10 nm of chromium and 15 nm of gold by evaporation technique, respectively. The mica substrate was mounted concentrically with epoxy resin on the bottom of the electrochemical cell and was left for curing around 30 minutes. Electrolyte consists of 1 mM $CuSO_4$ and 0.1mM H_2SO_4 was used as electrolyte and Ag/AgCl electrode was used as reference electrode. The potential was scanned from 0.60V to 0.012V. The cyclic voltammogram shows two well defined peaks, as shown in Figure 6.2, corresponding to two different adsorption and desorption processes. This result shows that gold-coated mica substrate can be used as working electrode for studying a monolayer formation of copper using cyclicvoltammetry, and also can be used as in-situ study substrate for PSI. The peak currents for the deposition and stripping processes exhibit a marked sweep rate dependence, being proportional to the scan rate for values below 5mV/s. As shown in Figure 6.2, the current density of cyclicvoltammetry increased with the sweep rate.

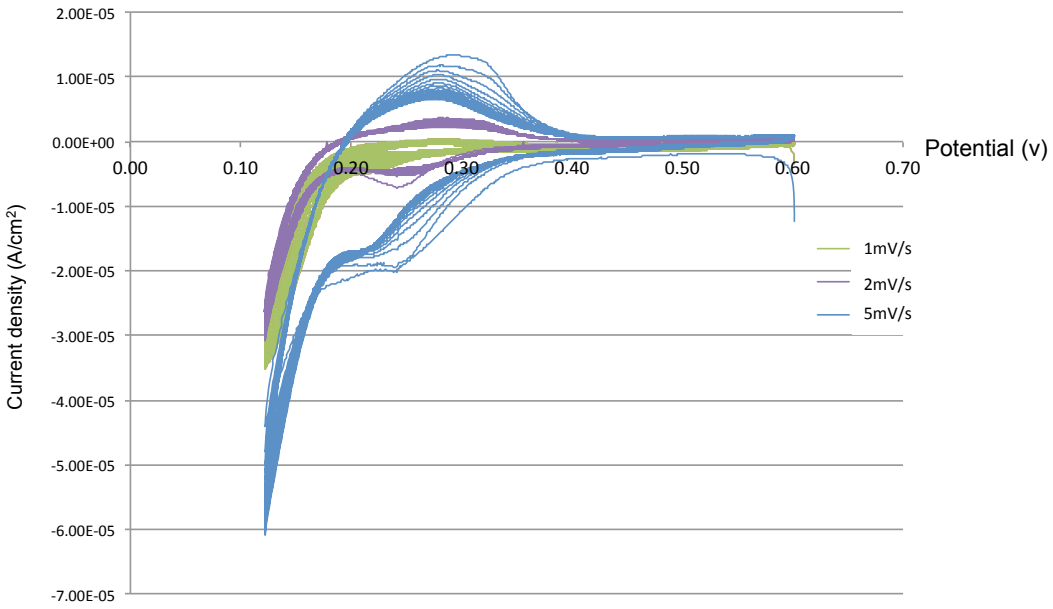

Figure 6.2. Our experimental cyclicvoltammetry current densities for a gold-coated mica electrode in 1mM $CuSO_4$ + 0.1mM H_2SO_4 at 1, 2 and 5 mV/s, respectively.

As mention before, PSI has been successfully, used for in-situ study of the formation of hydrogen nanobubble and gold shells by detecting the changing in optical path length and the depth of modulation without interrupting the deposition process, Here, underpotential deposition is a good example to test the sensitivity of PSI. As shown in Figure 6.3 (a) when a monolayer of copper form, the changing in OPL should be seen due to thickness of added layer on the substrate surface.

The light reflects from top and bottom surface of mica. The modulation pattern was recorded to be an original modulation. As a monolayer of copper deposits on substrate's surface, so the phase was shifted due to OPL. Following Equation 4.3, the phase change due to the change in the optical path length as a result of the physical increase in thickness caused by a monolayer of copper formation, that is demonstrated by the current density data of cyclicvoltammetry result, as shown in Figure 6.3 (b).

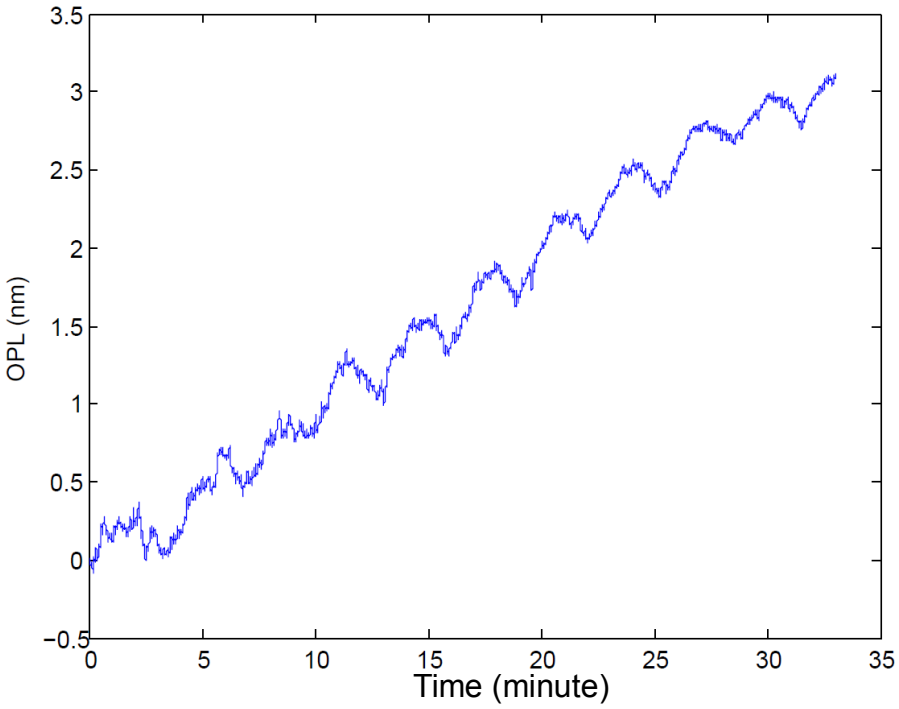

(a)

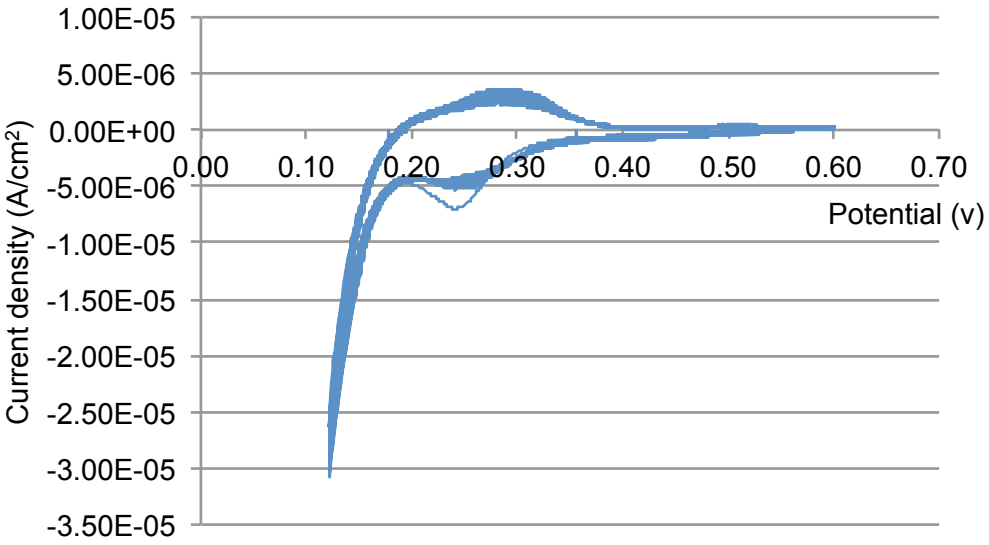

(b)

Figure 6.3 (a) the change in optical path length in (a) showing a monolayer of copper deposition on gold-coated mica substrate, which is conducted by using cyclicvoltammetry, as shown in (b).

As shown in Figure 6.3 (a), one up and down cycle in optical path length change is corresponding to one cycle with cyclicvoltammogram, clearly showing the ability of PSI to detect monolayer copper deposition and stripping.

This experiment is not only the demonstration of a new characterization method for in-situ studying the formation of one monolayer of copper during the adsorption/desorption, but also shows the ultra high sensitivity, being able to detect a monolayer of atom of PSI.

CHAPTER 7

CONCLUSIONS

In this study, the results show that the electrochemically evolved hydrogen bubbles can serve as templates and reducing agents for the synthesis of hollow gold nanoparticles. To understanding such process, the silver stripe pattern substrates, which is fabricated using photolithography technique on the microscopy glass slide have been used for studying the formation mechanism of hollow gold nanoparticles both in-situ and ex-situ study.

The formation mechanism of hollow gold nanoparticles can be described in a three stages process. (1) Hydrogen nanobubbles were generated electrochemically by supersaturation mechanism, (2) gold complex cations were reduced to become metallic gold clusters at the boundary of hydrogen nanobubbles, (3) metallic gold clusters act as autocatalysts to trigger the gold cations to go through disproportionation reaction.

Phase Sensitive Interferometry (PSI) have been used for real-time observation of the formation mechanism of hollow gold nanoparticles. The formation of hydrogen nanobubbles and gold shells can be detected by the phase shift and amplitude change that is due to the change of optical path length and reflectivity during the synthesis process. This study demonstrates that PSI can become a new method for in-situ study of an electrochemical process without any interference with the process. We also demonstrated that PSI can be used for real-time monitoring the underpotential deposition and stripping of monolayer of copper on gold substrate.

Ex-situ study to understand the effect of electrochemical conditions for tuning the size

and also improving the size distribution of hollow gold nanoparticles has been conducted. Anodic Aluminum Oxide membranes (AAO) were used as a working electrode to capture the electrochemically evolved hydrogen nanobubbles and subsequently to collect hollow gold nanoparticles inside the membranes. Size and number of hollow gold nanoparticles can be tuned by varying electrochemical conditions. Using either high overpotential or high concentration of nickel ions increases the number of hollow gold nanoparticles while reduces the size of gold nanoparticles. With longer deposition time, the number of hollow gold nanoparticle increases but the size of gold nanoparticles does not increase. The additive of EDA and the concentration of gold in electrolyte are two key parameters for controlling the size and number and morphology of hollow gold nanaoparticles. The low concentration of gold ion or the high concentration of EDA cause small number but large size of hollow gold nanoparticles, also cause a high porosity of gold shell. In addition, the size of gold nanoparticles can be controlled by using AAO with the different size of channels. Using AAO with smaller size channels can produce smaller particles.

Furthermore, SPI can be used for real-time monitoring the underpotential deposition of copper on gold substrate. A monolayer of copper can deposit on gold substrate and be oxidized by CyclicVoltammetry technique. This experiment was conducted using a gold-coated mica substrate. Mica substrates were deposited by 75 nm of chromium and 150 nm of gold, respectively. A monolayer of copper can be detected by phase shift due to the changing of OPL during electrodeposition. This is not only the first time that PSI technique is used for in-situ study the formation mechanism of hydrogen nanobubble and the reduction of gold shell but it is also the first time that PSI technique is used for real-time observe the deposition of monolayer of copper.

From our results, we invented a hydrogen nanobubble template synthesis method that is the new method for creating a tunable hollow gold nanoparticles. This is a one-step synthesis

technique and well-controlled process. Moreover, PSI is employed for in-situ study the formation of hollow gold nanoparticle and a monolayer of copper. This is the good feasible for using PSI technique to real time monitor other electrochemical processes.

REFERENCES

1. A. Vaskelis, E. N. (2002). Kinetics of electroless copper deposition using cobale(II)-ethylenediamine complex compounds as reducing agents. *Journal of Applied Electrochemistry , 32*, 297-303.
2. Adam M. Schwartzberg, T. Y. (2006). Synthesis, Characterization, and Tunable Optical Properties of Hollow Gold Nanospheres. *J. Phys. Chem. B , 110*, 19935-19944.
3. Agrawal A, H. S. (2006). Quantitative evaluation of optical coherence tomography signal enhancement with gold nanoshells. *J Biomed Opt , 11:041121*.
4. Akiyoshi Kuzume, E. H. (2004). Copper underpotential depositio at high index single crystal surfaces of Au. *Joutnal of Electroanalytical Chemistry , 570*, 157-161.
5. Amanda J. Haes, R. P. (2002). A nanoscale optical biosensor: Sensitivity and selectivity of an approach based on the localized surface plasmon resonance spectroscopy of triangular silver nanoparticles. *Journal of the American Chemical Society , 124* (35), 10596-10604.
6. Astruc, M.-C. D. (2004). Gold Nanoparticles: Assembly, Supramolecular Chemistry, Quantum-Size-Related Properties, and Applications toward Biology, Catalysis and Nanotechnology. *Chem, Rev , 104*, 293-346.
7. Bikram M, G. A. (2007). Temperature-sensitive hydrogels with SiO2-Au nanoshells for controlled drug delivery. *J Control Release , 123*, 219-227.
8. Boyd, N. (2011, May 19). *Center of Biomolecular Science and Engineering.* Retrieved from https://cbse.soe.ucsc.edu/news/article/1837?ID=1837
9. Boyd, N. (2011). *QB3 Fellowship Furthers Research on Hollow Gold Nanospheres for Cancer Treatment.* University of California Santa Cruz, Center for Biomolecular Science and Engineering.
10. Bradley Deutsch, R. B. (n.d.). Retrieved from Optics&Photonics: http://www.osa-opn.org/home/articles/volume_21/issue_12/features/interferometric_imaging/detecting_nanoparticles_with_phase-sensitive_inter/
11. C.Z. Wu, Y. X. (2006). Synthesis of New-Phased VOOH Hollow “Dandelions” and Their Application in Lithium-Ion Batteries. *18* (131727-1732).
12. Chienwen Huang, J. J. (2010). Trapping Iron Oxide into Hollow Gold Nanoparticles. *Nanoscale Research Letters , 6* (43).
13. Chienwen Huang, Y. W. (2010). Porous Hollow Gold Nanoparticles for Cancer SERS Imaging. *Journal of Nano Research , 10*, 137-148.
14. Chithrani BD, G. A. (2006). Determining the size and shape dependence of gold nanoparticle uptake into mammalian cells. *Nano Lett , 6*, 662-668.
15. Christina Graf, D. L. (2003). A General Method To Coat Colloidal Particles with Silica. *Langmuir , 19* (17), 6693-9700.
16. Christopher Loo, A. L. (2005). Immunotargeted Nanoshells for Integrated Cancer Imaging and Therapy. *Nano Letters , 5* (4), 709-711.
17. Debenedetti, V. K. (2003). A kinetic theory of homogeneous bubble nucleation. *Journal of Chemical Physics , 118* (2), 768-783.
18. Enrique Herrero, L. J. (2001). Underpotential Deposition at Single Crystal Surfaces of Au, Pt, Ag and other Materials. *Chem.Rev. , 101*, 1897-1930.
19. Feldmann, D. H. (2007). Nanoscale γ-AlO(OH) Hollow Spheres: Synthesis and Container-Type Functionality. *Nano Lett., , 7* (11), 3489-3492.
20. Frank Caruso, M. S. (2001). Magnetic Nanocomposite Particles and Hollow Spheres Constructed by a Sequential Layering Approach. *Chem. Mater. , 13* (1), 109-116.
21. Frank Caruso, R. A. (1998). Nanoengineering of Inorganic and Hybrid Hollow Spheres by Colloidal Templating. *Science , 282* (5391), 1111-1114.

22. H. Bludau, K. M. (1998). The structure of the underpotential deposition of copper on to Pt(111) in the presence of chloride anions: a LEED structure analysis. *Surface Science , 402*, 786-789.
23. H. Riegel, J. M. (1998). Role of mass transfer on hydrogen evolution in aqueous media. *Journal of Applied Electrochemistry , 27*, 10-17.
24. Han-Pu Liang, H.-M. Z.-S.-G.-J.-L. (2004). Pt Hollow Nanospheres: Facile Synthesis and Enhanced Electrocatalysts. *Angew.Chem.Inter.Ed. , 43*, 1540-1543.
25. Haolan Xu, W. W. (2007). Template Synthesis of Multishelled Cu2O Hollow Spheres with a Single-Crystalline Shell Wall. *Angewandte Chemie International Edition , 46* (9), 1489-1492.
26. Hassan O, A. a. (1984). A Review of Electroless Gold Deposition Processes. *Gold Bull , 17* (4), 118-127.
27. Hong Jin Fan, U. G. (2007). Formation of Nanotuves and Hollow Nanoparticles Based on Kirkendall and Diffusion Processes: A Review. *small , 3* (10), 1660-1671.
28. Huang X, J. P.-S. (2006b). Determination of the minimum temperature required for selective photothermal destruction of cancer cells with the use of immunotargeted gold nanoparticles. *Photochem Photobiol , 82*, 412-17.
29. Huang, C. (2010). *Bubble Template Synthesis of Hollow Gold Nanoparticles and Their Applications as Theranostic Agents.* Arlington, TX, USA: The University of Texas at Arlington.
30. Huang, Y. B. (2007). Thermal Behavior of Localized Surface Plasmon Resonance of Au/TiO2 core/shell nanoparticle arrays. *Applied Physics Letters , 90*, 183117.
31. Imhof, A. (2001). Preparation and Characterization of Titania-Coated Polystyrene Spheres and Hollow Titania Shells. *Langmuir , 17* (12), 3579-3585.
32. Itaya, K. O. (1995). In-Situ Scanning Tunneling Microscopy of Underpotential and Bulk Deposition of Silver on Gold (111). *Electrochemica Acta , 40* (10), 1249-1257.
33. J.Hwang, B. M. (2004). Al2O3 Nanotubes Fabricated by Wet Etching of ZnO/Al2O3 Core/Shell Nanofibers. *Adv. Mater. , 16*, 422.
34. Jain PK, H. X. (2008). Noble metals on the nanoscale: optical and photothermal properties and some applications in imaging, sensing, biology, and medicine. *41* (12), 1578-1586.
35. Jain PK, L. K.-S. (2006a). Calculated absorption and scattering properties of gold nanoparticles of different size, shape and composition: application in biological imaging and biomedicine. *J Phys Chem B , 110*, 7238-7248.
36. Jensen RA, S. J. (2007). Single nanoparticle based optical pH probe. *Appl Spectrosc , 61*, 832-838.
37. Jonathan A. Edgar, H. M. Synthesis of Hollow Gold Nanoparticles are Rings Using Silver Templates. *Nanoscience and Nanotechnology, 2008, ICONN 2008* (pp. 36-19). Melbourne, Vic: IEEE Xplore.
38. Jun Okada, J. I. (2001). Underpotential and bulk deposition of copper on Pd(111) in sulfuric acid solution studied by in-situ scanning tunneling microscopy. *Phys. Chem. Chem. Phys. , 3*, 3297-3320.
39. Katz, M. B. (1975). Bubble Nucleation in Liquids. *AIChe Journal , 21* (5), 833-848.
40. Kosich, D. (2008, Mar 24). *Mineweb*. Retrieved August 26, 2010, from Mineweb: http://www.mineweb.com
41. Kumar R, M. A. (2005). Hollow gold nanoparticles encapsulating horseradish peroxidase. *Biomaterials , 26*, 6743-53.
42. Kuveshni Govender, D. S. (2004). Understanding the factors that govern the deposition and morphology of thin films of ZnO from aqueous solution. *Journal of Materials Chemistry , 14*, 2575-2595.
43. Kwangjin An, S. G.-I. (2008). Synthesis of Uniform Hollow Oxide Nanoparticles through Nanoscale Acid Etching. *Nano Lett , 8* (12), 4552-4258.

44. Kwangjin An, T. H. (2009). Synthesis and biomedical applications of hollow nanostructures. *Nanotoday , 4*, 359-373.
45. L. R. Hirsch, R. J. (2003). Nanoshell-mediated near-infrared thermal therapy of tumors under magnetic resonance guidance. *he National Academy of Sciences of the United States of America*, *100(23)*, pp. 13549-13554 .
46. L. R. Hirsch, R. J. (2003). Nanoshell-mediated near-infrared thermal therapy of tumors under magnetic resonance guidance. *the National Academy of Sciences of the United States of America . 100.* 13549-13554: National Academy of Sciences.
47. Leon R. Hirsch, A. M. (2006). Metal Nanoshells. *Annals of Biomedical Engineering , 24* (1), 15-22.
48. LI, Y. J. (2010). Formation of Au Nanoparticles Through Reduction of Na3Au(SO3)2 by Electrochemically Evolved Hydrogen. Arlington, TX, USA: The University of Texas at Arlington.
49. Low AF, T. G. (2006). Immunonanoshells for targeted photothermal ablation of tumor cells. *Int J Nanomedicine , 1*, 149-154.
50. Lowery AR, G. A. (2006). Tumor vascular permeability and the EPR effect in macromolecular therapeutics. *J Control Release , 65*, 271-284.
51. M. Cappadonia, K. R. (1997). In-situ X-ray surface diffreaction of copper underpotential deposition on Au(100). *Journal of Electroanalytical Chemistry , 436*, 73-78.
52. M. Thambidurai, N. M. (2009). Preparation and Characterization of Nanocrystalline CdS Thin Films. *Chalcogenide Letters , 6* (4), 171-179.
53. McGraw, A. L. (1996). Thermodynamics, gas-liquid nucleation, and size-dependent surface tension. *Electrophysics Letters , 35* (5), 367-372.
54. metals, H. b. (1993). J.B. Condon and T. Schober. *Journal of Nuclear Materials , 207*, 1-24.
55. Mu Yang, J. M. (2005). General Synthetic Route toward Functional Hollow Spheres with Double-Shelled Structures. *Angewandte Chemie International Edition , 44* (41), 6727-6730.
56. Mustafa Anik, E. K. (2008). Effect of coating composition on the properties of electroldess nickel-boron films. *Surface & Coatings Technology , 202*, 1718-1727.
57. O'Neal DP, H. L. (2004). Photo-thermal tumor ablation in mic using near infrared-absorbing nanoparticles. *Cancer Lett , 209*, 171-176.
58. Oxtoby, D. W. (1998). Nucleation of First-Order Phase Transitions. *Acc. Chem. Res. , 31*, 91-97.
59. P. K. Weathersby, L. D. (1982). Homogeneous nucleation of gas bubbles in vivo. *Journal of Applied Physiology , 53* (4), 940-946.
60. Peter G. Bowers, C. H. (1995). Supersaturation Limit for Homogeneous Nucleation of Oxygen Bubbles in Water at Elevated Pressure: "Superhenry's Law". *J. Phys. Chem. , 99*, 9632-9637.
61. Prashant K. Jain, Y. X. (2009). Surface Plasmon Resonance Enhanced Magneto-Optics (SUPREMO): Faraday Rotation Enhancement in Gold-Coated Iron Oxide Nanocrystals. *NanoLetters , 9* (4), 1644-1650.
62. Qiao Zhang, J. G. (2010). Tailored Synthesis of Superparamagnetic Gold Nanoshells with Tunable Optical Properties. *Adv. Mater. , 22*, 1905-1909.
63. Qing Peng, Y. D. (2003). ZnSe Semiconductor Hollow Microspheres. *43* (26), 3027-3030.
64. Rachel A. Caruso, A. S. (2001). Multilayered Titania, Silica, and Laponite Nanoparticle Coating on Polystyrene Colloidal Templates and Resulting Inorganic Hollow Spheres. *Chem. Mater. , 13* (2), 400-409.
65. Robert Elghanian, J. J. (1997). Selective colorimetric detection of polynucleotides based on the distance-dependent optical properties of gold nanoparticles. *Science , 277* (5329), 1078-1080.

66. S.B. Yoon, K. S. (2002). Fabrication of Carbon Capsules with Hollow Macroporous Core/Mesoporous Shell Structures. *Adv. Matter. , 14* (1), 19-21.
67. Sang-Wook Kim, M. K. (2002). Fabrication of Hollow Palladium Spheres and Their Successful Application to the Recyclable Heterogeneous Catalyst for Suzuki Coupling Reactions. *J. Am. Chem. Soc. , 124* (26), 7642-7643.
68. Sara E. Skrabalak, J. C. (2008). Gold Nanocages: Synthesis, Properties, and Applications. *Acc. Chem. Res. , 41* (12), 1587-1595.
69. *ScienceDaily.* (2008, 03 28). Retrieved from http://www.sciencedaily.com/releases/2009/03/090322154415.htm
70. Seong Su Kim, W. Z. (1998). Ultrastable Mesostructured Silica Vesicles. *Science , 282* (5392), 1302-1305.
71. Sershen SR, W. S. (2000). Temperature-sensitive polymer-nanoshell composites for photothermally modulated drug delivery. *J.Biomed Mater Res , 51*, 293-298.
72. Sonnichsen Carsten, R. B. (2005). A molecular ruler based on plasmon coupling of single gold and silver nanoparticles. *Nature biotechnology , 23* (6), 741-5.
73. stern JM, S. J. (2007). Efficacy of laser-activated gold nanoshells in ablating prostate cancer cells in vitro. *J Endourol , 21*, 939-943.
74. Stern JM, S. J. (2008). Selective prostate cancer thermal ablation with laser activated gold nanoshells. *J Urol , 179*, 748-753.
75. Tenhu, J. S. (2007). Recent advances in polymer protected gold nanoparticles: synthesis properties and applications. *Chem.Commun* , 4580-4598.
76. Ullmann, D. K. (1997). Nanofabrication of small copper clusters on Gold (111) electrodes by a scanning tunneling microscope. *Science , 275* (5303), 1097.
77. Vincent Stuart, J. C. (2011). Very small bubble ar surfaces- the nanobubble puzzle. *Soft Matter , 7*, 40-48.
78. W.Y., C. W. Synthesis of Gold Nanoparticles and Hollow Gold Nanostructures. National University of Singapore, Department of Chemistry.
79. Wang Y, Q. W. (2008b). A label-free biosensor based on gold nanoshell monolayers for monitoring biomolecular interactions in diluted whole blood. *Biosens Bioelectron , 23*, 1166-1170.
80. Westwater, J. P. (1964). Measurements of The Growth of Electrolytic Bubbles. *Int. J. Heat Mass Transfer , 7*, 1427-1443.
81. Xiamao Lu, J. C. (2007). Galvanic replacement reaction: a simple and powerful route to hollow and porous metal nanostructures. *Journal of Nanoengineering and Nanosystems , 221*.
82. Xiaohua Huang, I. H.-S.-S. (2006). Cancer Cell Imaging and Photothermal Therapy in the Near-Infrared Region by Using Gold Nanorods. *Journal of the American Chemical Society , 128* (6), 2115-2120.
83. Xiaoming Sun, Y. L. (2004). Ga2O3 and GaN Semiconductor Hollow Spheres. *Angewandte Chemie International Edition , 43* (29), 3827-3831.
84. Xie H, G.-s. K. (2007). Quantitative estimation of gold nanoshell concentrations in whole blood using dynamic light scattering . *Nanomedicine , 3*, 89-94.
85. Xiong Wen (David) Lou, L. A. (2008). Hollow Micro-/Nanostructures: Synthesis and Applications. *Adv. Mater. , 20* (21), 3987-4019.
86. Yadong Yin, R. M. (2004). Formation of Hollow Nanocrystals Through the Nanoscale Kirkendall Effect. *Science , 304* (5671), 711-714.
87. Yongsheng, J. Z. (2003). Hollow Spheres of Mesoporous Aluminosilicate with a Three-Dimensional Pore Network and Extraordinarily High Hydrothermal Stability. *Nano Letters , 3* (5), 609-612.
88. Yugang Sun, B. M. (2003). Metal Nanostructures with Hollow Interiors. *Advanced Materials , 15* (7-8), 641-646.

89. Yugang Sun, B. M. (2003). Metal Nanostrucutres with Hollow Interiors. *Advanced Materials , 15* (7-8), 641-646.

BIOGRAPHICAL INFORMATION

Chivarat Muangphat was born on July 20th, 1975 in Bangkok, Thailand. She completed her Bachelor of Science in Applied Physics from King Mongkut's Institute of Technology North Bangkok, Thailand in August 1995 and she received her Master of Engineering in Materials Technology from King Mongkut's University of Technology Thonburi in August 2001. She worked as a scientist in Division of Materials Technology, King Mongkut's University of Technology Thonburi.

She joined Ph.D. program in Materials Science and Engineering, University of Texas at Arlington in Fall 2007. Her current research interests include the fabrication and characterization of nanoparticles.